



Bruna Costa Leopércio

Gellan-based microcapsules: production and applications

Tese de Doutorado

Thesis presented to the Programa de Pós-graduação em Engenharia Mecânica of PUC-Rio in partial fulfillment of the requirements for the degree of Doutor em Engenharia Mecânica.

Advisor : Prof. Márcio da Silveira Carvalho

Co-advisor: Prof. Mariano Michelon

Rio de Janeiro
March 2021



Bruna Costa Leopércio

Gellan-based microcapsules: production and applications

Thesis presented to the Programa de Pós-graduação em Engenharia Mecânica of PUC-Rio in partial fulfillment of the requirements for the degree of Doutor em Engenharia Mecânica. Approved by the Examination Committee.

Prof. Márcio da Silveira Carvalho

Advisor

Departamento de Engenharia Mecânica - PUC-Rio

Prof. Mariano Michelin

Co-advisor

Escola de Química e Alimentos - FURG

Prof. John Frostad

UBC

Prof. Lucimara Gaziola de la Torre

Faculdade de Engenharia Química - UNICAMP

Prof. Patrick Tabeling

ESPCI Paris

Prof. Shima Parsa

RIT

Rio de Janeiro, March the 29th, 2021

All rights reserved.

Bruna Costa Leopércio

Bruna Leopércio graduated in Mechanical Engineering at Pontifical Catholic University of Rio de Janeiro (PUC-Rio) in 2014. Soon after, she started working as researcher in the Rheology Group (GReo) at PUC-Rio. In 2016, Bruna got her Master's degree in Thermosciences at the Mechanical Engineering Department studying the formation of cyclopentane hydrates through interfacial rheology. Since 2017, she has been working in the Laboratory of Microhydrodynamics and Flow in Porous Media (LMMP) at PUC-Rio. Bruna has been involved in research projects with Petrobras, Equinor and Shell. Her research interests include emulsification, microencapsulation, microfluidics, confocal microscopy and rheology and characterization of complex fluids.

Bibliographic data

Leopércio, Bruna

Gellan-based microcapsules: production and applications / Bruna Costa Leopércio; advisor: Márcio da Silveira Carvalho; co-advisor: Mariano Michelon. – Rio de Janeiro: PUC-Rio, Departamento de Engenharia Mecânica, 2021.

v., 123 f: il. color. ; 30 cm

Tese (doutorado) - Pontifícia Universidade Católica do Rio de Janeiro, Departamento de Engenharia Mecânica.

Inclui bibliografia

1. Engenharia Mecânica – Teses. 2. Engenharia Mecânica – Teses. 3. microfluídica;. 4. goma gelana;. 5. microcápsulas;. 6. biopolímero;. 7. escoamento confinado;. 8. gastro-resistência;. 9. cápsulas magnéticas.. I. Carvalho, Márcio. II. Michelon, Mariano. III. Pontifícia Universidade Católica do Rio de Janeiro. Departamento de Engenharia Mecânica. IV. Título.

CDD: 621

Acknowledgments

I would like to thank my advisor, Márcio, for taking me out of my comfort zone and for the inspiring technical discussions through these years. I learn a lot from you.

I also thank my co-advisor, Mariano, for sharing his technical knowledge and his time in the lab with me. It was fun and enriching to work side by side with you.

To CNPq, PUC-Rio, Shell and ANP, for financial support. This study was financed in part by the Coordenação de Aperfeiçoamento de Pessoal de Nível Superior - Brasil (CAPES) - Finance Code 001.

I thank my lab colleagues at LMMP, whose comments and suggestions, pizzas and cakes have made my doctorate easier and funnier. Especially, Sergio and Fred for their valuable collaboration in the last part of this work.

To my colleagues at GReo, who were by my side when I started this journey and are always willing to help me.

To my grandparents, for all the support and inspiration.

To Ian, for the partnership, encouragement and interest in everything I do.

To my brothers, for always being with me and for making any problem smaller.

To my father, for his unconditional encouragement, care and love.

To my mother, who will no longer be the only one with a PhD degree at the lunch table, for everything.

Abstract

Leopércio, Bruna; Carvalho, Márcio (Advisor); Michelon, Mariano (Co-Advisor). **Gellan-based microcapsules: production and applications**. Rio de Janeiro, 2021. 123p. Tese de doutorado – Departamento de Engenharia Mecânica, Pontifícia Universidade Católica do Rio de Janeiro.

Microcapsules are applied in several sectors of industry when a physical barrier between the core material and the external environment is required. They protect their cargo and ultimately release it in a controlled way. In the present work, microcapsules with hydrogel-based shells are produced. Monodispersed microcapsules are formed by ionotropic gelation of gellan gum from monodispersed oil-in-water-in-oil (O/W/O) double emulsion templates obtained using glass-capillary microfluidic devices. An oil extraction step was added after the shell gelation process to enable the dispersion of the microcapsules in an aqueous medium. We report the operability window for the production of monodispersed microcapsules as a function of the flow rate of each fluid phase and the dimensions of the device. Microcapsules with mean diameters ranging from 95 to 260 μm and a maximum coefficient of variation of 5% were formed. The results show how to independently control the capsule diameter and shell thickness by varying the outer and middle phase flow rates. After that, we experimentally investigate the flow of monodispersed gellan gum microcapsules through a constricted capillary tube by measuring the evolution of the pressure difference and flow visualization. The maximum pressure difference and capsule deformation is obtained for capsules with different diameter and shell thickness. We map the conditions at which the capsule membrane ruptures during the flow, releasing its internal phase. Then, the gastro-resistance of gellan microcapsules is verified through an *in vitro* test that mimics the gastric and intestinal phases of digestion. Confocal fluorescence microscopy is used to track microcapsules integrity and we show that microcapsules cargo is released in the intestine mostly due to its pH. Finally, we demonstrate that it is possible to produce magnetic microcapsules with well controlled magnetic response by adding different amounts of ferrofluid to their core or shell. The microcapsules produced have great potential for different applications in food, biomedical, pharmaceutical and oil and gas industries.

Keywords

microfluidics; gellan gum; microcapsules; biopolymer; confined flow; gastroresistance; magnetic capsules.

Resumo

Leopércio, Bruna; Carvalho, Márcio; Michelin, Mariano. **Microcápsulas de gelana: produção e aplicações**. Rio de Janeiro, 2021. 123p. Tese de Doutorado – Departamento de Engenharia Mecânica, Pontifícia Universidade Católica do Rio de Janeiro.

Microcápsulas são utilizadas em diversos setores da indústria para isolar o material interno do ambiente externo. Elas protegem o conteúdo interno e permitem uma liberação controlada. Neste trabalho, apresenta-se um método de produção de microcápsulas de goma gelana monodispersas a partir da formação de modelos de emulsão dupla óleo-em-água-em-óleo por microfluídica. A extração do óleo externo, após a gelificação ionotrópica, permite a dispersão das microcápsulas em meios aquosos. Assim, o método proposto permite encapsular ativos hidrofóbicos e dispersar as microcápsulas em uma fase aquosa, tendo diversas aplicações. Foram definidas janelas de operação para produção de microcápsulas de gelana monodispersas em função da vazão volumétrica de cada fluido que forma as microcápsulas e das dimensões do dispositivo microfluídico. Produziu-se microcápsulas com diâmetros variando de 95 a 260 μm e um coeficiente de variação máximo de 5%. Os resultados mostram que é possível controlar o diâmetro das cápsulas e a espessura da membrana através das vazões da fase externa e intermediária, respectivamente. Além disso, estudamos o escoamento de cápsulas de gelana com diferentes diâmetros e espessuras de membrana por um capilar com constrição através de imagens microscópicas e medidas de diferença de pressão. Mapeamos as condições nas quais a membrana é rompida devido à constrição e o conteúdo interno é liberado durante o escoamento. A gastroresistência das cápsulas de gelana é verificada através de testes *in vitro* que simulam as fases gástrica e intestinal da digestão. Mostramos, através de imagens fluorescentes, que as cápsulas são capazes de liberar o conteúdo interno apenas no intestino devido ao seu pH. Finalmente, demonstramos ser possível, não só produzir microcápsulas magnéticas, mas controlar a resposta magnética delas regulando a quantidade de ferrofluido que é adicionada à fase interna ou à membrana polimérica. As microcápsulas produzidas neste estudo têm grande potencial de aplicação em diversos setores, como alimentício, biomédico, farmacêutico e de óleo e gás.

Palavras-chave

microfluídica; goma gelana; microcápsulas; biopolímero; escoamento confinado; gastroresistência; cápsulas magnéticas.

Table of contents

| | | |
|-------|--|------------|
| 1 | Introduction | 16 |
| 1.1 | Objectives | 18 |
| 1.2 | Content of the chapters | 18 |
| 2 | Literature Review | 20 |
| 2.1 | Emulsions | 20 |
| 2.2 | Microcapsules | 21 |
| 2.3 | Microfluidics | 25 |
| 2.4 | Gellan gum | 27 |
| 3 | Microcapsules production by microfluidics | 32 |
| 3.1 | Gellan-based microcapsules | 32 |
| 3.2 | Experimental set-up and methodology | 34 |
| 3.2.1 | Microfluidic device | 34 |
| 3.2.2 | Experimental set-up | 37 |
| 3.2.3 | Microcapsules recovery | 39 |
| 3.2.4 | Microcapsules size and shell thickness | 39 |
| 3.3 | Operability window | 40 |
| 3.3.1 | Microfluidic design A ($\phi_i = 80 \mu\text{m}$, $\phi_c = 350 \mu\text{m}$ and $l = 120 \mu\text{m}$) | 41 |
| 3.3.2 | Microfluidic design B ($\phi_i = 50 \mu\text{m}$, $\phi_c = 250 \mu\text{m}$ and $l = 75 \mu\text{m}$) | 55 |
| 3.4 | Conclusions | 59 |
| 4 | Flow of microcapsules through constricted capillary | 60 |
| 4.1 | Introduction | 60 |
| 4.2 | Experimental set-up and methodology | 62 |
| 4.3 | Results and discussion | 65 |
| 4.4 | Conclusions | 76 |
| 5 | Gastroresistant microcapsules | 78 |
| 5.1 | Introduction | 78 |
| 5.2 | Experimental set-up and methodology | 79 |
| 5.3 | Results and discussion | 80 |
| 5.4 | Conclusions | 82 |
| 6 | Magnetic microcapsules | 83 |
| 6.1 | Introduction | 83 |
| 6.2 | Experimental set-up and methodology | 85 |
| 6.2.1 | Ferrofluids | 85 |
| 6.2.2 | Production of magnetic microcapsules | 85 |
| 6.2.3 | Magnetic response test | 88 |
| 6.2.4 | Results and discussion | 91 |
| 6.2.5 | Conclusions | 104 |
| 7 | Final remarks and suggestions for future works | 105 |

List of figures

| | | |
|------------|--|----|
| Figure 1.1 | Microcapsule formed by solidification of the middle phase of a double emulsion droplet. | 16 |
| Figure 1.2 | Two emulsification steps required to form a double emulsion. | 17 |
| Figure 1.3 | Microfluidic device for generating double emulsions in a single step: (a) injection capillary; (b) collection capillary and (c) square capillary. | 17 |
| Figure 2.1 | Water-in-oil and oil-in-water simple emulsions. Water is represented in blue and oil in brown. | 20 |
| Figure 2.2 | Oil-in-water-in-oil and water-in-oil-in-water double emulsions. Water is represented in blue and oil in brown. | 21 |
| Figure 2.3 | Simplified form of a microcapsule with core protected by a shell. Based on [1]. | 22 |
| Figure 2.4 | (a) Mono-core microcapsule and (b) poly-core microcapsule. | 22 |
| Figure 2.5 | Microfluidic device developed by Utada et al. for generating double emulsions. Reproduced from [2]. | 26 |
| Figure 2.6 | Chemical structure of the repeating unit of (a) acetylated or high acyl form of gellan gum and (b) deacetylated or low acyl gellan gum form, both reproduced from [3]. | 28 |
| Figure 2.7 | Gradual transformation of gellan gum from aqueous solutions. Based on [4]. | 29 |
| Figure 3.1 | Flow curves at 25 °C: (●) inner phase, (■) middle phase and (▲) continuous phase. | 33 |
| Figure 3.2 | Perspective view of the coaxial glass-capillary device with detail of the droplet generation region. Q_i , Q_m and Q_o are the flow rate of inner, middle and continuous phases, respectively. | 36 |
| Figure 3.3 | Coaxial glass-capillary device. | 36 |
| Figure 3.4 | Experimental set-up for microcapsules production, including: (a) an inverted microscope; (b) a high speed camera; (c) a computer; (d) three syringe pumps and (e) a collection vial. | 38 |
| Figure 3.5 | Scheme of the experimental set-up for microcapsules production. | 38 |
| Figure 3.6 | Microcapsule diameter of 142.4 μm being measured in Leica Application SuiteX software. | 40 |
| Figure 3.7 | O/W/O template formation in the ideal intermittent dripping regime. | 41 |

- Figure 3.8 (a) Operability window as a function of the flow rates Q_m and Q_o at a fixed inner phase flow rate, $Q_i = 200 \mu\text{L/h}$ using Design A ($\phi_i = 80 \mu\text{m}$, $\phi_c = 350 \mu\text{m}$ and $l = 120 \mu\text{m}$) and (b) Operability window represented as a function of the outer and middle phases capillary numbers: (\square) monodispersed O/W/O templates, (\blacktriangle) jetting regime, formation of double emulsion with multiple inner compartments, (\bullet) formation of droplets containing only the middle phase without the inner core together with the formation of polydispersed microcapsules, (\blacksquare) back flow regime, the outer phase invades the injection channels of the inner and middle phases. 42
- Figure 3.9 Jetting flow regime: (a) Polydisperse microcapsules formed far from the entrance of the collection capillary and (b) Microcapsules formed with multiple inner phase drops inside a single middle phase drop. 43
- Figure 3.10 (a) Microcapsule diameter (D) as a function of middle and outer phase flow rates (Q_m and Q_o) at a fixed $Q_i = 200 \mu\text{L/h}$ with Design A ($\phi_i = 80 \mu\text{m}$, $\phi_c = 350 \mu\text{m}$ and $l = 120 \mu\text{m}$) and (b) power-law fit of the diameter in units of the collecting capillary diameter (continuous line) as a function of $Q_o/(Q_i + Q_m)$: $Q_m =$ (\blacksquare) $25 \mu\text{L/h}$, (\bullet) $50 \mu\text{L/h}$, (\blacktriangle) $100 \mu\text{L/h}$, (\blacktriangledown) $150 \mu\text{L/h}$, (\blacktriangleright) $200 \mu\text{L/h}$, (\blacktriangleleft) $250 \mu\text{L/h}$ and (\blacklozenge) $300 \mu\text{L/h}$. 46
- Figure 3.11 Examples of micrographs and particle size distributions of the microcapsules produced at different Q_o : (a) $Q_i = 200 \mu\text{L/h}$, $Q_m = 200 \mu\text{L/h}$ and $Q_o = 1000 \mu\text{L/h}$ and (b) $Q_i = 200 \mu\text{L/h}$, $Q_m = 200 \mu\text{L/h}$ and $Q_o = 4500 \mu\text{L/h}$. 47
- Figure 3.12 (a) Shell thickness in units of droplet radius ($t/(D/2)$) as a function of middle and outer phase flow rates (Q_m and Q_o) at a fixed $Q_i = 200 \mu\text{L/h}$ with Design A ($\phi_i = 80 \mu\text{m}$, $\phi_c = 350 \mu\text{m}$ and $l = 120 \mu\text{m}$): $Q_m =$ (\blacksquare) $25 \mu\text{L/h}$, (\bullet) $50 \mu\text{L/h}$, (\blacktriangle) $100 \mu\text{L/h}$, (\blacktriangledown) $150 \mu\text{L/h}$, (\blacktriangleright) $200 \mu\text{L/h}$, (\blacktriangleleft) $250 \mu\text{L/h}$ and (\blacklozenge) $300 \mu\text{L/h}$ and (b) Shell thickness evaluated by Equation 3-8 (continuous line) as a function of the flow rate ratio Q_m/Q_i : $Q_o =$ (\blacksquare) $500 \mu\text{L/h}$, (\bullet) $1000 \mu\text{L/h}$, (\blacktriangle) $1500 \mu\text{L/h}$, (\blacktriangledown) $2000 \mu\text{L/h}$, (\blacktriangleright) $2500 \mu\text{L/h}$, (\blacktriangleleft) $3000 \mu\text{L/h}$, (\blacklozenge) $3500 \mu\text{L/h}$, (\blacksquare) $4000 \mu\text{L/h}$, (\bullet) $4500 \mu\text{L/h}$ and (\blacktriangle) $5000 \mu\text{L/h}$. 49
- Figure 3.13 Examples of microcapsules with different shell thickness (paired red arrows) produced at different Q_m : (a) $Q_i = 200 \mu\text{L/h}$, $Q_m = 250 \mu\text{L/h}$ and $Q_o = 1500 \mu\text{L/h}$ and (b) $Q_i = 200 \mu\text{L/h}$, $Q_m = 50 \mu\text{L/h}$ and $Q_o = 1500 \mu\text{L/h}$. 50
- Figure 3.14 (a) Operability window as a function of the flow rates Q_i and Q_o at a fixed middle phase flow rate, $Q_m = 100 \mu\text{L/h}$ using Design A ($\phi_i = 80 \mu\text{m}$, $\phi_c = 350 \mu\text{m}$ and $l = 120 \mu\text{m}$) and (b) Operability window represented as a function of the outer and inner phases capillary numbers: (\square) monodispersed O/W/O templates, (\blacktriangledown) jetting regime, formation of polydispersed microcapsules, (\blacksquare) back flow regime, the outer phase invades the injection channels of the inner and middle phases. 51

Figure 3.15 (a) Microcapsule diameter (D) as a function of inner and outer phase flow rates (Q_i and Q_o) at a fixed $Q_m = 100 \mu\text{L/h}$ with Design A ($\phi_i = 80 \mu\text{m}$, $\phi_c = 350 \mu\text{m}$ and $l = 120 \mu\text{m}$) and (b) power-law fit of the diameter in units of the collecting capillary diameter (continuous line) as a function of $Q_o/(Q_i + Q_m)$: $Q_i =$ (■) 25 $\mu\text{L/h}$, (●) 50 $\mu\text{L/h}$, (▲) 100 $\mu\text{L/h}$, (▼) 200 $\mu\text{L/h}$, (►) 300 $\mu\text{L/h}$. 53

Figure 3.16 (a) Shell thickness in units of droplet radius ($t(D/2)$) as a function of inner and outer phase flow rates (Q_i and Q_o) at a fixed $Q_m = 100 \mu\text{L/h}$ with Design A ($\phi_i = 80 \mu\text{m}$, $\phi_c = 350 \mu\text{m}$ and $l = 120 \mu\text{m}$): $Q_m =$ (■) 25 $\mu\text{L/h}$, (●) 50 $\mu\text{L/h}$, (▲) 100 $\mu\text{L/h}$, (▼) 200 $\mu\text{L/h}$, (►) 300 $\mu\text{L/h}$ and (b) Shell thickness evaluated by Equation 3-8 (continuous line) as a function of the flow rate ratio Q_m/Q_i : $Q_o =$ (■) 500 $\mu\text{L/h}$, (●) 1000 $\mu\text{L/h}$, (▲) 1500 $\mu\text{L/h}$, (●) 2000 $\mu\text{L/h}$, (►) 2500 $\mu\text{L/h}$, (◄) 3000 $\mu\text{L/h}$, (◆) 3500 $\mu\text{L/h}$, (■) 4000 $\mu\text{L/h}$. 54

Figure 3.17 (a) Operability window as a function of the flow rates Q_m and Q_o at a fixed inner phase flow rate, $Q_i = 100 \mu\text{L/h}$ using Design B ($\phi_i = 50 \mu\text{m}$, $\phi_c = 250 \mu\text{m}$ and $l = 75 \mu\text{m}$) and (b) Operability window represented as a function of the outer and middle phases capillary numbers: (□) monodispersed O/W/O templates, (▲) jetting regime, formation of double emulsion with multiple inner compartments, (●) formation of droplets containing only the middle phase without the inner core together with the formation of polydispersed microcapsules, (■) back flow regime, the outer phase invades the injection channels of the inner and middle phases. 56

Figure 3.18 (a) Microcapsule diameter (D) as a function of middle and outer phase flow rates (Q_m and Q_o) at a fixed $Q_i = 100 \mu\text{L/h}$ with Design B ($\phi_i = 50 \mu\text{m}$, $\phi_c = 250 \mu\text{m}$ and $l = 75 \mu\text{m}$) and (b) power-law fit of the diameter in units of the collecting capillary diameter (continuous line) as a function of $Q_o/(Q_i + Q_m)$: $Q_m =$ (●) 12.5 $\mu\text{L/h}$, (■) 25 $\mu\text{L/h}$, (◆) 50 $\mu\text{L/h}$, (►) 75 $\mu\text{L/h}$, (◄) 100 $\mu\text{L/h}$, (▼) 125 $\mu\text{L/h}$, (▲) 150 $\mu\text{L/h}$, (●) 200 $\mu\text{L/h}$ and (■) 250 $\mu\text{L/h}$. 57

Figure 3.19 (a) Shell thickness in units of droplet radius ($t(D/2)$) as a function of middle and outer phase flow rates (Q_m and Q_o) at a fixed $Q_i = 200 \mu\text{L/h}$ with Design A ($\phi_i = 50 \mu\text{m}$, $\phi_c = 250 \mu\text{m}$ and $l = 75 \mu\text{m}$): $Q_m =$ (●) 12.5 $\mu\text{L/h}$, (■) 25 $\mu\text{L/h}$, (◆) 50 $\mu\text{L/h}$, (►) 75 $\mu\text{L/h}$, (◄) 100 $\mu\text{L/h}$, (▼) 125 $\mu\text{L/h}$, (▲) 150 $\mu\text{L/h}$, (●) 200 $\mu\text{L/h}$ and (■) 250 $\mu\text{L/h}$ and (b) Shell thickness evaluated by Equation 3-8 (continuous line) as a function of the flow rate ratio Q_m/Q_i : $Q_o =$ (■) 500 $\mu\text{L/h}$, (●) 1000 $\mu\text{L/h}$, (▲) 1500 $\mu\text{L/h}$, (▼) 2000 $\mu\text{L/h}$, (►) 2500 $\mu\text{L/h}$, (◄) 3000 $\mu\text{L/h}$, (◆) 3500 $\mu\text{L/h}$, (■) 4000 $\mu\text{L/h}$. 58

Figure 4.1 Experimental set-up for flowing microcapsules through constriction capillaries, including: (a) a stand-alone pressure pump; (b) a Link module for PC communication; (c) a flow rate control unit; (d) a computer for pressure data recording; (e) a 15mL Falcon with an air-tight connector P-CAP; (f) an inverted microscope; (g) a high speed camera; (h) a computer for real time visualization and (i) a dispensing beaker. 63

- Figure 4.2 Scheme of the experimental set-up for flowing microcapsules through constriction capillaries. 63
- Figure 4.3 Evolution of the microcapsule position and configuration as it flows through the constriction. System #3, $D = 144.4 \mu\text{m}$ and $t = 15.2 \mu\text{m}$ ($\bar{a} = 1.44$ and $Ca_s = 5.9 \times 10^{-4}$). 66
- Figure 4.4 Evolution of the inlet pressure as the capsule flows through the constriction. System #3, $D = 144.4 \mu\text{m}$ and $t = 15.2 \mu\text{m}$ ($\bar{a} = 1.44$ and $Ca_s = 5.9 \times 10^{-4}$). 66
- Figure 4.5 Evolution of the microcapsule position and configuration as it flows through the constriction. System #5, $D = 109.1 \mu\text{m}$ and $t = 5.3 \mu\text{m}$ ($\bar{a} = 1.09$ and $Ca_s = 1.7 \times 10^{-3}$). 67
- Figure 4.6 Microcapsule position in the flow direction as it flows through the constriction for capsules from (●) System #3 ($\bar{a} = 1.44$ and $Ca_s = 5.9 \times 10^{-4}$) and (●) System #5 ($\bar{a} = 1.09$ and $Ca_s = 1.7 \times 10^{-3}$). 68
- Figure 4.7 Length of the microcapsule in the flow direction as it flows through the constriction for capsules from (●) System #3 ($\bar{a} = 1.44$ and $Ca_s = 5.9 \times 10^{-4}$) and (●) System #5 ($\bar{a} = 1.09$ and $Ca_s = 1.7 \times 10^{-3}$). 69
- Figure 4.8 Microcapsule deformation $\epsilon_x = L_x/L_{x,0}$ as it flows through the constriction for capsules from (●) System #3 ($\bar{a} = 1.44$ and $Ca_s = 5.9 \times 10^{-4}$) and (●) System #5 ($\bar{a} = 1.09$ and $Ca_s = 1.7 \times 10^{-3}$). 70
- Figure 4.9 Evolution of the microcapsule position and configuration as it flows through the constriction. System #1, $D = 174.6 \mu\text{m}$ and $t = 15.0 \mu\text{m}$ ($\bar{a} = 1.75$ and $Ca_s = 6.0 \times 10^{-4}$). 71
- Figure 4.10 Evolution of the inlet pressure as the capsule flows through the constriction. System #1, $D = 174.6 \mu\text{m}$ and $t = 15.0 \mu\text{m}$ ($\bar{a} = 1.75$ and $Ca_s = 6.0 \times 10^{-4}$). 72
- Figure 4.11 Evolution of the microcapsule position and configuration as it flows through the constriction. System #2, $D = 143.8 \mu\text{m}$ and $t = 6.3 \mu\text{m}$. 73
- Figure 4.12 Evolution of the microcapsule position and configuration as it flows through the constriction. System #4, $D = 124.4 \mu\text{m}$ and $t = 5.6 \mu\text{m}$. 74
- Figure 4.13 Map of state of capsule after flowing through the constriction as a function of dimensionless capsule diameter \bar{a} and surface capillary number Ca_s : (●) reversible deformation and (●) rupture. 76
- Figure 5.1 Confocal image of the inner phase of gellan microcapsules before static in vitro digestion simulation. 81
- Figure 5.2 Fluorescent image of the inner phase of gellan microcapsules after (a) 1 hour and (b) 2 hours in gastric conditions. 81
- Figure 5.3 Fluorescent image of the inner phase of gellan microcapsules after (a) 1 hour and (b) 2 hours in intestinal conditions. 82
- Figure 6.1 Device for PDMS microcapsules production: (a) photo of the coaxial glass-capillary device and (b) detail of the injection and collection capillaries. 87

- Figure 6.2 Schematic of a magnetic capsule flowing between magnets. Black arrows represent magnetic field lines. 89
- Figure 6.3 3D printed device with magnets and hose used to flow microcapsules between magnets. 90
- Figure 6.4 Experimental set-up for flowing microcapsules between magnets: (a) a syringe pump; (b) the 3D printed device; (c) a plastic tube; (d) an stereomicroscope; (e) a high speed camera; (f) a computer for real time visualization and (g) a dispensing beaker. 90
- Figure 6.5 Scheme of the experimental set-up for flowing microcapsules between magnets. 91
- Figure 6.6 Production of monodispersed (a) gellan magnetic microcapsules with ferrofluid as inner phase and (b) PDMS magnetic microcapsules with ferrofluid in the shell. 92
- Figure 6.7 Dependence of drag coefficient on Reynolds number and sphere-to-tube diameter ratio for a Newtonian fluid. Reproduced from [5]. 94
- Figure 6.8 System Gellan-core-75 microcapsule centroid position (x_c) as it flows between the magnets for different flow rates: $Q =$ (●) 170 mL/h, (●) 180 mL/h, (●) 190 mL/h, (●) 200 mL/h, (●) 210 mL/h, (●) 220 mL/h, (●) 230 mL/h and (●) 240 mL/h. $x_c = 0$ corresponds to magnets center plane. 95
- Figure 6.9 System Gellan-core-100 microcapsule centroid position (x_c) as it flows between the magnets for different flow rates: $Q =$ (●) 200 mL/h, (●) 250 mL/h, (●) 260 mL/h, (●) 270 mL/h, (●) 280 mL/h, (●) 290 mL/h, (●) 300 mL/h and (●) 310 mL/h. $x_c = 0$ corresponds to magnets center plane. 96
- Figure 6.10 System PDMS-core-25 microcapsule centroid position (x_c) as it flows between the magnets for different flow rates: $Q =$ (●) 10 mL/h (●) 20 mL/h (●) 30 mL/h, (●) 40 mL/h, (●) 50 mL/h, (●) 60 mL/h, (●) 70 mL/h, (●) 80 mL/h, (●) 90 mL/h and (●) 100 mL/h. $x_c = 0$ corresponds to magnets center plane. 97
- Figure 6.11 System PDMS-core-75 microcapsule centroid position (x_c) as it flows between the magnets for different flow rates: $Q =$ (●) 10 mL/h (●) 20 mL/h (●) 30 mL/h, (●) 40 mL/h, (●) 50 mL/h, (●) 60 mL/h, (●) 70 mL/h, (●) 80 mL/h, (●) 90 mL/h and (●) 100 mL/h. $x_c = 0$ corresponds to magnets center plane. 98
- Figure 6.12 System PDMS-core-100 microcapsule centroid position (x_c) as it flows between the magnets for different flow rates: $Q =$ (●) 60 mL/h, (●) 70 mL/h, (●) 80 mL/h, (●) 90 mL/h, (●) 100 mL/h, (●) 110 mL/h and (●) 120 mL/h. $x_c = 0$ corresponds to magnets center plane. 99
- Figure 6.13 Microcapsule final centroid position ($x_{c,final}$) as a function of the flow rate: (■) System PDMS-core-25, (▲) System PDMS-core-75, (●) System PDMS-core-100. 100
- Figure 6.14 Qualitative representation of the magnetic field variation with distance in the flow direction. 100

Figure 6.15 Microcapsule centroid position (x_c) as it flows between the magnets for different flow rates: $Q =$ (●) 5 mL/h, (●) 10 mL/h, (●) 15 mL/h, (●) 20 mL/h, (●) 30 mL/h and (●) 40 mL/h. $x_c = 0$ corresponds to magnets center plane. (a) System PDMS-shell-25-1, (b) System PDMS-shell-25-2 and (c) System PDMS-shell-25-3. 102

Figure 6.16 Maximum magnetic force as a function of the volume of suspended magnetic nanoparticles for capsules with particles suspended in the liquid core and in the solid shell: (■) Gellan-core, (▲) PDMS-core, (●) PDMS-shell. 104

List of tables

| | | |
|-----------|--|-----|
| Table 3.1 | Density (ρ), viscosity (μ) and interfacial tension (σ) of the phases at 25 °C. Different lowercase letters (a-b) represent significant differences ($p < 0.05$) between the phases. | 34 |
| Table 3.2 | Geometric parameters of the designs used. ϕ_i and ϕ_c are the inner diameter of the injection and collection capillaries, respectively, and l denotes the separation distance between them. Only designs A and B were successfully used to form monodispersed O/W/O templates. | 37 |
| Table 4.1 | Main properties of the microcapsules used in the constriction experiments. | 64 |
| Table 4.2 | Maximum extra pressure-drop and deformation and state of the capsule after passing through the constriction for each system tested. | 75 |
| Table 5.1 | Recommended concentrations of electrolytes in Simulated Gastric Fluid (SGF) and Simulated Intestinal Fluid (SIF), based on human <i>in vivo</i> data. Reproduced from [6]. | 80 |
| Table 6.1 | Main properties of the water-based ferrofluid EMG 601P from Ferrotec Corporation. | 85 |
| Table 6.2 | Main properties of the oil-based ferrofluid EFH1 from Ferrotec Corporation. | 85 |
| Table 6.3 | Magnetic field measured at 3 distances from the magnet. Data available in the magnets technical file from ImaShop. | 88 |
| Table 6.4 | Main properties of microcapsules with magnetic cores used in the magnet experiments. | 93 |
| Table 6.5 | Main properties of PDMS microcapsules with magnetic shells used in the magnet experiments. Shell thicknesses were calculated by Eq. 6-1. | 93 |
| Table 6.6 | Flow rates applied to form magnetic microcapsules. | 93 |
| Table 6.7 | Maximum magnetic force to stop the flow of capsules from each system. | 103 |

1 Introduction

Microcapsules are highly hierarchized structures with submillimeter dimensions containing an inner phase and a shell. They are promising candidates for embracing, delivering, and controllably releasing active ingredients. As such, their use has been seen in different areas for encapsulation of agricultural substances, cosmetic components, building materials, food additives, pharmaceuticals and surfactants for enhanced oil recovery [7, 8, 9, 10, 11]. Most applications require a shell that effectively retains and protects the inner phase and releases it only after exposure to a specific external condition, such as temperature, pH, osmotic pressure and external stress [10, 12, 13, 14, 15, 16]. Employing microcapsules in areas at which interaction with living organisms and natural degradation are involved requires the use of biocompatible and biodegradable polymers as the shell material. Alginates fulfill this necessity, being the most used biopolymer applied as shell component nowadays [9, 17, 18, 19, 20].

In general, microcapsules are obtained after a solidification step of the middle phase of a double emulsion template (Fig. 1.1). The preparation of double emulsion templates by conventional methods is not trivial and, commonly, two emulsification steps are required, as illustrated in Fig. 1.2. First, a simple emulsion is formed from high shear mixing of two immiscible phases, one aqueous and one oily. In a second step, a double emulsion is formed using milder shear conditions to avoid the disruption of the inner phase. The highly variable shear inherent to these conventional emulsification routes results in microcapsules with a broad distribution of sizes, making it difficult to control the shell thickness, and consequently, generating poorly controlled encapsulation and release characteristics [7, 21].

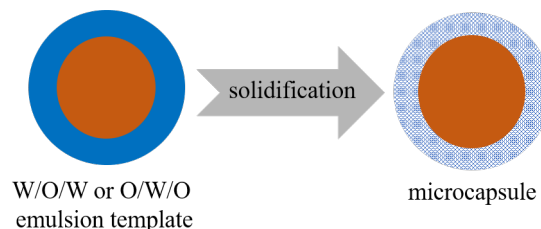


Figure 1.1: Microcapsule formed by solidification of the middle phase of a double emulsion droplet.

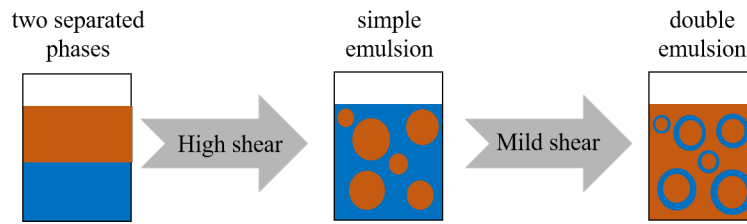


Figure 1.2: Two emulsification steps required to form a double emulsion.

Microfluidic technology [22] is a promising technique for the fabrication of monodispersed double emulsion templates that overcome these drawbacks, providing well-controlled release characteristics to the final product. The fluids that form the microcapsules flow inside micro-capillaries and double emulsion templates are formed in a single step as the inner and middle phase jets break in the entrance of the collection capillary, as exemplified in Fig. 1.3. The breakup of these jets depends on the balance between the pinning, drag and capillary forces acting in the tip of the injection capillary. Different devices have been developed over the past few years.

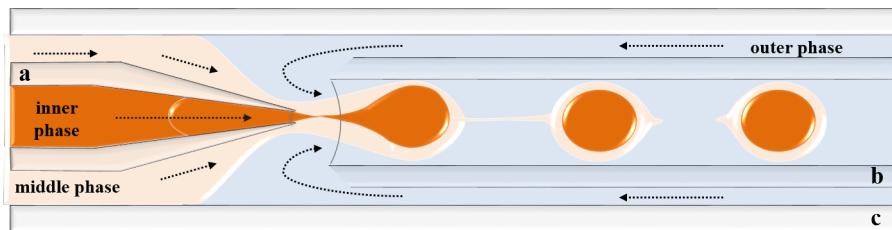


Figure 1.3: Microfluidic device for generating double emulsions in a single step: (a) injection capillary; (b) collection capillary and (c) square capillary.

Microfluidics enables a fine control of the template dimensions and offers high flexibility with regard to the materials that can be used to form the microcapsule shell [23, 24]. Using the microfluidic approach, a variety of hydrophilic or hydrophobic active compounds can be truly encapsulated as the inner phase of water-in-oil-in-water (W/O/W) or oil-in-water-in-oil (O/W/O) double emulsion templates, respectively.

Therefore, there is a worldwide interest in microcapsules, which are very versatile products already used in a broad range of applications and possibly appropriate for exploration of new ones, specially if biodegradable materials are used. Additionally, the improvement of their production methods is also of great relevance. These facts motivated the present research. We report the development of a procedure to produce biocompatible microcapsules with different sizes and shell thicknesses from O/W/O double emulsion templates using a glass-capillary microfluidic device [2]. The shell is made of gellan gum, which is a biopolymer poorly exploited as shell

component material although it can form stronger and less permeable hydrogels than the ones formed with alginates. A prominent collection method enables the microcapsules, which are originally dispersed in oil, to be suspended in an aqueous phase. Then the response of gellan gum microcapsules to external stress, digestion conditions and external magnetic field is studied. Gellan gum microcapsules are suitable for containing hydrophobic compounds and our experiments indicate that they can be used in assorted applications.

1.1

Objectives

The main objective of this thesis is to study the conditions required to form monodispersed microcapsules with a shell made of gellan gum through microfluidics. Then, we study different applications for the microcapsules by testing their characteristics regarding response to external stress, digestibility conditions and magnetic signal.

1.2

Content of the chapters

This document is divided into six more chapters besides this first one. In Chapter 2, the concepts of emulsions and microcapsules are presented and the state of the art is revisited. It gives an overview of microcapsules technological applications. Besides that, it mentions the main techniques for producing microcapsules, focusing on microfluidics, which is the one explored in this work. Chapter 2 also discusses some important characteristics of gellan gum that justify its commercial value and use in this research.

In Chapter 3, a detailed description on the procedure developed to produce gellan gum monodispersed microcapsules is given. It includes the materials used, the microfluidic set-up and how microcapsules diameter and shell thickness are measured. Also, the groundbreaking recovery process is described. Then, the operability window of the microfluidic devices required to achieve the dripping flow regime that leads to a monodispersion is determined. Moreover, it is shown how the microcapsule diameter and shell thickness can be controlled by changing the flow parameters.

Chapter 4 presents an experimental study of the flow of suspended capsules through a constricted capillary by measuring the evolution of the pressure difference and flow visualization. The maximum pressure difference and capsule deformation is obtained for capsules with different diameter and shell thickness. We map the conditions at which the capsule membrane ruptures during the flow, releasing its internal phase.

Chapter 5 analyses the use of gellan-based microcapsules as a gastro-resistant carrier for controlled release in the intestine. A potential application is to encapsulate bacteria for probiotic products.

Gellan gum microcapsules are magnetized by the addition of biocompatible ferrofluids to their inner phase or shell. This enlarges the possibilities of using these microcapsules in applications that require non-intrusively manipulation by external magnetic fields or detection by magnetic sensors. The response of magnetized microcapsules to external magnetic field is studied in Chapter 6.

Finally, Chapter 7 brings the main conclusions of the present research as well as some suggestions for future works.

2 Literature Review

2.1 Emulsions

Emulsions are dispersions in which a liquid is suspended as small spherical droplets in a continuous liquid phase of different composition. In general, one of the liquids is aqueous and the other is oily. If water droplets are dispersed in oil, the emulsion is called water-in-oil (W/O) and if oil droplets are dispersed in water, the emulsion is called oil-in-water (O/W). Figure 2.1 illustrates both systems.

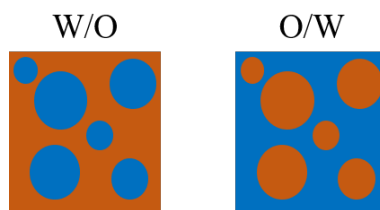


Figure 2.1: Water-in-oil and oil-in-water simple emulsions. Water is represented in blue and oil in brown.

To be considered stable, an emulsion has to resist to physical changes over a practical length of time [25]. Most emulsions are not thermodynamically stable because liquid-liquid systems have a tendency to decrease their free energy with time by reducing the total interfacial area [26]. Therefore, an emulsifier or stabilizer, which is usually a surfactant, a macromolecule or finely divided solids [27], is needed to promote steric or electrostatic stabilization. These agents adsorb to the oil-water interface promoting droplet stability by lowering the interfacial tension and, consequently, the droplet size or by forming a mechanical barrier that hinders coalescence, flocculation and other mechanisms of destabilization [25, 28, 29, 30, 31].

According to Bancroft's rule, the nature of the emulsifier added to the mixture dictates the type of emulsion that will be formed. It states that the phase in which an emulsifier is more soluble constitutes the continuous phase of the emulsion [32, 33, 34]. Counterintuitively, it means that the choice of the emulsifier is even more relevant than the relative percentages of each phase. Therefore, in general, if a hydrophilic surfactant is used to stabilize a system, it tends to form an oil-in-water

emulsion while, if a hydrophobic surfactant is used, it tends to form a water-in-oil emulsion.

The size of the droplets of an emulsion can also be controlled by the emulsifier type as well as by the emulsifier concentration and homogenization conditions (such as applied energy and duration) [35, 36].

A system that contains three immiscible phases instead of two is called a double emulsion (Fig. 2.2). It is formed of small droplets of a liquid contained within larger droplets of a second liquid that are dispersed within a continuous phase (third liquid). There are two types of double emulsions: oil-in-water-in-oil ($O_1/W/O_2$) emulsions, in which the inner and outer phases are oil-based, and water-in-oil-in-water ($W_1/O/W_2$) emulsions, in which the inner and outer phases are water-based. Usually two emulsifiers are required to stabilize a double emulsion - a water soluble and an oil soluble [35, 36].

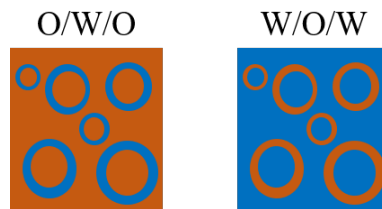


Figure 2.2: Oil-in-water-in-oil and water-in-oil-in-water double emulsions. Water is represented in blue and oil in brown.

2.2

Microcapsules

As shown in Fig. 2.3, microcapsules are formed by a core material, which is called internal phase, payload or fill, and a wall called shell, membrane or coating [1, 37]. They range in size from one micron (one thousandth of a millimeter) to few millimeters and can have a relative high surface area (inversely proportional to the diameter) [11].

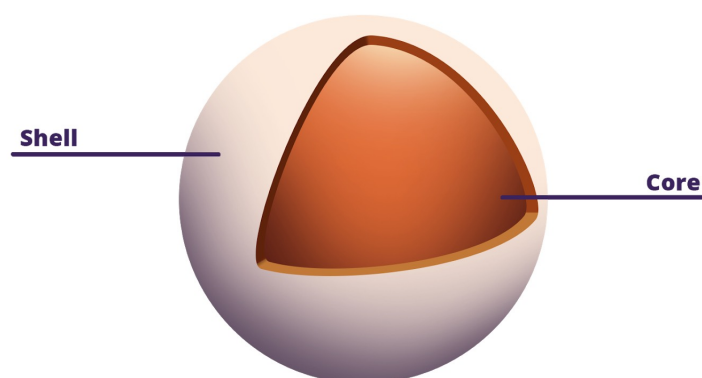


Figure 2.3: Simplified form of a microcapsule with core protected by a shell. Based on [1].

Microcapsules are used when it is necessary to have a physical barrier between the core material, which can be a solid, liquid, or gaseous substance, and the external environment. They can be classified into two basic categories: (i) as mono-core, or single-core, and (ii) as poly-core, or multiple-core. The first group possesses a single core enveloped by the shell, while the second possesses more than one chamber within the shell [1, 11, 37, 38, 39], as illustrated in Fig. 2.4. Some authors, especially in the food area, also consider a microparticle that has active compounds integrated within the shell matrix as a microcapsule just because it carries and protects the active compound, exhibiting controlled release or targeted delivery properties [11, 38, 39, 40].

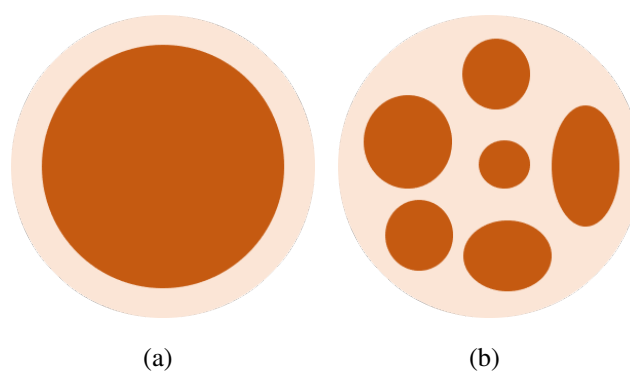


Figure 2.4: (a) Mono-core microcapsule and (b) poly-core microcapsule.

Some microcapsules may present double or multiple concentric coating. The diameter and shape of microcapsules are usually defined by the wall material and the methods used to prepare them [1, 41]. These elements also determine the degree of protection for the core, as well as the stability of the capsule [1, 42]. Usual shell

materials are sugars, gums, proteins, natural and modified polysaccharides, lipids and synthetic polymers [37].

The process of forming microcapsules is called microencapsulation. Emulsification technology is a key step in the microencapsulation once microcapsules are often made from single or double emulsion drops that are subsequently converted into capsules [8].

Microencapsulation is used for several reasons. It can disguise undesirable characteristics of a material such as flavor, smell and pH; improve the processing capacity of an ingredient and facilitate the handling of some materials by turning liquids into solid; enable the controlled release of a material at the right place and the right time; guarantee safe and convenient handling of materials which are otherwise toxic or noxious; and separate incompatible or reactive compounds [40, 43, 44].

The first record of applying microencapsulation in a product is from 1953 when Green and Scheiner [45] used microscopic pressure-rupturable capsules with oily nuclei to manufacture carbonless copying paper. Since then, microencapsulation has enabled the development of new products and the improvement of existing ones for a wide variety of industries such as pharmaceutical, textile, cosmetic, food, electronic and biomedical.

Specifically in the pharmaceutical industry, microcapsules are applied to reduce adverse reactions and side effects, allow site-specific and sustained drug delivery, increase shelf-life, act as an alternative administration mode, overcoming, for instance, the need of medical supervision, and even to prepare intrauterine contraceptive devices [41, 46, 47, 48].

In biomedicine, microcapsules containing bioadsorbents and enzymes, for example, are commonly used [49]. More challenging, microencapsulation of mammalian cells for use in musculoskeletal, neural, skin, hepatic and cardiovascular tissue engineering [50, 51] and in tumor therapy [52, 53] has also been evaluated. It is even possible to incorporate ferrofluids to microcapsules which then present magnetic properties [54, 55]. Such capsules can be used in diagnostics and therapeutics that require tracking and guiding chemical-filled capsules to specific areas of the human body through application of a magnetic field [56, 57].

The demand for "functional foods", which can have ingredients that are environmental and/or processing unstable, has made the interest of food industry on microencapsulation grow. This technology allows the incorporation of flavouring agents, sweeteners, colorants and vitamins as well as of living cells, such as probiotics, to different foods and beverages [11, 41, 58, 59]. In addition, microcapsules can protect active compounds from processing and packaging conditions and from the severe gastrointestinal environment and increase their shelf life [11].

The cosmetic industry uses microcapsules filled with essential oils that play a

major role as fragrance ingredients, to conserve them by avoiding evaporation, heating, oxidation, volatilization or undesired chemical interactions [60, 61]. Besides that, microcapsules containing vitamins, essential oils, skin moisturising agents, skin cooling agents, anti-aging agents, insects repellents are also used in smart textiles, which are designed to transfer the active substance when in contact with human body and skin [62]. They resist several washing cycles protecting and controlling the delivery of the active ingredient.

In defense applications, microcapsules are used in self-healing polymers and composites to store the healing agent and provide a mechanical trigger for the self-healing process when ruptured as the damage occurs. Due to their enhanced chemical protection against chemical warfare, microcapsules are also used in special fabrics for military personnel [11].

The agriculture sector has also noticed the value of microcapsules: they can function as vehicle and protection from oxidation and light during storage and release for pheromones that will disrupt insects mating process, acting as an alternative to conventional hazardous pesticides [11].

Other technological application is the use of microcapsules as a selfhealing method for asphalt pavements, once they have the potential of encapsulating and delivering the rejuvenator at damage site within the asphalt mastic mix [9, 63]. Although this healing method can not recover as much strength as current induction heating method, it aims at the rejuvenation of aged binder.

The use of microcapsules for enhanced oil recovery has been exploited as surfactant delivery vehicles to oil-water interfaces [10] and as fluid mobility agents that lead to flow redistribution in the porous space [64, 65], resulting in increased volumes of recovered oil.

As demonstrated, the relevance of microcapsules, which can be made of varied materials and through several procedures, in different areas is clear. In certain applications, microcapsules which do not lose their contents during their useful life are required, when, for example, they are suspended in a fluid stream for measurement purposes. However, in almost all applications, besides the necessity to protect the inner content, there is also the need to ultimately release it. Therefore, it is crucial to formulate stable capsules specifically for each purpose and to know their degradation kinetics and the mechanisms that guarantee release of the core material. In general, the release will be a consequence of mechanical rupture, biodegradation, dissolution or melting of the shell or diffusion through it [11, 43]. Frequently, combinations of these release mechanisms are desirable.

The final properties of microcapsules affect the active compound release rate. In this regard, different triggers can be applied to activate the core release depending on the material that forms the microcapsule and how it was formulated. Temperature

[12, 13], pH [14], osmotic pressure [15, 16], external stress [10] and chemical reaction [10, 66] are some of the most used ones.

2.3

Microfluidics

There are many physical, chemical and physicochemical methods to produce emulsions that will later become capsules [67]. Some of them are spray drying [68, 69, 70], fluidized bed coating [71, 72], extrusion [73, 74], coacervation [75, 76] and membrane emulsification [77, 78]. However, these conventional techniques usually yield polydisperse microcapsules with variable composition associated to a poorly controlled encapsulation and release kinetics [7, 21]. This fact limits the applicability of microcapsules in different areas.

Microfluidic technology offers a route to overcome these drawbacks, emerging as a promising alternative technique for the fabrication of monodispersed double emulsion templates that are subsequently converted into microcapsules with well-controlled release properties. The formation of double emulsion templates in capillary microfluidic devices enables tuning the template dimensions and using a broad range of materials to form the microcapsule shell [8, 23, 24].

As pointed by Amstad [8], the degree of control over the drop size is low if the drops are formed through mechanical agitation using rotor-stator systems or high-pressure homogenization; it is much higher if drops are formed using membranes and even higher if they are formed with microfluidics.

Microfluidic generation of drops differs from the generation of drops in unconfined geometries and is dominated by confinement of the interface. Surfactants and particles are usually applied to modulate interfacial properties in order to avoid droplets coalescence in most microfluidics applications [79].

Several devices, using co-flow, flow focusing and cross-flow, different materials and treatments, have already been proposed to generate droplets [80, 81, 82, 83, 84, 85, 86, 87, 88, 89, 90].

In 2005, Utada et al [2] developed a microcapillary device for generating double emulsions in a single step (Fig. 2.5) allowing control of the outer and inner drop sizes and the number of droplets encapsulated in each larger droplet. It consisted of an injection and a collection cylindrical glass capillary nested into the opposite ends of a square glass capillary .

In this device, an inner fluid flows through the injection capillary and is embraced by an immiscible second fluid (middle phase) that flows through the interstices between this cylindrical capillary and the square one. The middle phase is, in turn, engulfed by a third fluid (outer phase) that flows in the opposite direction

through the interstices between the collection tube and the square one. Thereby, W/O/W or O/W/O templates can be formed inside the collection capillary.

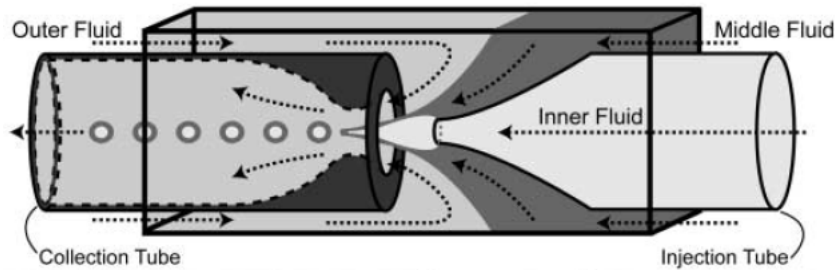


Figure 2.5: Microfluidic device developed by Utada et al. for generating double emulsions. Reproduced from [2].

The authors defined two flow regimes with which it would be possible to form double emulsions: dripping and jetting. The dripping regime produces drops close to the entrance of the collection tube while the jetting regime produces a long jet in the collection tube and the drops are formed downstream. They argue that the second is typically quite irregular, resulting in polydisperse droplets whose diameter are much greater than that of the jet [2].

The control of the size and shell thickness of the droplets is enabled by adjusting the flow rates of the phases until the inner and middle fluids are simultaneously dripping or simultaneously jetting [2]. In dripping mode, the viscous force, exerted by the continuous phase, exceeds the pinning force arising from the interfacial tension [21]. The jetting mode, can either be narrowing, when the viscous force generated by the continuous phase is greater than the interfacial force, or widening, when the inertial forces of the jet dominate the interfacial tension force. The first one is related to a thin and long jet that breaks into small drops while the second, to the deceleration of the jet [21].

Thus, drops are formed over a range of flow conditions, which can be described by two dimensionless numbers for each fluid phase: the Capillary number, which relates viscous to interfacial tension forces, and the Weber number, which relates inertial to interfacial tension forces [89]. Adjusting these dimensionless numbers, the formation of outer drops with multiple inner drops is also possible [91].

Once the double emulsion templates are generated, microcapsules can be formed by solidifying the middle phase to form shells that isolate the inner content from the medium. Hence, the structure of a microcapsule is highly dependent on the shape and composition of the double emulsion droplet, as discussed before.

There are two commonly used approaches to form shells: polymerization and solvent evaporation [7]. Polymerization consists on using a monomer solution as middle phase that solidifies when in contact with a cross-linker that can be in solution

in any phase. In this case, the solidification of the shell is associated with an increase in the complex shear modulus. It can happen naturally after enough time has elapsed [64] or it can be accelerated by triggers such as UVlight [17, 92] or temperature [93]. On the other hand, solvent evaporation consists on using a dispersion of the desired shell material (polymer, colloidal particles...) in a volatile solvent as middle phase and letting it evaporate to form the shell network [94].

W/O/W double emulsions have been widely used as templates for microcapsules, because their aqueous core provide an ideal environment for the dissolution of hydrophilic compounds, whereas the microfluidic formation of O/W/O templates for the encapsulation of hydrophobic compounds has been less reported. This fact can be associated to: (i) the shear-thinning behavior of aqueous polymer dispersions used to form O/W/O templates, which may hinder the flow stabilization; (ii) the difficulty on achieving the continuous dripping flow regime due to the high viscosity of the inner and outer oil phases; (iii) the difficulty to choose the ideal surfactant to stabilize each interface, as well as the oil-types to compose the inner and outer phases; (iv) the scarce or incipient alternatives to solidify water-based polymers, as well as to control their crosslinking rate and (v) the continuous phase of the final microcapsules dispersions being an oil phase, which may be a limiting factor to some applications.

The drawbacks related to microfluidics production of microcapsules include the size range, which is limited to the order of tens or hundreds of micrometers, while some applications require smaller capsules, and the low production rate once it is hard to upscale the process while maintaining monodispersity [7].

To reduce the size of microcapsules it would be necessary to use smaller capillaries. Such small tubes imply working with prohibitively large pressures or very small and hardly achieved flow rates. This could not be circumvented yet [7].

Attempts have been made in order to accelerate the production of microcapsules by operating glass or PDMS devices with multiple parallelized droplet makers [95, 96, 97]. Besides that, alternative fabrication technologies, such as 3D printing, rapidly advance and open up new possibilities to the fabrication of more advanced parallelized devices [8]. High throughput production will bring microfluidics closer to industrial applications.

2.4

Gellan gum

As mentioned before, the material used to form the shell of capsules is strongly related to their applications and mechanical properties. The ideal type of material can be defined according to the required trigger that will be applied to release the charge.

Gels are usually used as shell formers. They are soft semi-solid materials formed by a liquid dispersion medium or solvent and the gelling agent or gelator [98].

Alginates are the most used water soluble gelling agents to form beads and capsules due to their low cost, low toxicity and ease of use [9, 17, 18, 19, 20]. Alternatively, gellan gum is a biocompatible polymer that can be used to produce hydrogels that are stronger and less permeable than alginate-based ones. It is a linear, anionic, and high molecular weight exopolysaccharide secreted by the bacterium *Sphingomonas elodea* with some valuable characteristics such as malleability and mucoadhesive ability [99]. Its commercial potential was firstly identified in 1978 by Kelco [100].

There are two forms of gellan gum: the acetylated (native) form, known as high acyl gellan gum, and the deacetylated form, known as low acyl gellan gum. The second is the most common and most commercially available [3]. The chemical structure of both forms are showed in Figure 2.6. The high acyl form produces more elastic gels, while the low acyl form generates strong and brittle gels [20].

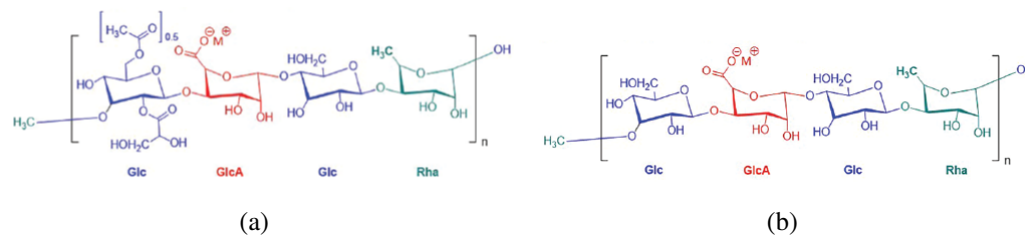


Figure 2.6: Chemical structure of the repeating unit of (a) acetylated or high acyl form of gellan gum and (b) deacetylated or low acyl gellan gum form, both reproduced from [3].

The gelation process of gellan starts with the formation of double helices generated from the initial disordered coil (chain ordering). Then, stable self-supporting structures can be formed depending on the stimuli (temperature, pH, ion presence,...), leading to a porous, branched network (chain association) [4, 100, 101, 102, 103]. Figure 2.7 illustrates this process.

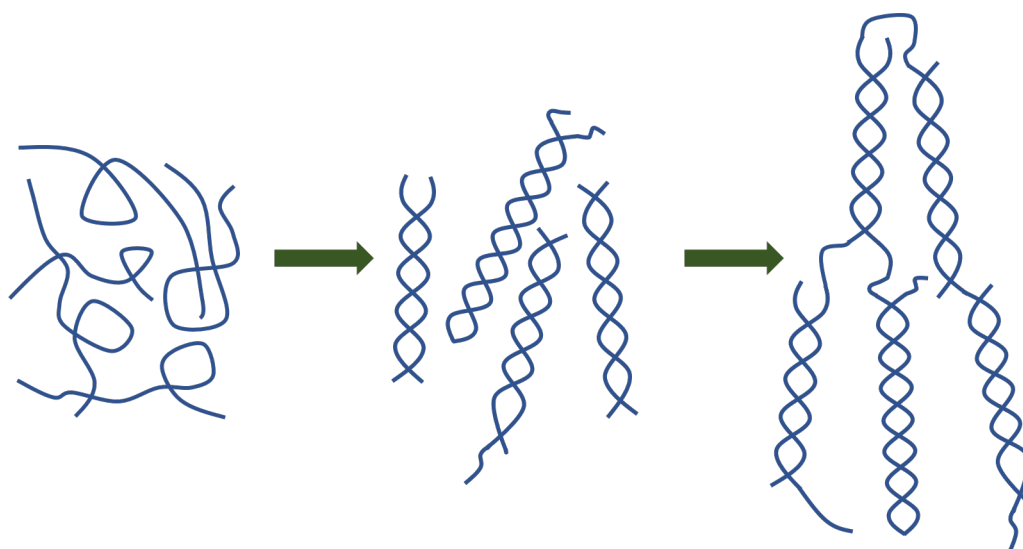


Figure 2.7: Gradual transformation of gellan gum from aqueous solutions. Based on [4].

As a naturally thermoresponsive polymer, gellan exhibits upper critical solution temperatures, transitioning from a disordered solution state (first stage illustrated in Fig. 2.7) to a gel state upon cooling as the coil to double-helix transition occurs (second stage indicated in Fig. 2.7) [98, 99, 102, 104, 105]. The gelation temperature can vary depending on the processing conditions, molecular weight and the presence of cations [99, 102, 106, 107].

To form a true gel, aggregation of helical sequences is necessary (third stage illustrated in Fig. 2.7). Cations stabilize gel structures by connecting the double helix chains (ionotropic process) [99]. Thus, gelation is influenced by the chemical nature and quantity of cations present in solution.

Monovalent cations give rise to a gelation based only on screening of the electrostatic repulsion between the ionized carboxylate groups on the gellan chains that hinder the tight bond of helices. On the other hand, divalent cations, promote an additional chemical bonding with carboxylate groups of gellan chains [3, 99, 100, 104, 105, 108]. Hence, divalent cations, such as Ca^{2+} and Mg^{2+} , promote a more efficient gelation than monovalent cations, such as Na^+ and K^+ . Besides that, gels induced by divalent cations have greater thermal stability [100]. However, very high salt concentrations lead to a decrease in gel strength [100].

Reduction in pH can also induce gelation of gellan gum because it reduces the charge on the helix chains allowing them to form stable aggregates [101, 109]. Similarly to what happens at high concentrations of salt, very acid environments also cause excessive aggregation and weaken the gel [100].

Despite being stable at ambient temperature or refrigerated, syneresis, or release of fluid, from the gellan gels can happen specially at low concentrations of

polymer [100].

Matricardi et al. [110] demonstrated that the type of crosslink (physical or chemical) used to form a gellan gel influences not only their strength but also the delivery of loaded model molecules profiles, with the release from the physical hydrogels being faster than that from the chemical hydrogels when a dissolution medium is added.

Due to its properties, gellan gum can be used in several applications. It is biocompatible and approved by the USFDA, Anvisa and European Union acting as a stabilizer, thickening and gelling agent in a wide variety of products. Gellan gels can resist to acidic environments. Besides that, due to their transparency, they do not affect the appearance of foods in which they are added [111]. Gellan gum can substitute gelatin in marshmallows and sweets, for example, with advantages of making them vegetarian, resistant to high temperatures such as the ones required to make hot cocoa or bake a cake and do not stick to one another in ambient temperature [100]. Gellan beads are also used as carries of savory or seasoning ingredients and to stabilize milkshakes, ice creams and yogurts [100].

Besides applications in food industry, gellan is also used as a structuring agent in cosmetics products such as creams, lotions, hair care products and toothpastes [100].

The potential of gellan gum for tissue engineering has also been studied [103, 105, 112]. It can be combined with other polymers and enriched with cations, for example, to promote the development of a bone-like apatite layer when placed in physiological conditions without triggering severe immune responses [113] or coupled with cells and implanted for the treatment of articular cartilage defects [114, 115].

The use of gellan gum-based hydrogels in intervertebral disc repair as acellular or cellular substitutes of the nucleus pulposus has also been evaluated once they showed to be non-cytotoxic to rat lung fibroblasts cells [116].

Biopolymers are also commonly applied to drug delivery. Studies demonstrated the feasibility of forming gellan gels in the stomach of rats and rabbits by the oral administration of aqueous solutions. The acidic environment of the stomach promotes the *in-situ* gelation resulting in depots for the release of theophylline [117] or paracetamol [118] over a period. The bioavailability obtained with this process is similar or higher than the one achieved with commercial oral formulations [117, 118]. However, most available studies regarding gellan use for triggered release focus on forming gel particles with embedded hydrophilic components that can be suspended in aqueous medium.

In 1996, Alhaique et al. [119] were able to prepare capsules by gelation of gellan gum around drops containing starch, calcium chloride and a model drug.

They showed that gellan is suitable for the formulation of sustained release capsules. Furthermore, they argued that the rate of delivery in water is mostly affected by solvent uptake once they observed that the increase of the average weight of capsules (due to solvent uptake) profile has the same trend of the delivery profile. Besides that, the capsules showed to be more efficient in sustaining the delivery of the model drugs than gellan beads. Though, oil was added to the bead composition to slow the delivery rate to values similar to that of the capsules.

As discussed, gellan gum is valuable for different uses and areas. However, besides its versatility and several possible triggers, it has only been scarcely explored as shell material.

In the present study, gellan gum microcapsules are produced by microfluidics for the first time using a device similar to the one proposed by Utada et al. [2] and presented above. The operability window based on the flow rate of each phase at which the continuous dripping flow regime occurs and monodispersed double emulsions are formed with a single inner phase core is defined. Moreover, it is shown how the microcapsule diameter and shell thickness can be controlled by changing the flow parameters. The produced microcapsules are used in different applications, discussed in chapters 4, 5 and 6.

3

Microcapsules production by microfluidics

3.1

Gellan-based microcapsules

To compose the double emulsion templates that become microcapsules, gellan gum is used as middle phase to form the polymeric shell while sunflower oil is used as the inner content and also as the continuous phase in which they are suspended. Thus, the microcapsules produced are biodegradable and elastic.

The middle phase consist of a mixture of 0.5 wt% of low-acyl gellan gum Kelcogel CG-LA (CP Kelco Brasil S/A, Brazil) and 2 wt% of polyoxyethylene sorbitan monolaurate, Tween20 (Sigma-Aldrich, USA) surfactant, in ultrapure water with resistivity 18.2 M Ω /cm (Direct-Q3 UV System, Millipore Co., USA). This phase is prepared shortly before starting the microcapsules production and the mixture stays under magnetic stirring at 80°C for 10 min .

The inner phase is a refined commercial sunflower oil (Liza, Cargill Agricola S.A., Brazil) labeled with an orange food-grade dye and a fluorescent pigment called oil Glo 22 for visualization purposes only.

The continuous phase, in turn, is a sunflower oil dispersion containing 1 wt% of calcium acetate (Sigma-Aldrich, USA) and 5 wt% of polyglycerol-polyricinoleate emulsifier commercially named Grinstead PGPR super (Danisco Brasil, Brazil).

The O/W/O templates formed through microfluidics, as will be explained later, are transformed into monodispersed biopolymer-based microcapsules through gelation of the middle phase induced by the calcium ions present in the continuous phase, according to what was discussed in Chapter 2.

Before being used, all phases were properly characterized by density, rheological and interfacial tension measurements, summed up in Table 3.1.

The density (ρ) of each phase was measured in a digital densimeter (model DMA 4200M, Anton Paar, Austria) at 25 °C. The measurement is based on the oscillating U-tube principle: the U shaped tube is excited and starts to oscillate at a certain frequency depending on the filled-in sample. Then the density of the sample is calculated based on this frequency. Three measurements were made for each fluid and the average is presented in Table 3.1.

Flow curves for all fluids were performed in a stress-controlled rheometer

(model DHR-3, TA Instruments, USA) using a stainless steel Couette geometry. The shear rate ranged from 1 to 1000 s^{-1} while the shear stress and viscosity were measured. The viscosity as a function of shear rate for the three phases is presented in Fig. 3.1. The inner and continuous oil phases show Newtonian behavior, $\mu_i = 55.3$ mPa.s and $\mu_o = 73.9$ mPa.s, which is a typical flow behavior of vegetable oils. The viscosity difference between the oil phases is mostly associated with the presence of calcium acetate in the continuous phase. The biopolymer-based phase, in turn, showed shear thinning behavior, with the viscosity varying from $\mu_m = 21.6$ mPa.s to $\mu_m = 291.4$ mPa.s in the range of shear rates explored. Therefore, the viscosity value of the middle phase changes with the flow rate and may affect the flow regime in the droplet formation region.

We estimated a deformation rate value of approximately 10^3 s^{-1} at the droplet breakup region.

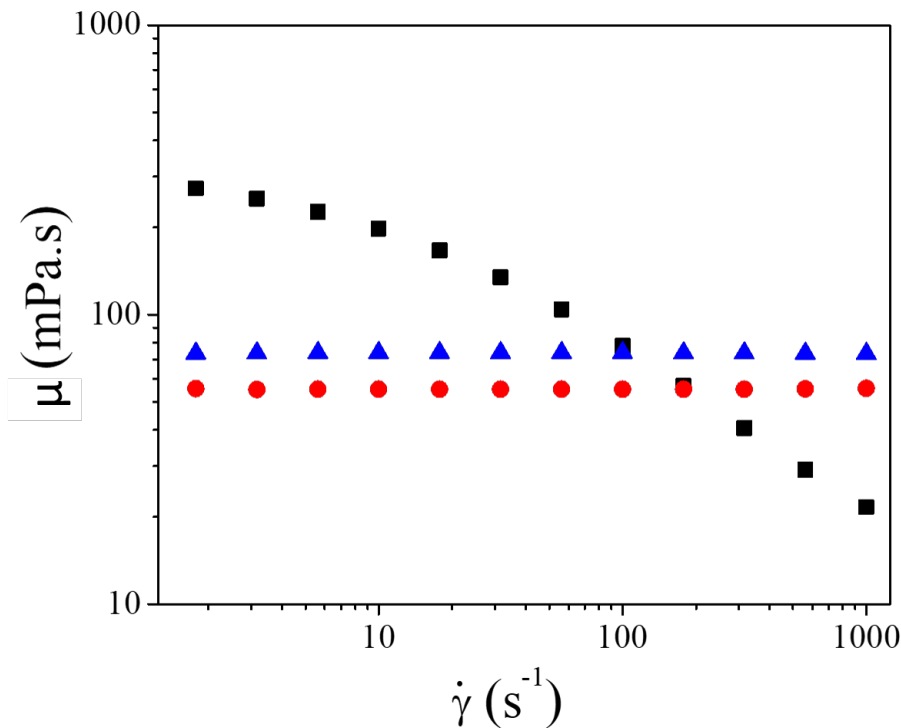


Figure 3.1: Flow curves at 25 °C: (●) inner phase, (■) middle phase and (▲) continuous phase.

The interfacial tensions (σ) were measured by Wilhelmy plate method, using a digital tensiometer (model DCAT 25, DataPhysics, Germany). In this static classic method, a thin plate is oriented perpendicularly to the interface and immersed into the liquids. Then the gravitational force of the lamella that forms when the Wilhelmy plate stands at the interface (F) is measured by a tensiometer or a microbalance and

the surface tension is calculated using the Wilhelmy equation (Eq. 3-1), where L is the wetted perimeter and θ is the contact angle.

$$\sigma = \frac{F}{L \cos \theta} \quad (3-1)$$

It is seen in Table 3.1 that there is a reduction of the interfacial tension between the middle and continuous phases, $\sigma_o = 2.7$ mN/m, in comparison with the interfacial tension between middle and inner phases, $\sigma_i = 5.4$ mN/m. This difference is explained by the presence of PGPR and Tween20 which are emulsifiers acting to favor the formation and stabilization of O/W/O templates, as explained in Chapter 2. Apart from that, calcium acetate can also act as a co-surfactant, promoting an additional stability for the O/W/O droplets before their full gelation [121].

| Phase | ρ (kg/m ³) | μ (mPa.s) | σ (mN/m) |
|----------------------|-----------------------------|---------------|----------------------|
| Inner (O_i) | 752.8±0.1 ^b | 55.3 | 5.4±0.3 ^a |
| Middle (W) | 1019.1±0.9 ^a | 21.6-291.4 | |
| Continuous (O_o) | 755.2±0.2 ^b | 73.9 | 2.7±0.2 ^b |

Table 3.1: Density (ρ), viscosity (μ) and interfacial tension (σ) of the phases at 25 °C. Different lowercase letters (a-b) represent significant differences ($p < 0.05$) between the phases.

3.2

Experimental set-up and methodology

3.2.1

Microfluidic device

To produce the double emulsion templates that will generate gellan-based microcapsules, three-dimensional coaxial microfluidic devices were used based on the configuration proposed by Utada et al. [2]. A sketch of the device is showed in Fig. 3.2 and a photo in Fig. 3.3. With this device it is possible to generate O/W/O double emulsions in a single step, precisely controlling the outer and inner drop sizes, as discussed before.

A step by step explanation of how to built the microfluidic device is described below.

1. Two cylindrical glass-capillaries (World Precision Instruments Inc., USA), with inner and outer diameters of 0.58 mm and 1 mm, are tapered to an inner diameter of approximately 20 μ m with a micropipette puller (model P-1000, Sutter Instrument Co., USA) that simultaneously heats and pulls them.

2. The tips are then carefully sanded to the desired final inner diameter. The one that will be the collection capillary (right capillary in Fig. 3.2) has a larger inner tip diameter (ϕ_c), usually on the order of 10^2 micrometers, while the other is called injection capillary (left capillary in Fig. 3.2) and has a smaller inner tip diameter (ϕ_i), usually on the order of 10^1 micrometers.
3. Both capillaries are surface treated for 60 minutes. The collection one is treated with a commercial rain repellent Glass Shield (Inove Pack do Brasil, Brazil) to render a hydrophobic surface while the injection one is treated with a polyelectrolytes solution composed of 1 wt% of poly(acrylamide-co-diallyldimethyl-ammonium chloride) (Sigma-Aldrich, USA) and 2 mol/L NaCl to render a hydrophilic surface. 2-[methoxy(polyethyleneoxy)6-9propyl]trimethoxysilane was also tested as a possible hydrophilic treatment but it led to channel clogging implying in disposing the entire microfluidic device.
4. Then, a square capillary with inner dimension of 1.05 mm (Atlantic International Technology Inc., USA) is fixed to a glass microscope slide with Epoxy resin (Devcon Corp., USA).
5. The two cylindrical glass-capillaries are inserted into the opposite ends of the square capillary and glued with Epoxy resin. Because the outer diameter of the cylindrical capillaries is approximately equal to the inner dimension of the square capillary, it is possible to achieve a precise alignment of the cylindrical capillaries for a truly coaxial geometry and also to fix a desired separation distance (l) between them.
6. Three stainless steel blunt dispensing needles of inner and outer diameters 0.66 mm and 0.91 mm respectively (model 304, McMaster-Carr, USA) were placed at the junctions between capillaries or at their ends, and fixed to the slide with Epoxy resin.

In the three-dimensional coaxial microfluidic devices, the inner phase flows through the injection capillary, while the middle and continuous phase flow in opposite directions through the interstices between the cylindrical and square capillaries, as sketched in Fig. 3.2.

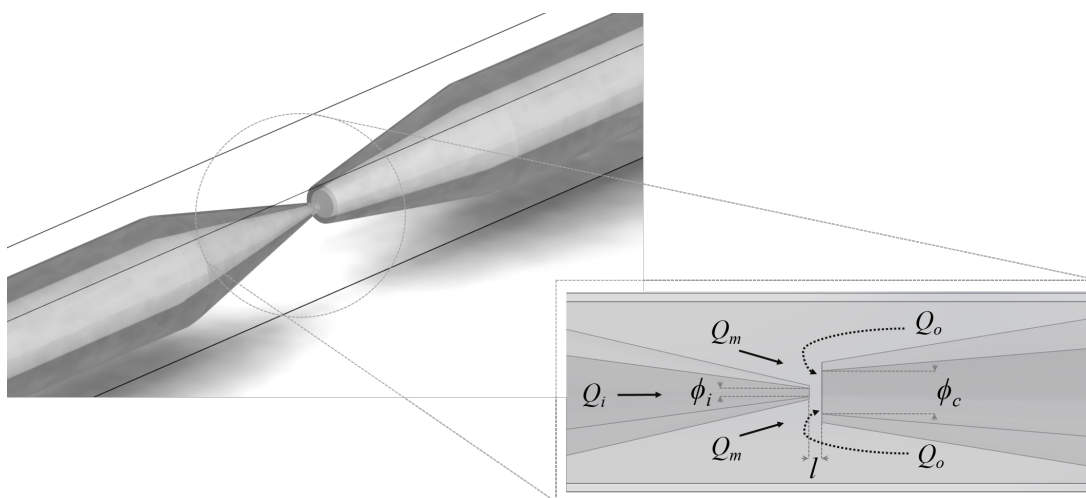


Figure 3.2: Perspective view of the coaxial glass-capillary device with detail of the droplet generation region. Q_i , Q_m and Q_o are the flow rate of inner, middle and continuous phases, respectively.

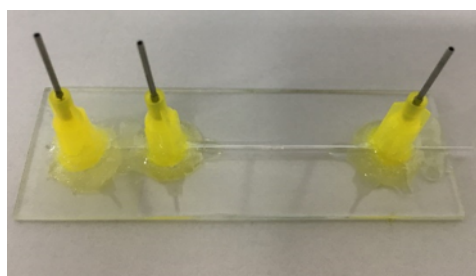


Figure 3.3: Coaxial glass-capillary device.

In this research, several microfluidic designs with different values of ϕ_c , ϕ_i and l were tested, including devices with the tip of the injection capillary inserted into the collection one (designs F and G), as reported in Table 3.2. However, it was not possible to form microcapsules with all of them and the ideal intermittent dripping regime necessary to form monodispersed templates could only be systematically achieved with two designs, named A and B. Thus, they were both used in a further study to determine the conditions required to achieve monodispersions.

| Design | ϕ_i (μm) | ϕ_c (μm) | l (μm) |
|--------|----------------------------|----------------------------|-----------------------|
| A | 80 | 350 | 120 |
| B | 50 | 250 | 75 |
| C | 50 | 150 | 75 |
| D | 50 | 100 | 75 |
| E | 50 | 250 | 35 |
| F | 50 | 250 | -75 |
| G | 50 | 400 | -75 |

Table 3.2: Geometric parameters of the designs used. ϕ_i and ϕ_c are the inner diameter of the injection and collection capillaries, respectively, and l denotes the separation distance between them. Only designs A and B were successfully used to form monodispersed O/W/O templates.

It is worth highlighting that, due to the handmade nature of these devices, any difference on the final diameter of the sanded tips or misalignment between the cylindrical capillaries can affect or even hinder the formation of double emulsion templates.

3.2.2

Experimental set-up

The O/W/O template formation was monitored within the microfluidic device using an inverted microscope (model DMi8, Leica Microsystem, Germany) equipped with a high speed camera (model Fastcam SA-3, Photron, USA) and a computer.

The flow rates of each one of the three phases (Q_i , Q_m and Q_o) were controlled by three syringe-pumps (model Pump 11) from Harvard Apparatus, USA. Three BD plastic syringes and four flexible hoses with an outer diameter of 0.052" and an inner diameter of 0.034" were used. Three of the hoses connected the dispensing needles of the syringes to the device dispensing needles to inject the fluids and one of them connected the collection capillary to the recovery vial to collect the capsules.

Figure 3.4 shows the experimental set-up and Fig. 3.5 a simplified scheme of it.

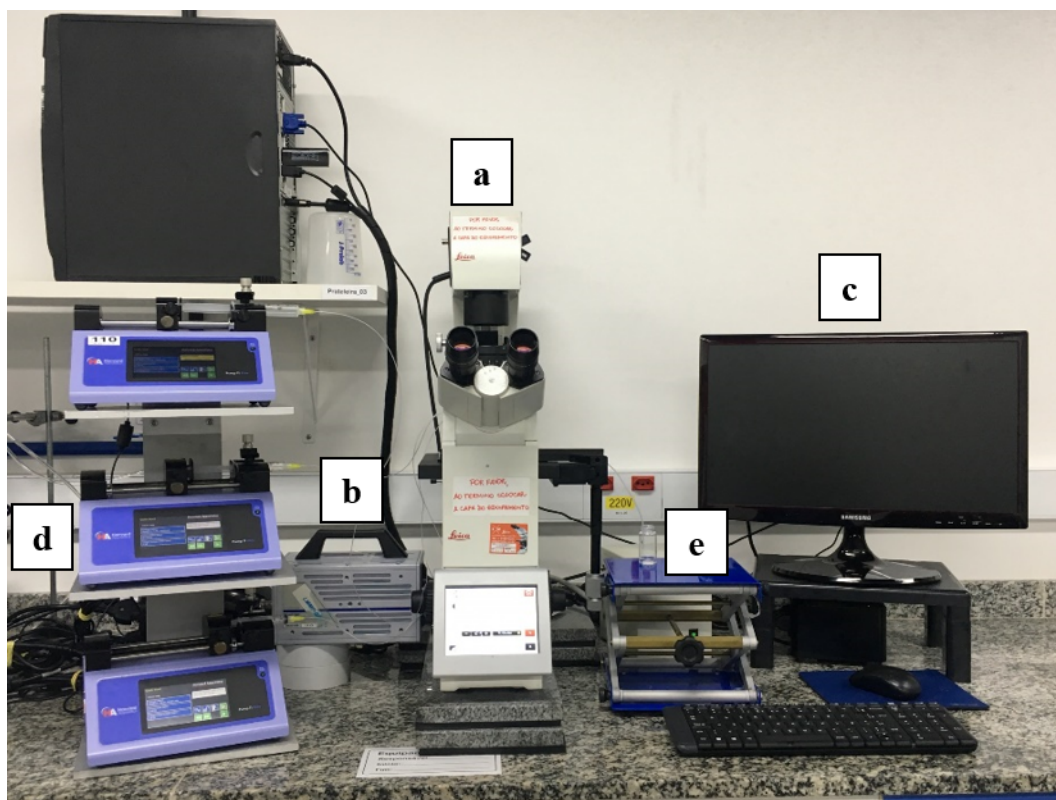


Figure 3.4: Experimental set-up for microcapsules production, including: (a) an inverted microscope; (b) a high speed camera; (c) a computer; (d) three syringe pumps and (e) a collection vial.

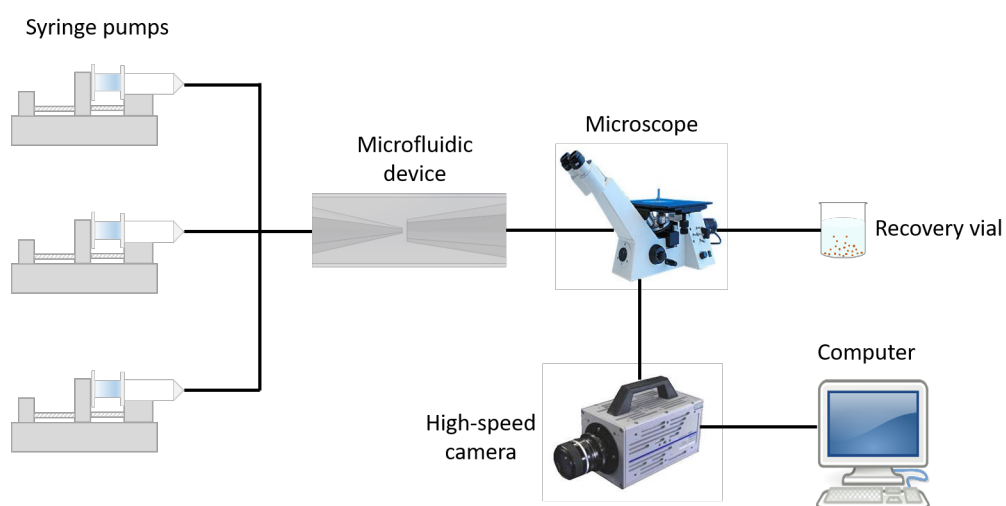


Figure 3.5: Scheme of the experimental set-up for microcapsules production.

3.2.3

Microcapsules recovery

Because many applications for the gellan gum microcapsules require an oil-free capsular dispersion, a recovery process was developed to change the continuous phase from sunflower oil to acetate buffer.

In the first step, the microcapsules are collected in a glass vial containing a small volume of hexane for no more than 5 minutes. After that, a small volume of acetate buffer (0.074 mol/L, pH 4.5) is carefully added to the vial with a pipette. Because of their density, the capsules go to the interface between the hexane, on top, and the acetate buffer, on the bottom. Then, the hexane excess containing the oil from the continuous phase is removed with a pipette and the residual hexane is evaporated at room temperature during 24 hours. This ensures that, in the end, we have a suspension of microcapsules in an aqueous media. Acetate buffer is used instead of pure water because gellan gum is more stable at acid pH's.

If the application requires an oily system, the microcapsules can simply be collected and maintained in sunflower oil.

This recovery process is very relevant because it broadens the possible applications for the microcapsules, since it enables them to be dispersed in hydrophobic and hydrophilic media.

3.2.4

Microcapsules size and shell thickness

After recovery, every batch of microcapsules was characterized in relation to microcapsule size and shell thickness. To this end, micrographs of the microcapsules in the acetate buffer were obtained using an inverted microscope (model DMI8, Leica Microsystems, Germany). Then, the micrographs were processed using the software Leica Application SuiteX (Leica Microsystems, Germany) to determine the outer (D) and inner (D_{in}) diameters of at least 10 microcapsules of each batch, as exemplified in Fig. 3.6. The shell thickness was calculated from Eq. 3-2. The polydispersity of the capsular systems is expressed in terms of coefficient of variation (CV) relating standard deviation to mean diameter.

$$t = \frac{D - D_{in}}{2} \quad (3-2)$$

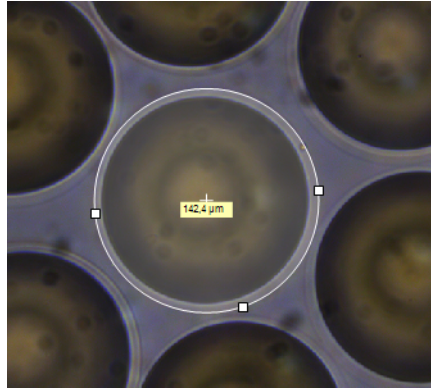


Figure 3.6: Microcapsule diameter of $142.4 \mu\text{m}$ being measured in Leica Application SuiteX software.

3.3

Operability window

In the microfluidic process presented, due to the hydrophilic nature of the treated injection capillary, the inner oil phase (O_i) flows through the tip of the injection capillary without wetting its outer surface, while the aqueous biopolymer middle phase (W) flows along the outer wall of the capillary, coaxially shielding the innermost stream. In addition, the hydrophobic treatment of the collection capillary ensured that the middle phase flows through the center of the collection capillary without contacting the glass-capillary wall.

The mechanism of O/W/O templates formation in coaxial glass capillary devices is governed by the interactions between viscous, inertial and interfacial forces, as discussed in Chapter 2. Therefore, the flow dynamics is a function of the Capillary number, which is the ratio of viscous drag forces to surface tension forces acting in the interface between two immiscible liquids, and the Weber number, which relates the inertial forces to the forces resulting from surface tension of each phase [79, 89].

The desired dripping regime is the result of an absolute instability, wherein the viscous and capillary force balance is such that both interfaces, one between the inner and middle phases (O_i/W) and the other between the middle and continuous phases (W/O_o), break simultaneously at the same spatial location and frequency, which depends on the flow parameters, leading to the formation of monodispersed droplets [21]. This regime only occurs at a small range of flow rates and the flow rates of the inner (Q_i), middle (Q_m), and continuous (Q_o) phases have a strong effect on the breakup dynamics of the two coaxial interfaces.

The effects of the flow rates of each phase on the O/W/O template generation for each of the two designs explored were investigated using the same device, to avoid any small variation in flow velocity associated with small differences in the

geometry from device-to-device of the same design. Then, the range of parameters at which the ideal intermittent dripping flow regime is observed and monodispersed microcapsules with a single inner core are produced were explored (see Fig. 3.7). Moreover, it was determined how the microcapsule diameter and shell thickness vary with the flow parameters inside the operability window. At each condition, 10 microcapsules were measured. The average value and the standard deviation (error bars in the plots) are reported.

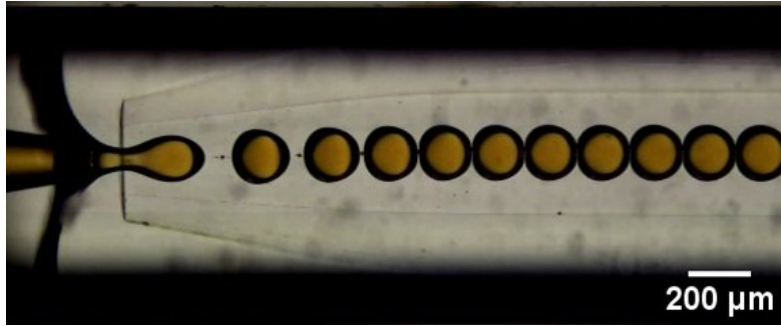


Figure 3.7: O/W/O template formation in the ideal intermittent dripping regime.

3.3.1

Microfluidic design A ($\phi_i = 80 \mu\text{m}$, $\phi_c = 350 \mu\text{m}$ and $l = 120 \mu\text{m}$)

(a) At fixed $Q_i = 200 \mu\text{L/h}$

First, the value of the inner phase flow rate was fixed to $Q_i = 200 \mu\text{L/h}$ while the flow rates of the middle and outer phases varied over a wide range: $12.5 < Q_m < 450 \mu\text{L/h}$ and $500 < Q_o < 5000 \mu\text{L/h}$. The observed flow regimes are summarized in Fig. 3.8(a) as a function of the outer and middle phase flow rates and in Fig. 3.8(b), as a function of the outer (Ca_o) and middle (Ca_m) phase capillary numbers, respectively defined as

$$Ca_o = \frac{\mu_o Q_o}{\sigma_{mo}(\phi_c^2 - \phi_i^2)} \quad (3-3)$$

$$Ca_m = \frac{\mu_m(Q_m + Q_i)}{\sigma_{mo}\phi_i^2} \quad (3-4)$$

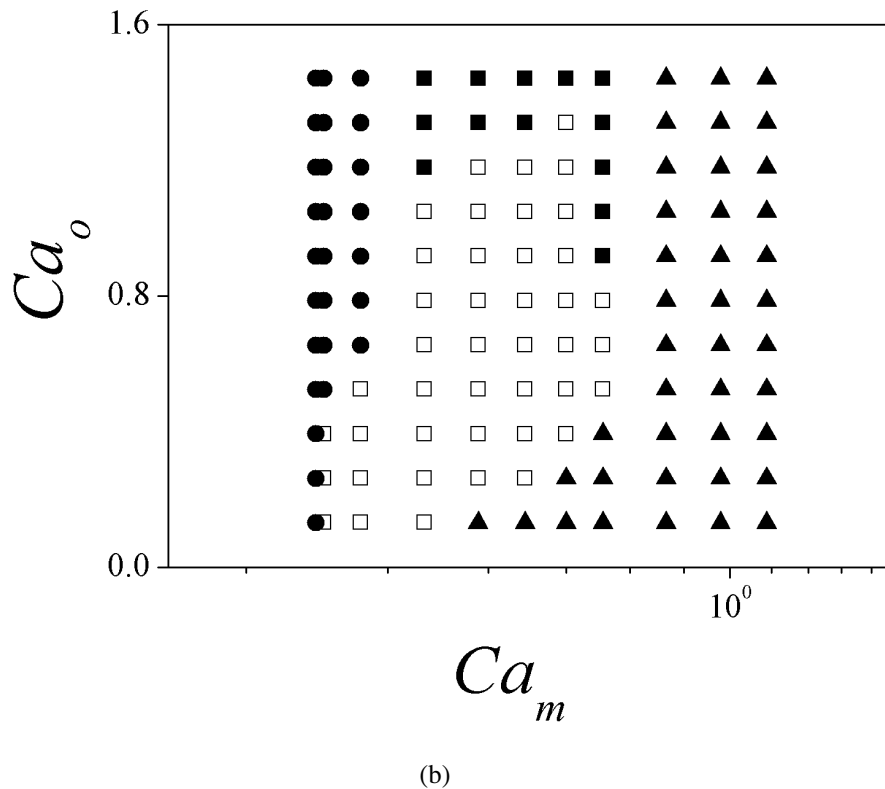
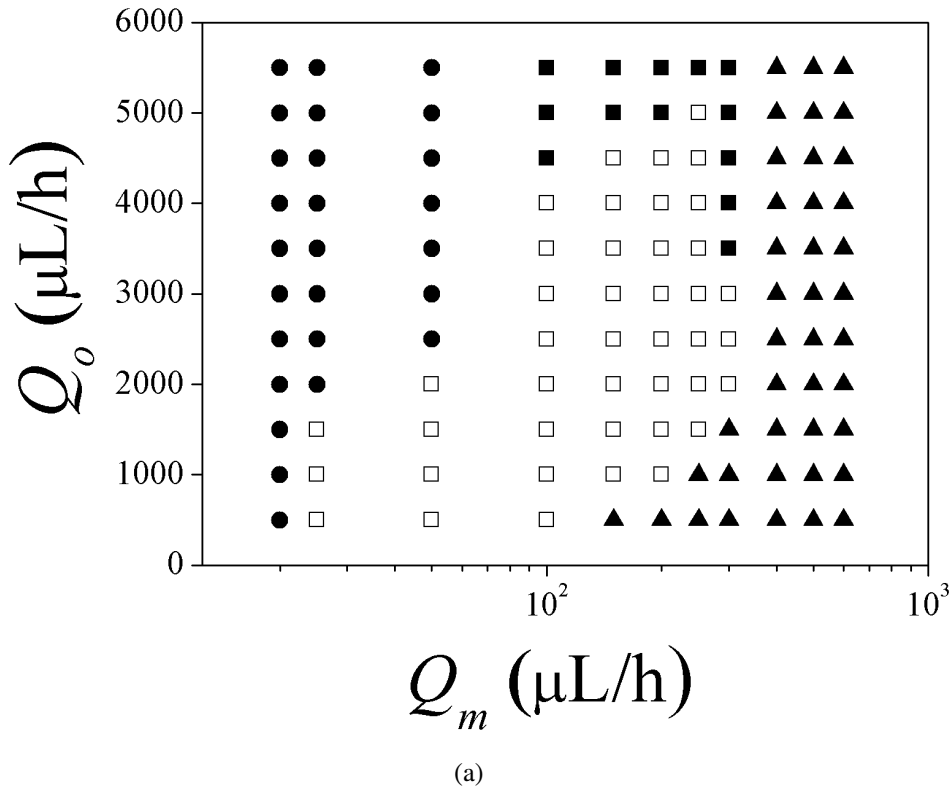


Figure 3.8: (a) Operability window as a function of the flow rates Q_m and Q_o at a fixed inner phase flow rate, $Q_i = 200 \mu\text{L/h}$ using Design A ($\phi_i = 80 \mu\text{m}$, $\phi_c = 350 \mu\text{m}$ and $l = 120 \mu\text{m}$) and (b) Operability window represented as a function of the outer and middle phases capillary numbers: (◻) monodispersed O/W/O templates, (▲) jetting regime, formation of double emulsion with multiple inner compartments, (●) formation of droplets containing only the middle phase without the inner core together with the formation of polydispersed microcapsules, (■) back flow regime, the outer phase invades the injection channels of the inner and middle phases.

The open symbols represent flow conditions at which the breakup of the inner and middle phases occurs simultaneously and at the same position, near the entrance of the collection capillary, as shown in Fig. 3.7. Double emulsion is generated with a single inner phase drop. This is the desired continuous dripping regime at which monodispersed microcapsules are produced. The filled symbols represent flow conditions that did not lead to the desired dripping regime.

The Reynolds Numbers of the outer and middle phases were calculated for each case following Eq. 3-5 and Eq. 3-6, respectively, and varied as following: $0.026 < Re_o < 0.4$ and $0.18 < Re_m < 0.8$.

$$Re_o = \frac{\rho_o Q_o}{\mu_o(\phi_c + \phi_i)} \quad (3-5)$$

$$Re_m = \frac{\rho_m(Q_m + Q_i)}{\mu_o \phi_i} \quad (3-6)$$

At a fixed value of the inner and outer flow rates, the formation of monodisperse O/W/O templates with a single inner core only occurs inside a certain range of the middle phase flow rate Q_m . If the middle phase flow rate is above a critical value, the inertial force of the middle and inner phases becomes comparable to the capillary forces. Thus, a long jet is formed and the drop breakup occurs far from the entrance of the collection capillary, in what is called the jetting regime [2, 90, 122]. At these conditions, the drop breakup is quite irregular leading to polydisperse capsules (Fig. 3.9(a)). Moreover, because of the relatively high middle phase flow rate, the breakup time of the inner phase is lower than that of the middle phase, leading to multiple inner phase drops inside a single middle phase drop (Fig. 3.9(b)). The flow conditions that correspond to the jetting regime are marked with the filled triangles in Fig. 3.8.

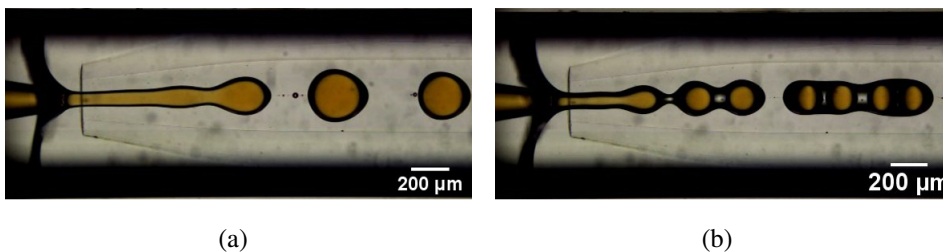


Figure 3.9: Jetting flow regime: (a) Polydisperse microcapsules formed far from the entrance of the collection capillary and (b) Microcapsules formed with multiple inner phase drops inside a single middle phase drop.

On the other hand, if the middle phase flow rate is below a critical value, the

shear force exerted by the outer phase along the interface is high, because of the large velocity difference between the outer and middle phases [96]. The high shear force associated with a very thin middle phase filament leads to breakup prior to the complete growth of the inner core and the formation of droplets containing only the middle phase without the inner core together with the formation of polydispersed microcapsules. These flow states are marked by filled circles in Fig. 3.8.

The production of monodispersed O/W/O double emulsion does not occur if the outer phase flow rate is very high (flow states marked by filled squares in the plots). At this condition, the inner and middle phases flow back into the injection capillary and through the interstices between the square and cylindrical capillaries, respectively, disrupting the desired periodic dripping flow.

In general, the range of the flow rates that led to formation of O/W/O templates was approximately 10x smaller than the one observed in the formation of the W/O/W templates [24, 66, 96, 123]. This fact is probably associated to the differences in viscosity ratio between the phases, interfacial tension of the fluids and tip diameter of capillary tube used, which are affecting synergistically on the force balance.

The operability windows can be used not only to define the region where the ideal dripping regime occurs but also to help defining the required flow rates to achieve a certain diameter and the shell thickness for the microcapsules being produced.

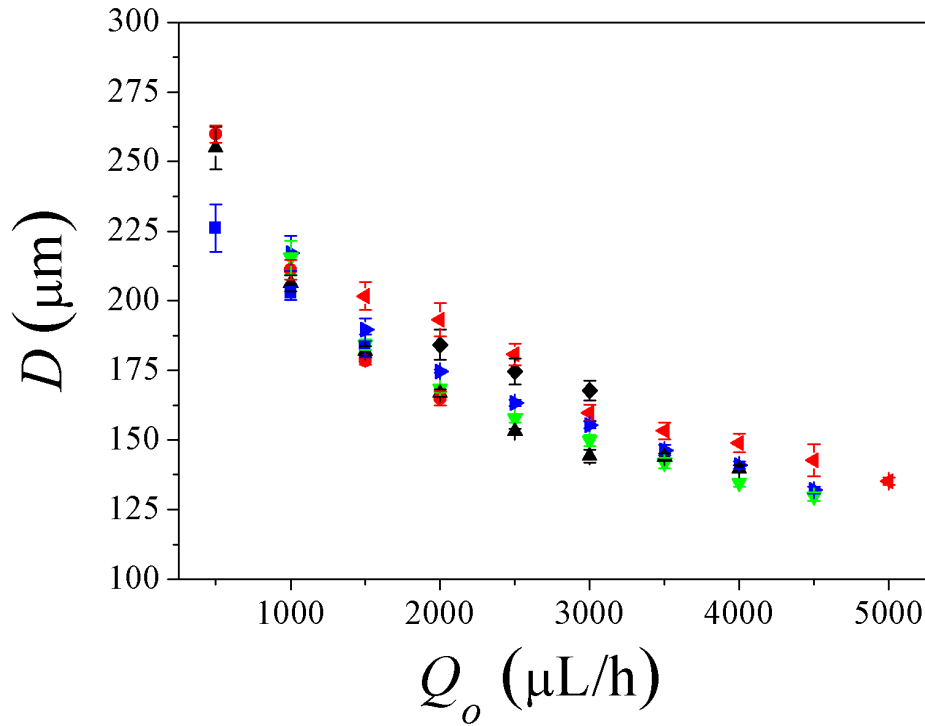
In fact, inside the operability window that led to the ideal dripping regime and the formation of the monodispersed O/W/O templates, it is possible to accurately control microcapsules diameter by changing the outer phase flow rate Q_o . As can be seen in Fig. 3.10, regardless of the value of the middle phase flow rate Q_m , the microcapsule diameter falls as Q_o rises. It happens because as Q_o increases, the viscous drag force between the continuous and middle phase also increases, causing the droplets to detach quickly from the injection capillary tube. Thus, smaller microcapsules are produced at higher frequencies. Similar behavior has been reported in the production of W/O/W double emulsion templates [2, 21, 66, 122, 124].

As explained before, for each batch of microcapsules, produced at different flow rates, at least 10 units had their diameters and shell thickness measured. For the range of flow rates explored ($25 < Q_m < 300 \mu\text{L/h}$ and $500 < Q_o < 5000 \mu\text{L/h}$) for device A with $Q_i = 200 \mu\text{L/h}$, microcapsules diameter ranged from 130 to 260 μm with a maximum coefficient of variation of 5% (Fig. 3.11). The data is represented in dimensionless form in Fig. 3.10(b), which shows the drop to collecting capillary diameter ratio as a function of the ratio of the outer phase flow rate to the sum of the middle and inner phase flow rates.

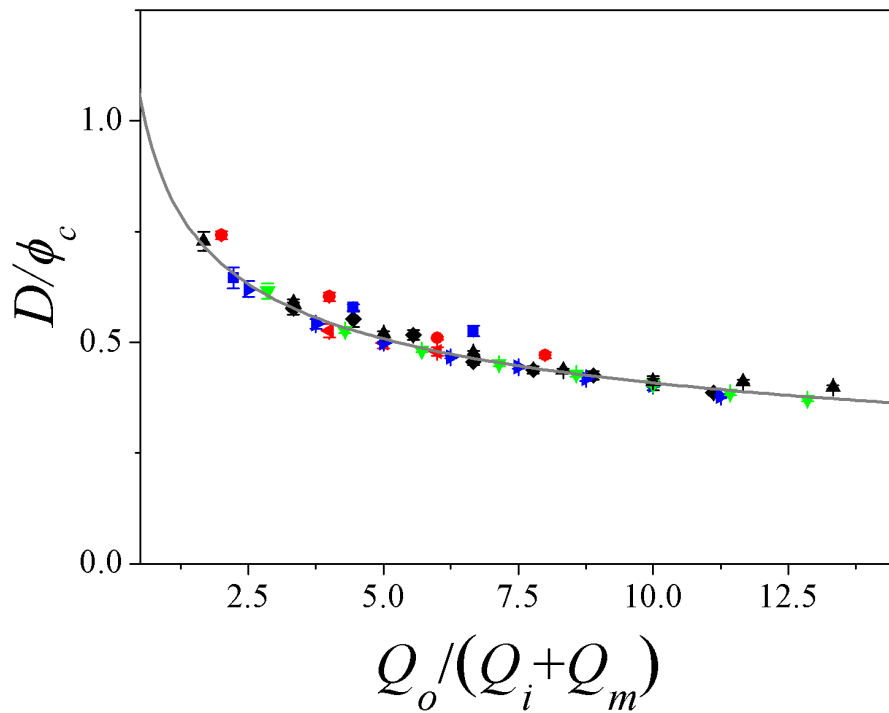
The drop diameter, in units of the collecting capillary diameter, obtained in our

set-up was approximately half of the values reported in the production of W/O/W double emulsion templates [122, 125]. The data for all values of Q_m collapse in a single power-law curve (Eq. 3-7) represented as a continuous line in Fig. 3.10(b). Vladislavjevic et al. [122] have reported similar power-law dependence, with an exponent of -1/3.

$$\frac{D}{\phi_c} = 0.85 \left(\frac{Q_o}{Q_m + Q_i} \right)^{-0.3} \quad (3-7)$$



(a)



(b)

Figure 3.10: (a) Microcapsule diameter (D) as a function of middle and outer phase flow rates (Q_m and Q_o) at a fixed $Q_i = 200 \mu\text{L/h}$ with Design A ($\phi_i = 80 \mu\text{m}$, $\phi_c = 350 \mu\text{m}$ and $l = 120 \mu\text{m}$) and (b) power-law fit of the diameter in units of the collecting capillary diameter (continuous line) as a function of $Q_o/(Q_i + Q_m)$: $Q_m =$ (■) $25 \mu\text{L/h}$, (●) $50 \mu\text{L/h}$, (▲) $100 \mu\text{L/h}$, (▼) $150 \mu\text{L/h}$, (►) $200 \mu\text{L/h}$, (◄) $250 \mu\text{L/h}$ and (◆) $300 \mu\text{L/h}$.

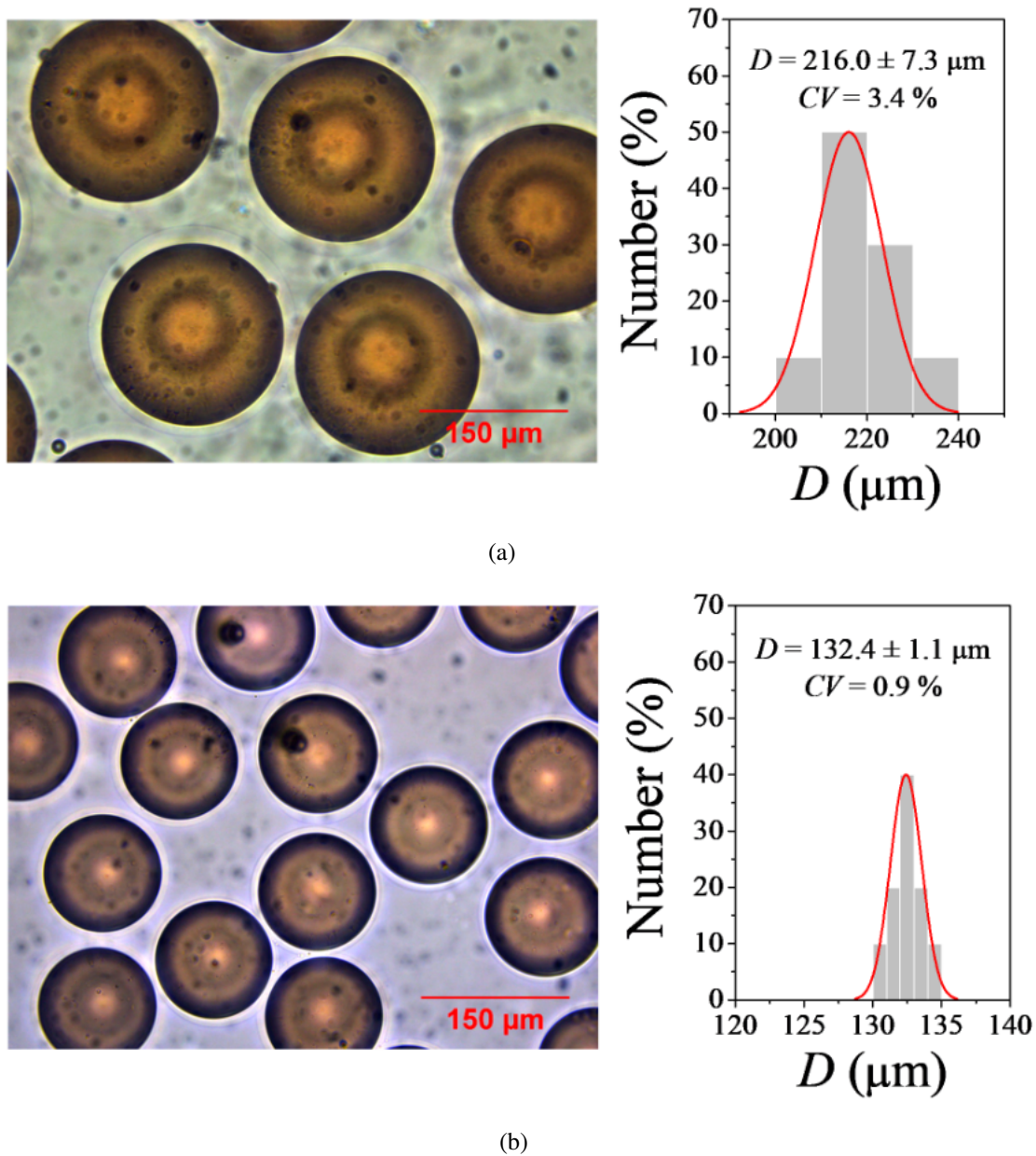


Figure 3.11: Examples of micrographs and particle size distributions of the microcapsules produced at different Q_o : (a) $Q_i = 200 \mu\text{L/h}$, $Q_m = 200 \mu\text{L/h}$ and $Q_o = 1000 \mu\text{L/h}$ and (b) $Q_i = 200 \mu\text{L/h}$, $Q_m = 200 \mu\text{L/h}$ and $Q_o = 4500 \mu\text{L/h}$.

The shell thickness of the produced microcapsules was calculated by the difference between the outer and inner drop radii. The results are shown in Fig. 3.12. As expected, at a constant outer phase flow rate, the shell thickness (t) rises as the middle phase flow rate is increased once there is more material available to form the shell. Because the droplet diameter changes with Q_o at a constant Q_m , it is instructive to plot the shell thickness in units of microcapsule radius $D/2$. Fig. 3.12(a) shows that the ratio thickness-radius, $t/(D/2)$, remains almost constant as the outer phase flow rate varies, except at the very high middle phase flow rate, near the boundary

of the operability window. The same behavior was reported by Nabavi et al. [126] for W/O/W double emulsion template.

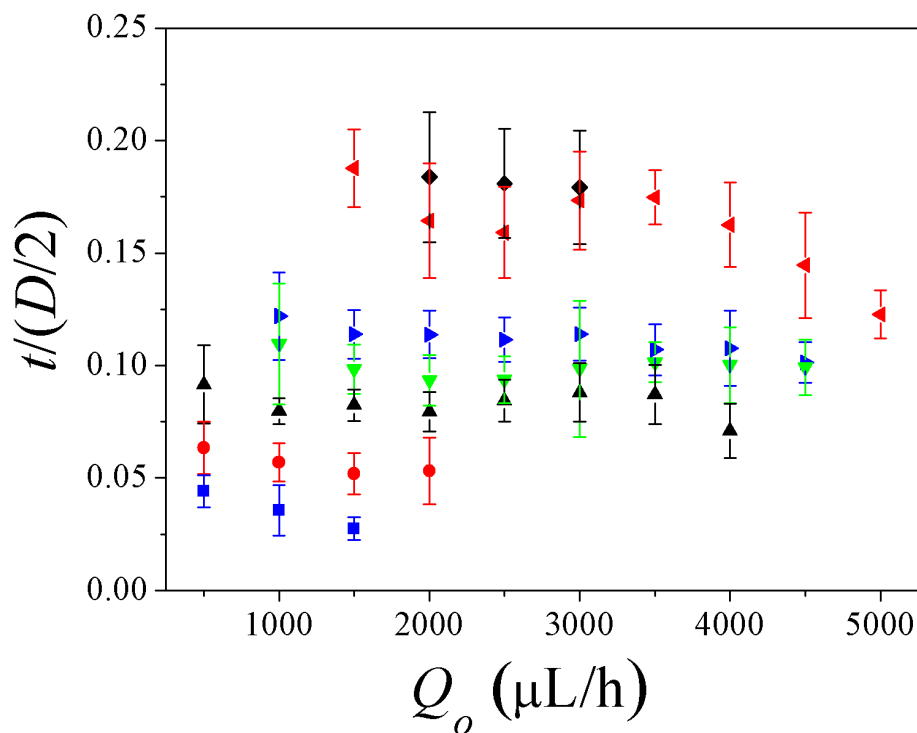
Lee and Weitz [124], Hennequin et al. [127], Vilanova et al. [123] and Chen et al. [24] have used mass balance to estimate the shell thickness as a function of Q_m/Q_i for W/O/W templates. The proposed equation assumes that the volume of the middle phase does not change during the solidification process and was able to accurately describe the measured shell thickness for their experiments.

In the production of microcapsules with hydrogel-based shell from O/W/O double emulsion templates, the volume of the middle phase is not constant during solidification process. This fact can be associated to the loss of aqueous mass from the shell during the gelation and recovery steps. Hydrogels based on gellan gum and divalent cations form bridges between the polymer chains, forming a porous structure that leaves significant amounts of free water in the gel network [128, 129]. Therefore, the thickness of the microcapsule shell is thinner than the thickness of the middle phase of the double emulsion template before solidification. We have incorporated the water loss phenomenon, quantified by the ratio α of the volume after and before solidification, in the mass balance to predict the shell thickness, according to Eq. 3-8. Fig. 3.12(b) presents the shell thickness to microcapsule radius ratio as a function of Q_m/Q_i at different Q_o and the curve fitting.

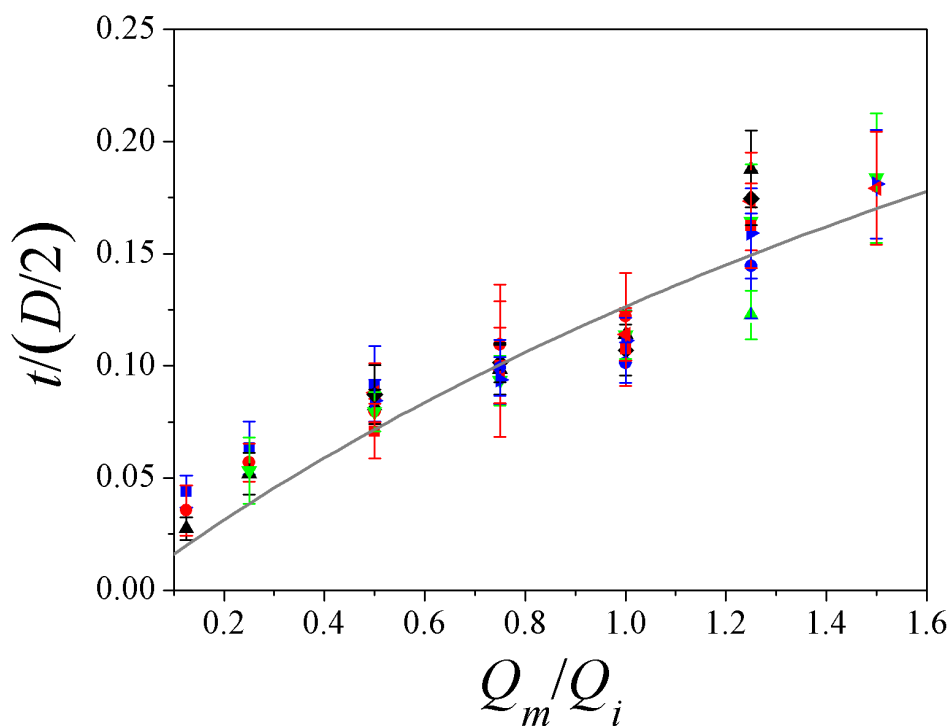
The amount of water loss from a hydrogel based on gellan gum is directly associated to the mechanism of gelation and polymer concentration. In general, gellan gum hydrogels at 0.5 wt% have shown variable amounts of water loss, ranging from 22% to 65% according to the pH condition applied [130]. To fit the data with Eq. 3-8, a water loss equal to $\alpha = 0.5$ (or 50%) was considered, which matches what was observed in a previous work that used calcium ions to gelify the gellan gum at 0.5 wt% [131].

For the specific conditions used in this study, the minimum shell thickness achieved was of approximately 3 μm and the maximum was of approximately 24 μm . The microcapsules with smaller shell thickness are more challenging to produce, as the thinner stream of the middle phase makes them more susceptible to break. The micrographs of Fig. 3.13 clearly show how the shell becomes thicker as the middle phase flow rate is increased. The large-shell thickness microcapsules, produced at high middle phase flow rates are eccentric and the shell thickness is not uniform.

$$\frac{t}{D/2} = 1 - \left[1 + \left(\frac{Q_m}{Q_i} (1 - \alpha) \right) \right]^{-1/3} \quad (3-8)$$



(a)



(b)

Figure 3.12: (a) Shell thickness in units of droplet radius ($t/(D/2)$) as a function of middle and outer phase flow rates (Q_m and Q_o) at a fixed $Q_i = 200 \mu\text{L/h}$ with Design A ($\phi_i = 80 \mu\text{m}$, $\phi_c = 350 \mu\text{m}$ and $l = 120 \mu\text{m}$): $Q_m =$ (■) $25 \mu\text{L/h}$, (●) $50 \mu\text{L/h}$, (▲) $100 \mu\text{L/h}$, (▼) $150 \mu\text{L/h}$, (►) $200 \mu\text{L/h}$, (◄) $250 \mu\text{L/h}$ and (◆) $300 \mu\text{L/h}$ and (b) Shell thickness evaluated by Equation 3-8 (continuous line) as a function of the flow rate ratio Q_m/Q_i : $Q_o =$ (■) $500 \mu\text{L/h}$, (●) $1000 \mu\text{L/h}$, (▲) $1500 \mu\text{L/h}$, (▼) $2000 \mu\text{L/h}$, (►) $2500 \mu\text{L/h}$, (◄) $3000 \mu\text{L/h}$, (◆) $3500 \mu\text{L/h}$, (■) $4000 \mu\text{L/h}$, (●) $4500 \mu\text{L/h}$ and (▲) $5000 \mu\text{L/h}$.

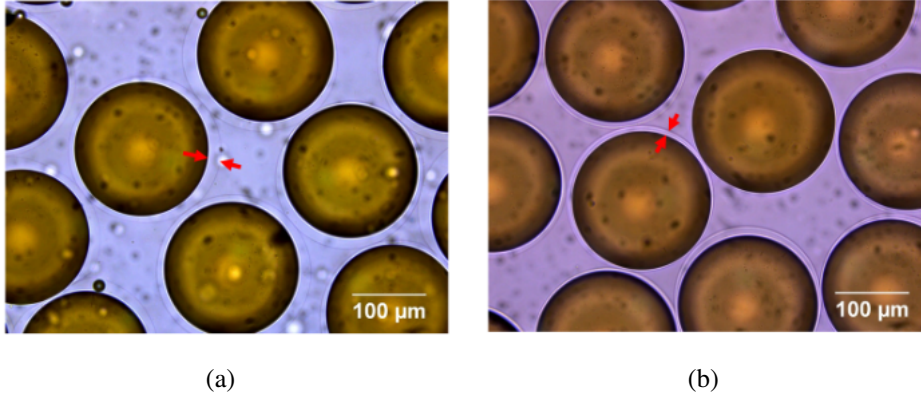


Figure 3.13: Examples of microcapsules with different shell thickness (paired red arrows) produced at different Q_m : (a) $Q_i = 200 \mu\text{L/h}$, $Q_m = 250 \mu\text{L/h}$ and $Q_o = 1500 \mu\text{L/h}$ and (b) $Q_i = 200 \mu\text{L/h}$, $Q_m = 50 \mu\text{L/h}$ and $Q_o = 1500 \mu\text{L/h}$.

(b) At fixed $Q_m = 100 \mu\text{L/h}$

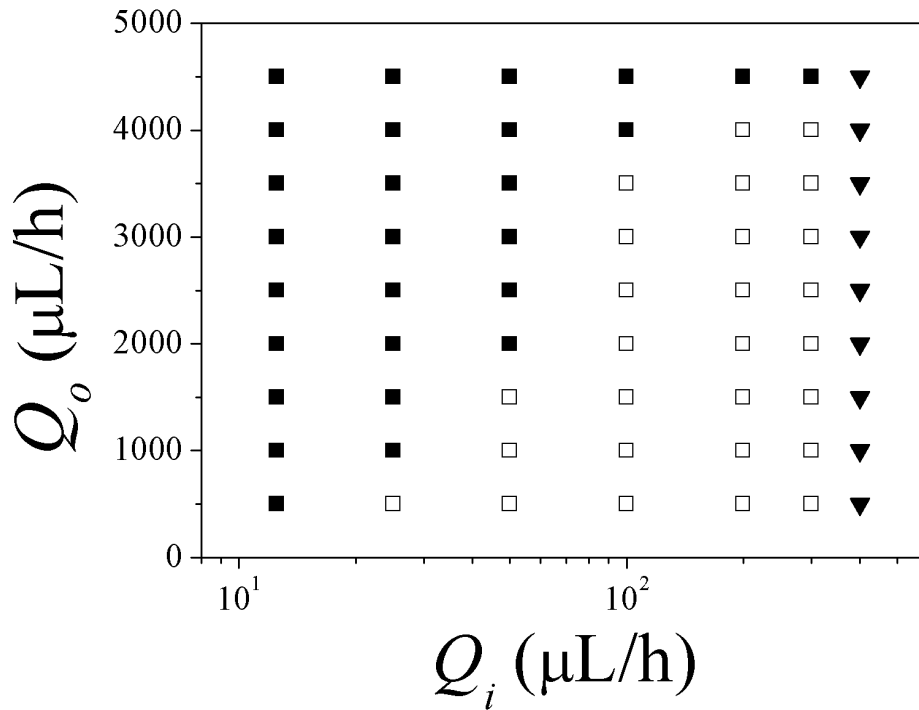
The operability window can be built in a different plane of the parameter space by fixing the middle phase flow rate. Fig. 3.14(a) presents the operability diagram for $Q_m = 100 \mu\text{L/h}$ as a function of the inner and outer phase flow rates. The flow states map as a function of the outer Ca_o and inner Ca_i phase capillary numbers is shown in Fig. 3.14(b).

The inner phase capillary number is defined as:

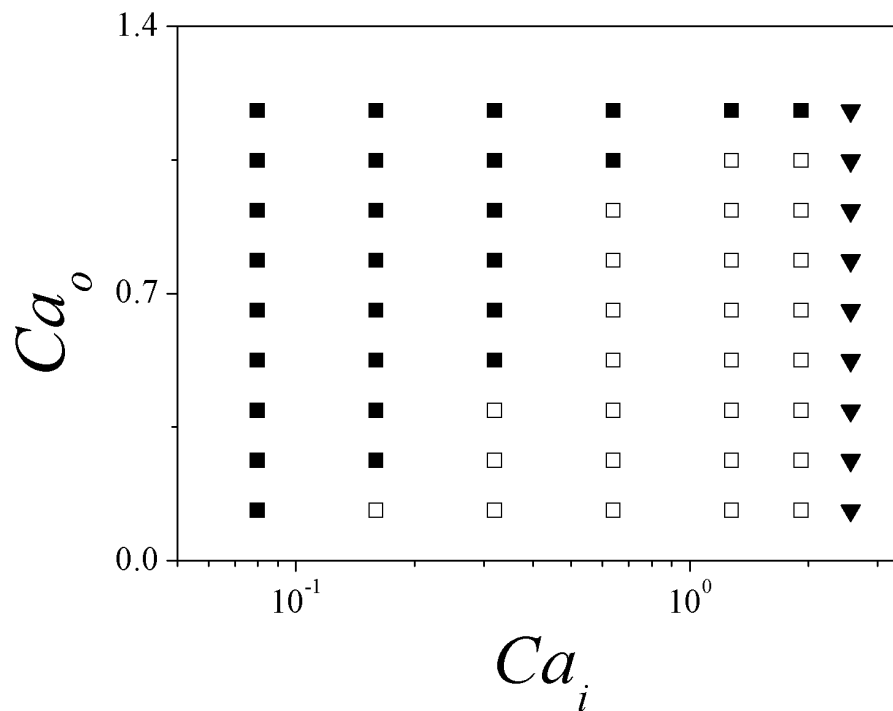
$$Ca_i = \frac{\mu_i Q_i}{\sigma_{mi}(\phi_i^2)} \quad (3-9)$$

Monodispersed O/W/O double emulsion was only produced inside a narrow range of parameters, marked as open symbols in Fig. 3.14. For inner phase capillary number higher than $Ca_i \approx 2$, there is the jetting flow regime and droplet detachment occurs far from the tip of the injection capillary tube, as shown in Fig. 3.9. The jetting regime is marked as filled triangles in the maps and the produced microcapsules were polydisperse [2].

At each value of Q_i (Ca_i) there was a maximum value of the outer phase flow rate Q_o (Ca_o) above which the inner and middle phases flow back into the injection capillary and through the interstices between the square and cylindrical capillaries. These conditions are marked as filled squares in the plots.



(a)

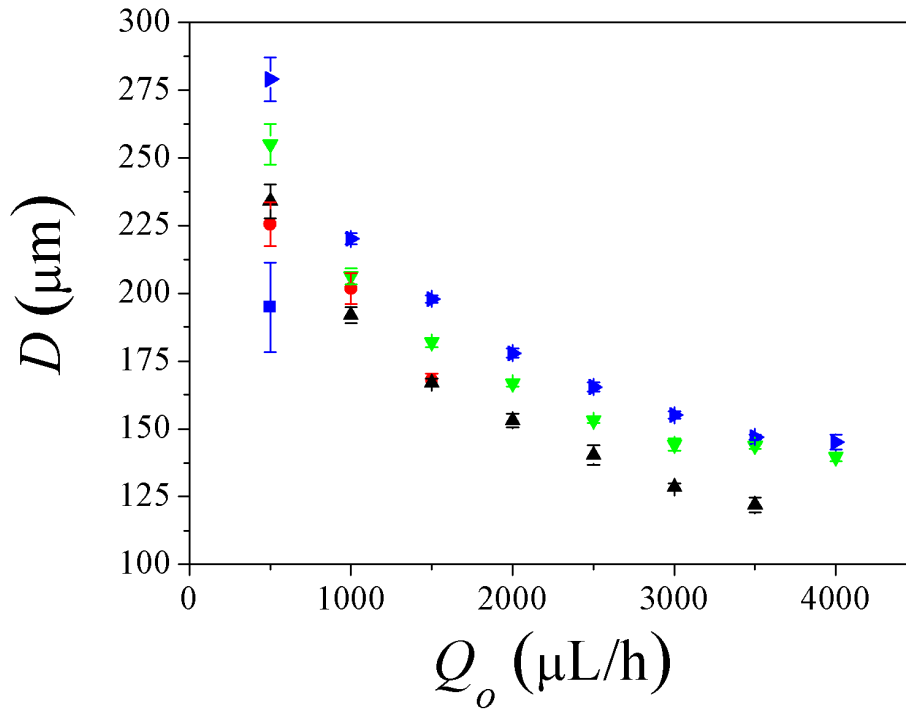


(b)

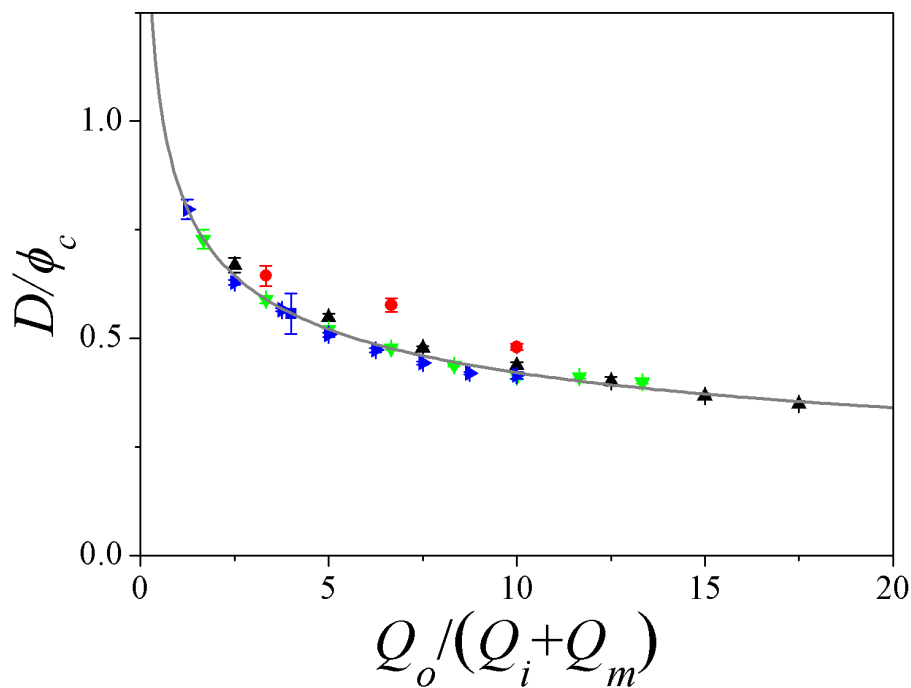
Figure 3.14: (a) Operability window as a function of the flow rates Q_i and Q_o at a fixed middle phase flow rate, $Q_m = 100 \mu\text{L/h}$ using Design A ($\phi_i = 80 \mu\text{m}$, $\phi_c = 350 \mu\text{m}$ and $l = 120 \mu\text{m}$) and (b) Operability window represented as a function of the outer and inner phases capillary numbers: (□) monodispersed O/W/O templates, (▼) jetting regime, formation of polydispersed microcapsules, (■) back flow regime, the outer phase invades the injection channels of the inner and middle phases.

Inside the operability window, the capsule diameter falls as the outer phase flow rate rises, as shown in Fig. 3.15(a). All the data collapses into a single curve when plotted in dimensionless form, as presented in Fig. 3.15(b). The drop diameter in units of the collecting capillary diameter is plotted as a function of $Q_o/(Q_i + Q_m)$. The data is well fitted by the same power-law relation (Eq. 3-7), which is shown as a continuous line in the plot.

The variation of the shell thickness, in units of capsule radius, as a function of the middle and outer phases flow rate is shown in Fig. 3.16. Except for the very low inner phase flow rate ($Q_m/Q_i = 4$), the data is well described by Eq. 3-8 (continuous line) in 3.16(b). The dimensionless shell thickness rises as the inner phase flow rate falls.

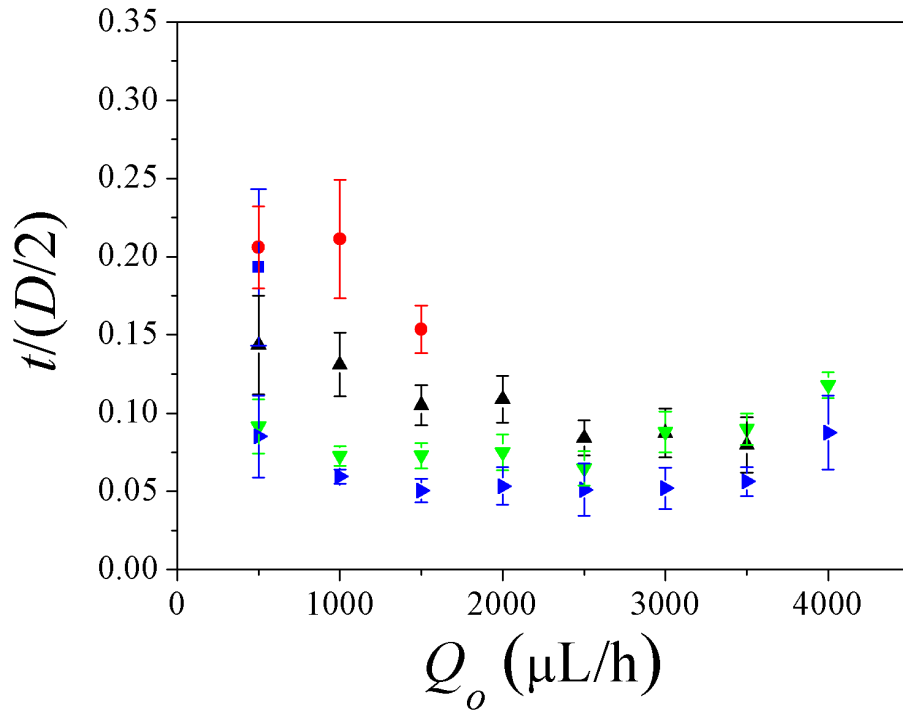


(a)

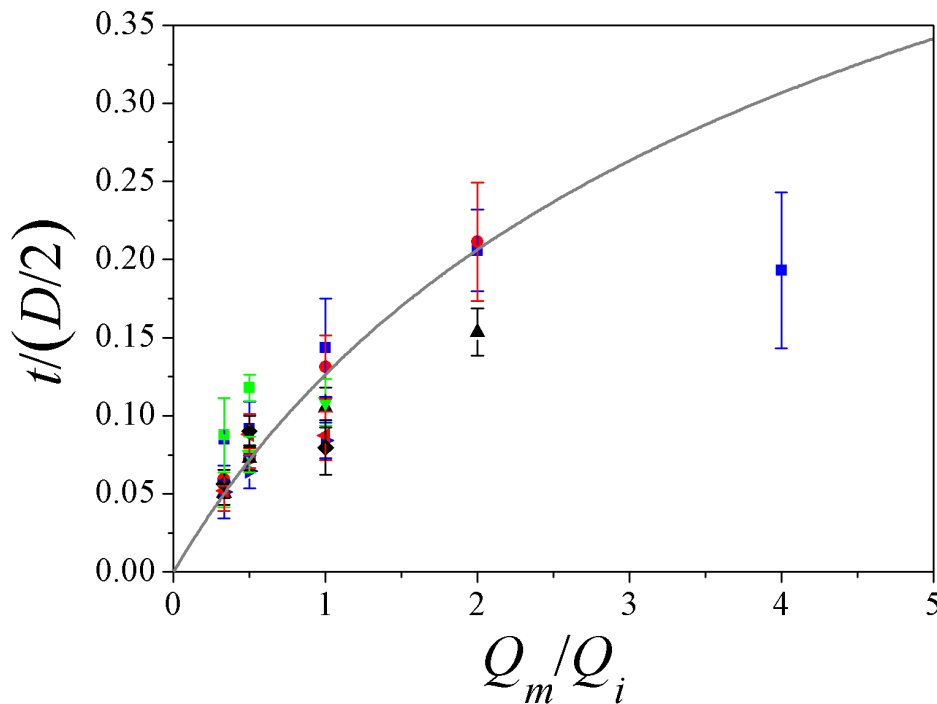


(b)

Figure 3.15: (a) Microcapsule diameter (D) as a function of inner and outer phase flow rates (Q_i and Q_o) at a fixed $Q_m = 100 \mu\text{L/h}$ with Design A ($\phi_i = 80 \mu\text{m}$, $\phi_c = 350 \mu\text{m}$ and $l = 120 \mu\text{m}$) and (b) power-law fit of the diameter in units of the collecting capillary diameter (continuous line) as a function of $Q_o/(Q_i + Q_m)$: $Q_i =$ (■) $25 \mu\text{L/h}$, (●) $50 \mu\text{L/h}$, (▲) $100 \mu\text{L/h}$, (▼) $200 \mu\text{L/h}$, (►) $300 \mu\text{L/h}$.



(a)



(b)

Figure 3.16: (a) Shell thickness in units of droplet radius ($t(D/2)$) as a function of inner and outer phase flow rates (Q_i and Q_o) at a fixed $Q_m = 100 \mu\text{L/h}$ with Design A ($\phi_i = 80 \mu\text{m}$, $\phi_c = 350 \mu\text{m}$ and $l = 120 \mu\text{m}$): $Q_m =$ (■) $25 \mu\text{L/h}$, (●) $50 \mu\text{L/h}$, (▲) $100 \mu\text{L/h}$, (▼) $200 \mu\text{L/h}$, (►) $300 \mu\text{L/h}$ and (b) Shell thickness evaluated by Equation 3-8 (continuous line) as a function of the flow rate ratio Q_m/Q_i : $Q_o =$ (■) $500 \mu\text{L/h}$, (●) $1000 \mu\text{L/h}$, (▲) $1500 \mu\text{L/h}$, (●) $2000 \mu\text{L/h}$, (►) $2500 \mu\text{L/h}$, (◄) $3000 \mu\text{L/h}$, (◆) $3500 \mu\text{L/h}$, (■) $4000 \mu\text{L/h}$.

3.3.2

Microfluidic design B ($\phi_i = 50 \mu\text{m}$, $\phi_c = 250 \mu\text{m}$ and $l = 75 \mu\text{m}$)

In order to study the effect of the device geometry on the microcapsule production process and its dimensions, a device with smaller injection and collection capillary tips (Design B) was used to run some experiments. The injection capillary tip ϕ_i and the distance between the injection and collection capillaries l were reduced by a factor of 0.625. The collection capillary tip was reduced by a factor of 0.7.

Fig. 3.17(a) presents the operability window as a function of middle and outer phase flow rates at a constant inner phase flow rate $Q_i = 100 \mu\text{L/h}$. The dimensionless flow map as a function of the outer and middle phases capillary numbers is shown in Fig. 3.17(b). The range of dimensionless parameters that defines the conditions at which the monodispersed O/W/O double emulsions are produced is wider than the one presented in Fig. 3.8 for Design A, with larger capillary tips. The maximum middle phase capillary number above which the jetting regime starts increased from $Ca_m \approx 0.75$ to $Ca_m \approx 3$, and the maximum outer phase capillary number above which back flow occurs increased from $Ca_o \approx 1.2$ to $Ca_o \approx 2$.

Besides widening the operability window, the capillary device using Design B produced microcapsules with smaller diameters. As shown in Fig. 3.18(a), the diameter of the microcapsules varied from 95 to 200 μm . In contrast, Design A produced microcapsules ranging from 130 to 260 μm . The reduction of the microcapsule diameter range as a function of the characteristic dimensions of the microfluidic device is mainly associated to an increase in the shear rate that pulls the middle and inner phase leading to a faster droplet detachment and consequently a reduction on the microcapsule diameter [21, 91, 132].

As in the previous case, the diameter in units of collecting capillary diameter is represented by a single power-law function (Eq. 3-10) when plotted as a function of $Q_o/(Q_m + Q_i)$, as shown in Fig. 3.18(b). The relation has the same exponent of Eq. 3-7 with a slightly higher coefficient. Data obtained with this microfluidic design is more scattered than data obtained with microfluidic design A due to the small dimensions of design B which are harder to reproduce.

The range of shell thickness in units of microcapsule radius was similar to the values obtained with Design A. The dependence on flow rate is well described by Eq. 3-8, except at very low middle phase flow rate, close to the boundaries of the operability window.

$$\frac{D}{\phi_c} = 1.05 \left(\frac{Q_o}{Q_m + Q_i} \right)^{-0.3} \quad (3-10)$$

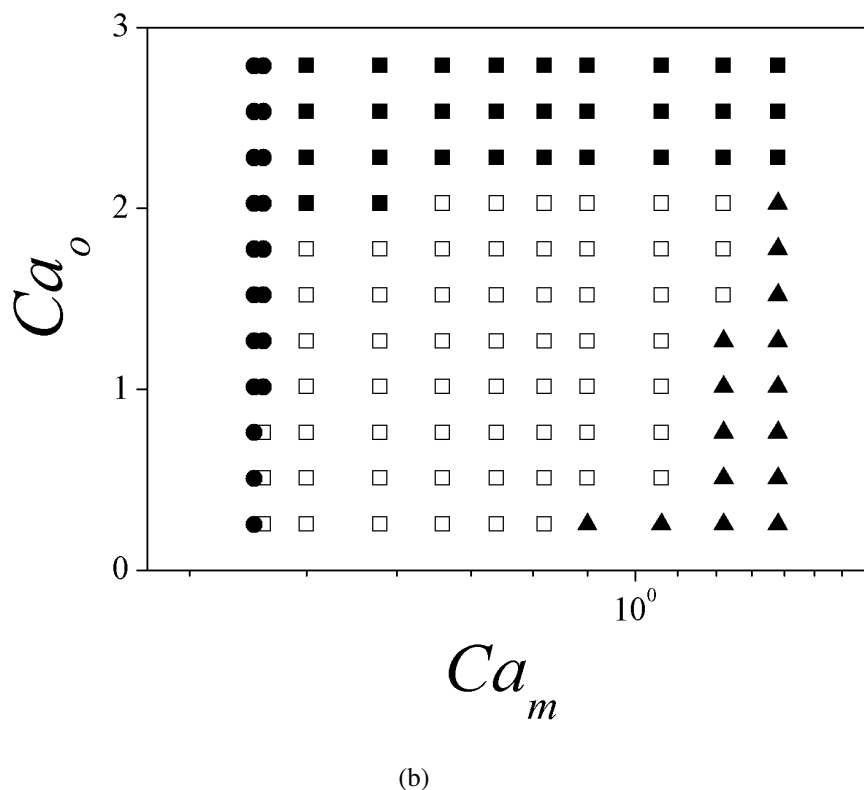
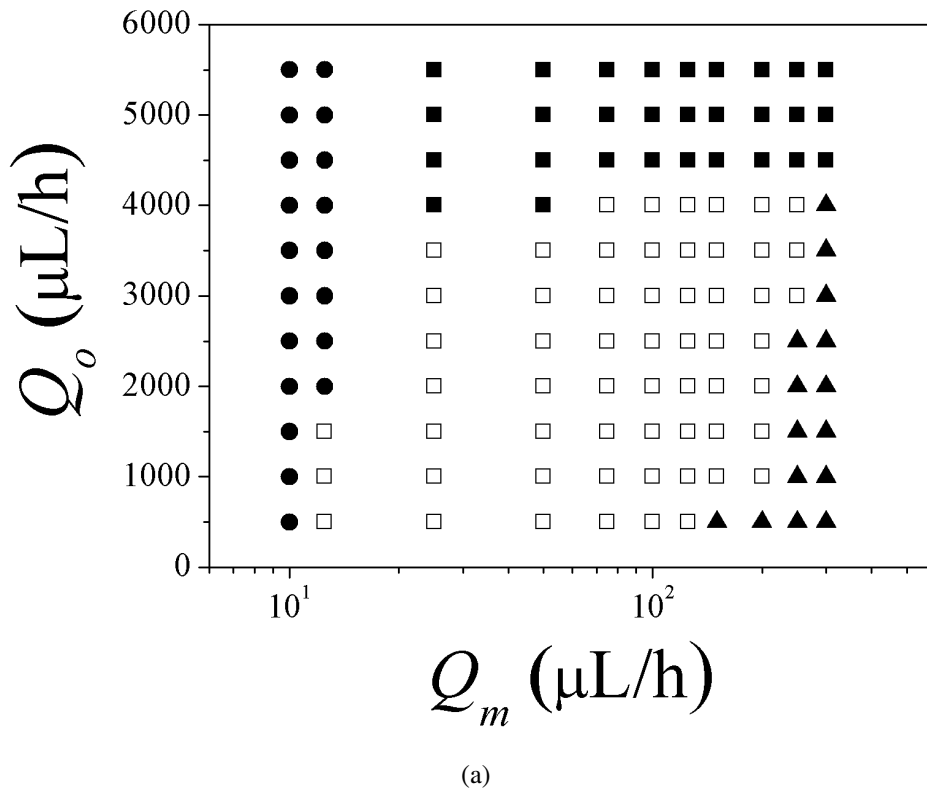


Figure 3.17: (a) Operability window as a function of the flow rates Q_m and Q_o at a fixed inner phase flow rate, $Q_i = 100 \mu\text{L/h}$ using Design B ($\phi_i = 50 \mu\text{m}$, $\phi_c = 250 \mu\text{m}$ and $l = 75 \mu\text{m}$) and (b) Operability window represented as a function of the outer and middle phases capillary numbers: (□) monodispersed O/W/O templates, (▲) jetting regime, formation of double emulsion with multiple inner compartments, (●) formation of droplets containing only the middle phase without the inner core together with the formation of polydispersed microcapsules, (■) back flow regime, the outer phase invades the injection channels of the inner and middle phases.

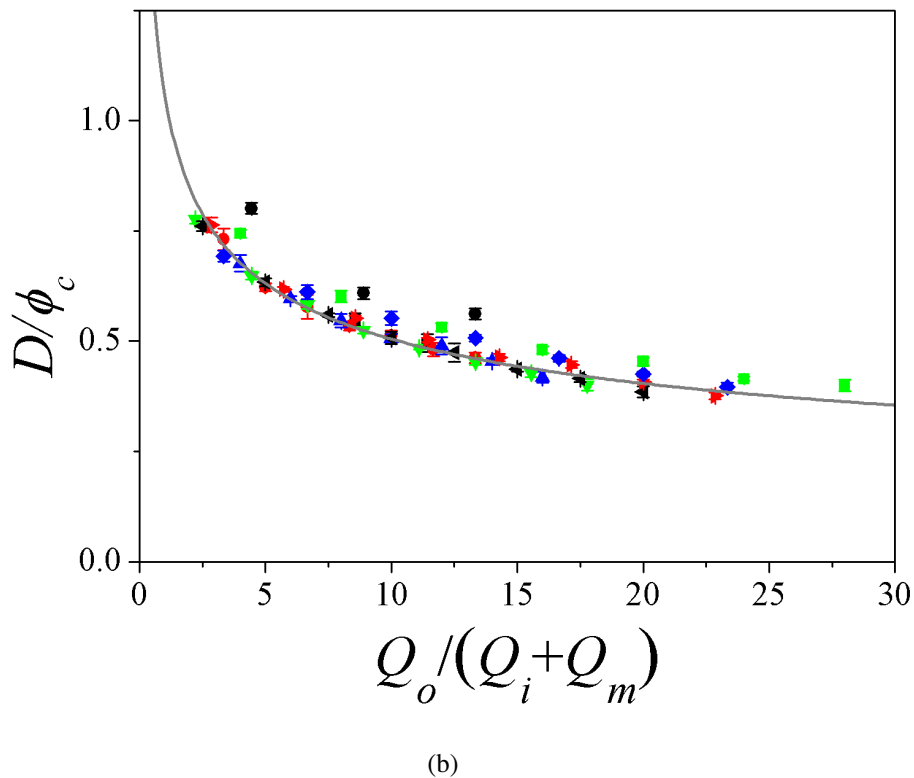
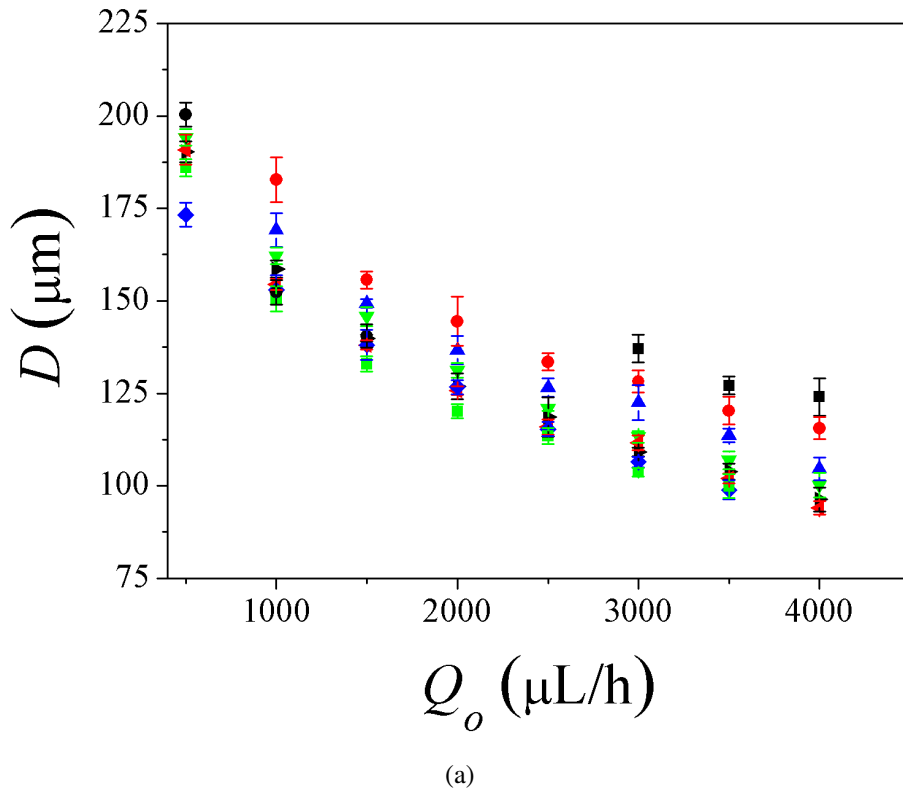
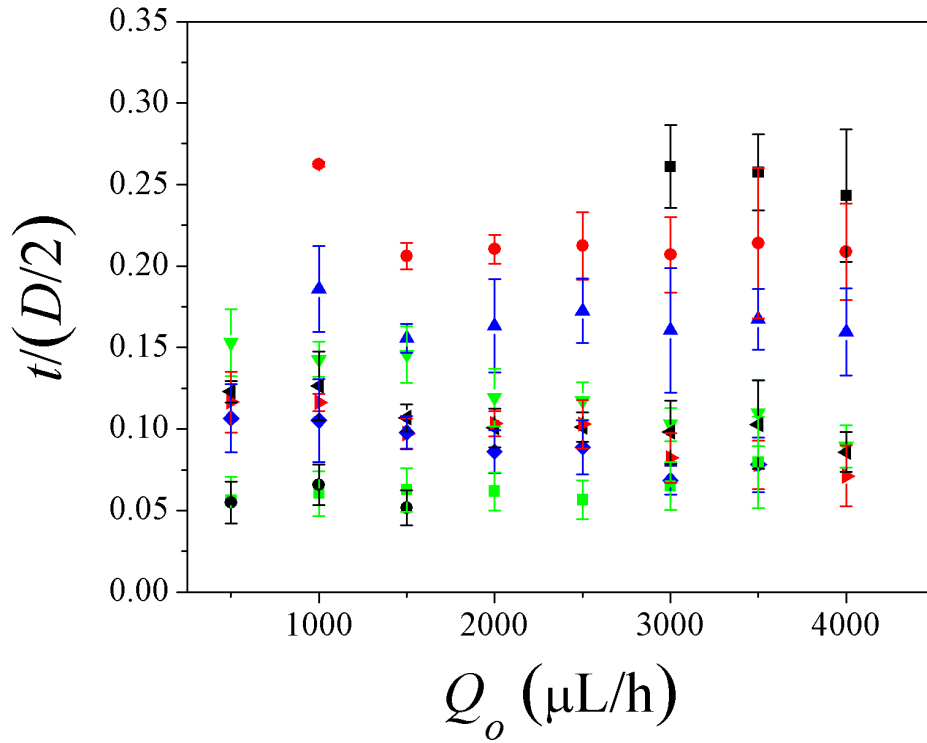
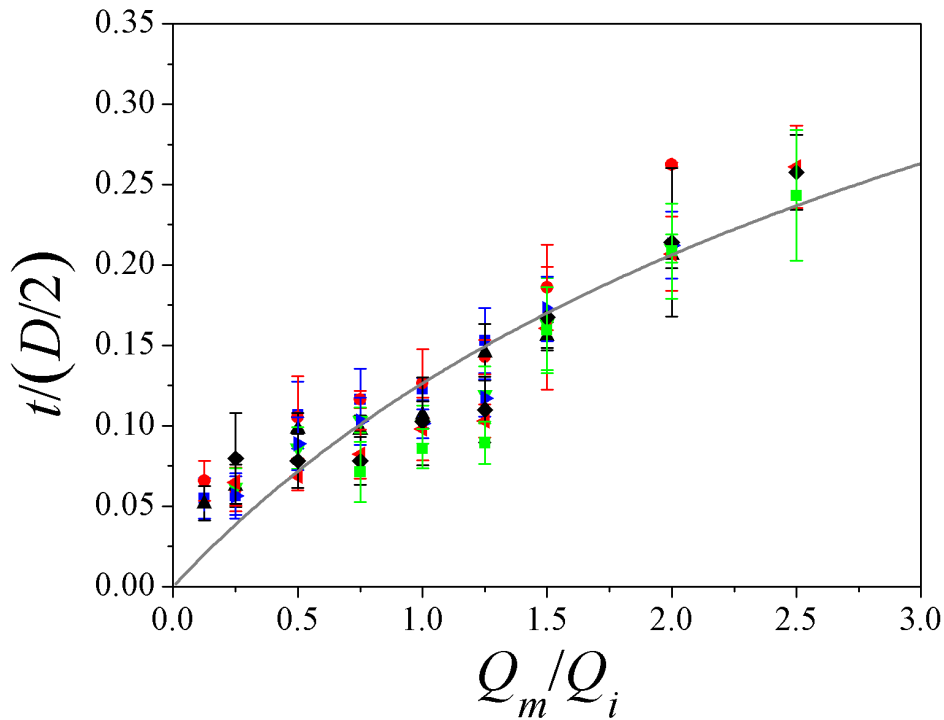


Figure 3.18: (a) Microcapsule diameter (D) as a function of middle and outer phase flow rates (Q_m and Q_o) at a fixed $Q_i = 100 \mu\text{L/h}$ with Design B ($\phi_i = 50 \mu\text{m}$, $\phi_c = 250 \mu\text{m}$ and $l = 75 \mu\text{m}$) and (b) power-law fit of the diameter in units of the collecting capillary diameter (continuous line) as a function of $Q_o/(Q_i + Q_m)$: $Q_m = (\bullet)$ $12.5 \mu\text{L/h}$, (\blacksquare) $25 \mu\text{L/h}$, (\blacklozenge) $50 \mu\text{L/h}$, (\blacktriangleright) $75 \mu\text{L/h}$, (\blacktriangleleft) $100 \mu\text{L/h}$, (\blacktriangledown) $125 \mu\text{L/h}$, (\blacktriangle) $150 \mu\text{L/h}$, (\bullet) $200 \mu\text{L/h}$ and (\blacksquare) $250 \mu\text{L/h}$.



(a)



(b)

Figure 3.19: (a) Shell thickness in units of droplet radius ($t(D/2)$) as a function of middle and outer phase flow rates (Q_m and Q_o) at a fixed $Q_i = 200 \mu\text{L/h}$ with Design A ($\phi_i = 50 \mu\text{m}$, $\phi_c = 250 \mu\text{m}$ and $l = 75 \mu\text{m}$): $Q_m = (\bullet) 12.5 \mu\text{L/h}$, $(\blacksquare) 25 \mu\text{L/h}$, $(\blacklozenge) 50 \mu\text{L/h}$, $(\blacktriangleright) 75 \mu\text{L/h}$, $(\blacktriangleleft) 100 \mu\text{L/h}$, $(\blacktriangledown) 125 \mu\text{L/h}$, $(\blacktriangle) 150 \mu\text{L/h}$, $(\bullet) 200 \mu\text{L/h}$ and $(\blacksquare) 250 \mu\text{L/h}$ and (b) Shell thickness evaluated by Equation 3-8 (continuous line) as a function of the flow rate ratio Q_m/Q_i : $Q_o = (\blacksquare) 500 \mu\text{L/h}$, $(\bullet) 1000 \mu\text{L/h}$, $(\blacktriangle) 1500 \mu\text{L/h}$, $(\blacktriangledown) 2000 \mu\text{L/h}$, $(\blacktriangleright) 2500 \mu\text{L/h}$, $(\blacktriangleleft) 3000 \mu\text{L/h}$, $(\blacklozenge) 3500 \mu\text{L/h}$, $(\blacksquare) 4000 \mu\text{L/h}$.

3.4

Conclusions

Gellan-gum was successfully used as shell material to produce biopolymer-based microcapsules filled with sunflower oil. Two designs of a glass-capillary microfluidic device that combines co-flow and flow focusing were used. Results show that reducing the tip of the capillaries can reduce the capsules diameter. Moreover, the flow rate of the continuous phase is the main parameter that affects the size of the capsules. The shell thickness, in turn, is tuned by fixing the flow rate of the inner phase and varying the flow of the middle phase.

The recovery process carried out enabled to disperse the microcapsules in aqueous media, what broadens their potential applications.

4

Flow of microcapsules through constricted capillary

4.1

Introduction

As discussed in Chapter 2, microcapsules have a broad range of applications, including in food [1, 37, 133], cosmetic [61, 134], pharmaceutical industries [135, 136] and reservoir engineering [137, 138, 139]. In most of these applications, microcapsules are used to transport a desired chemical component, avoiding interaction with the environment, to a specific region where it should be released at a specific time. Microcapsules can also be used as a means to control the mobility of a water phase injected in a reservoir, partially blocking the pore throats and diverting water to oil-filled regions.

In many applications, microcapsules flow through confined geometries, which are present in physiological systems and porous media, making the dynamics of deformable microcapsules in confined flows relevant to the success of target chemical delivery by a microcapsule suspension. In some cases, it is important to design microcapsules that can sustain the stress and deformation that they are subjected to as they flow through constricted channels, such that the encapsulated chemical can reach the target region. On the other hand, there are situations in which the content release is triggered by an external stress, which can be achieved during the flow through a constriction [10].

Microcapsule is widely considered a good model to describe the hydrodynamic behavior of cells [140], and the flow of suspended microcapsules through confined channels has attracted much attention also because of the development of microfluidic medical diagnostic devices based on cell deformation as they flow through constricted capillaries [141, 142]. Healthy and diseased cells have different stiffness and the dynamics of deformation can be used to separate normal and cancer cells, for example [143].

Flow of suspended microcapsules through confined channels poses a challenging problem due to its complex fluid-solid interaction. A myriad of experimental and numerical studies has been developed to understand the underlying physical phenomena and were discussed in a recent review [144].

The flow of suspended capsules through confined geometry has been exten-

sively studied by numerical simulation. Leyrat-Maurin and Barthès-Biesel [145] presented a model for the flow of a capsule through an axisymmetric hyperbolic constriction, considering both a constant flow rate and constant pressure-drop condition to infer properties of the capsules from filtration experiments. Details of the capsule deformation and extra pressure-drop as the capsule flows through the constriction were determined as a function of capsule properties and flow conditions. The three-dimensional flow of an elastic capsule through constricted channels has been studied to relate the capsule deformation and extra pressure with the membrane elastic properties and flow conditions [146, 147]. From their computational predictions, Dimitrakopoulos and Kuriakose [147] proposed a method based on the flow in a converging micro capillary to evaluate the membrane shear modulus independently of its dilation modulus.

Experimental analysis of microscale flow of suspended microcapsules is challenging. Risso et al. [148] experimentally studied motion and deformation of bioartificial capsules in a 4 mm diameter capillary. They show that the steady-state capsule configuration was a function of the capillary number, defined as the ratio of viscous to elastic forces, and the capsule diameter to tube radius ratio. The capsule deformation in the flow through microchannels of comparable dimensions was also used by Lefebvre et al. [149] to characterize the membrane mechanical properties of microcapsules. The transient flow of ovalbumin microcapsules through convergent-divergent square microchannels, with cross section area varying from $30 \times 30 \mu\text{m}^2$ to $70 \times 70 \mu\text{m}^2$, was studied by Leclerc et al. [150]. The relaxation process of the capsule back to its nearly undeformed configuration as it flows out of the constricted channel was used to extract the shear modulus of the membrane. Flow through a convergent channel was also used to evaluate elastic properties of cells enabling cell sorting and cancer diagnostics [151]. Most of the experimental analyses are focused on the determination of the capsule membrane properties and do not report the extra pressure associated with the flow of the capsule through a constriction, which would be an important parameter to validate available numerical predictions. The effect of shell stiffness and thickness of PDMS capsules on the pressure difference of the flow through constricted capillary was studied by do Nascimento et al. [64]. PDMS capsules are strong enough that capsule burst was not observed in any condition. As discussed in the review by Barthès-Biesel [144], there are very few observations of flow induced capsule burst; the capsules used in the experiments have been too resistant or the flow strength too weak to rupture the capsule membrane.

This chapter reports the evolution of the deformation and pressure difference in the flow of a suspended microcapsule through a constricted microcapillary in a constant flow rate condition. Gellan gum microcapsules of different diameter and shell thickness, produced as described in the previous chapter, were used in the

experiments. We discuss the effect of capsule size and shell thickness on the flow mobility and shell rupture.

4.2

Experimental set-up and methodology

A constricted glass capillary with a channel to constriction diameter ratio of $D_0/D_c = 300/100 \mu\text{m}$ made by Hilgenberg (Germany) was used in the experiments. It is a smooth geometry with a total length of 80 mm. Its constriction is in the middle of this length and has length of $L_c = 4 \text{ mm}$. The capillary was treated with a polyelectrolytes solution composed of 1 wt% poly(acrylamide-co-diallyldimethyl-ammonium chloride) (Sigma-Aldrich, USA) and 2 mol/L NaCl to render a hydrophilic surface and then it was fixed on a microscope slide with Epoxy resin (Devcon Corp., USA).

As shown in Fig. 4.1, besides the constricted capillary, the experimental apparatus consisted of a Fluigent system composed of a stand-alone pressure pump (LineUp Flow EZ series - 0 to 2000 mbar) combined with a flow rate control unit (Flow Unit S) to feed the suspension through the capillary at constant flow rates and measure the pressure drop and a Link module (LineUp) that connects the chain to a PC for software control; a computer to record the pressure data; a 15mL Falcon with an air-tight connector P-CAP from Fluigent; and an inverted microscope (model DMi8, Leica Microsystem, Germany) equipped with a high speed camera (model Fastcam SA-3, Photron, USA) to record real time images of microcapsules flow; a second computer to monitor the flow at real time and a dispensing beaker.

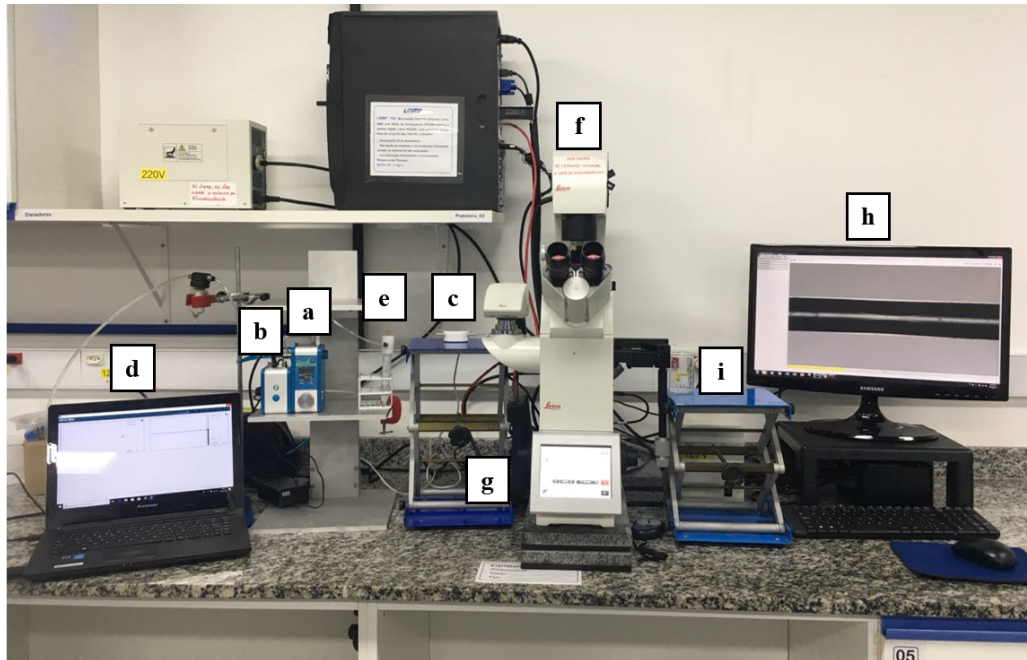


Figure 4.1: Experimental set-up for flowing microcapsules through constriction capillaries, including: (a) a stand-alone pressure pump; (b) a Link module for PC communication; (c) a flow rate control unit; (d) a computer for pressure data recording; (e) a 15mL Falcon with an air-tight connector P-CAP; (f) an inverted microscope; (g) a high speed camera; (h) a computer for real time visualization and (i) a dispensing beaker.

The Fluigent system mounted as described enables the control of the flow rate as well as of the dispense volume once the applied pressure automatically adjusts in the background to maintain the flow rate.

A simplified scheme of the entire set-up is presented in Fig.4.2.

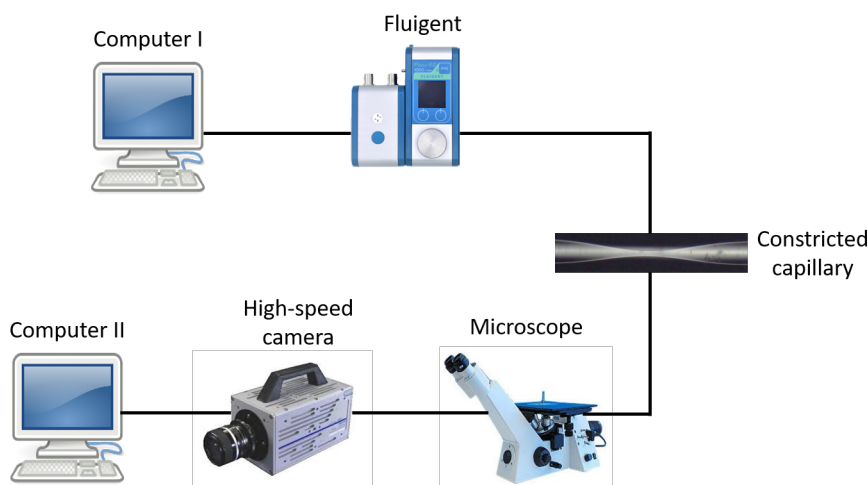


Figure 4.2: Scheme of the experimental set-up for flowing microcapsules through constriction capillaries.

Some batches of microcapsules with different physical characteristics were selected to be used in these experiments and their main properties are shown in Table 4.1. The diameters and shell thicknesses presented are the mean value of 10 measurements made for each batch with their standard deviation. All capsules were smaller than the capillary diameter (D_0) and larger than the constriction diameter (D_c) through which they flowed.

| System ID | D (μm) | t (μm) |
|-----------|-----------------------|-----------------------|
| #1 | 174.6 ± 4.6 | 15.0 ± 2.1 |
| #2 | 143.8 ± 4.2 | 6.3 ± 1.5 |
| #3 | 144.4 ± 6.7 | 15.2 ± 3.7 |
| #4 | 124.4 ± 1.7 | 5.6 ± 1.0 |
| #5 | 109.1 ± 2.9 | 5.3 ± 1.1 |

Table 4.1: Main properties of the microcapsules used in the constriction experiments.

During these experiments, all microcapsules were suspended in a saturated sucrose solution to increase the carrier fluid viscosity, which was fixed at $\mu_0 = 11.5$ MPa.s enabling pressure-drop measurements. A carbopol solution was considered to produce this increase based on Cobos et al. [152] work but its alkaline pH destroys the gellan microcapsules, hindering its use.

Preliminary tests indicated that, with this system, an injection flow rate of at least $Q = 0.2$ mL/h was necessary to accurately measure the pressure-drop evolution. This corresponds to an average velocity in the straight portion of the capillary of $\bar{V} = 4Q/\pi D_0^4 \approx 800$ $\mu\text{m/s}$. Therefore, the following results were all obtained at this flow rate/velocity.

After the tests, all images extracted from the videos were processed with a Matlab code based on frame difference to detect the moving capsules. The images were converted into grayscale and, after denoising, into binary images. Then, morphological operations were performed and small unwanted objects were removed from the background.

The length scale was determined from the known constriction diameter (D_c). The position of the tip of the microcapsules in the flow direction (x) and their length in the flow direction (L_x) were measured in each frame. The velocity of the capsules was calculated from the distance covered over a set of frames and its corresponding time.

4.3

Results and discussion

The dimensionless parameters that govern the flow of a suspended capsule through a constricted capillary are [145]:

- Dimensionless capsule diameter: $\bar{a} = \frac{D}{D_c}$,
- Capillary constriction ratio: $\beta = \frac{D_c}{D_0}$,
- Surface capillary number: $Ca_s = \frac{\mu_0 \bar{V}}{Gt}$,
- Reynolds number: $Re = \frac{\rho \bar{V} D_0}{\mu_0}$ and
- Viscosity ratio: $\lambda = \frac{\mu_i}{\mu_0}$,

where D is the capsule diameter, t is the shell thickness, D_0 and D_c are the capillary and constriction diameter; \bar{V} is the average flow velocity; G is the shear modulus of the shell material; and μ_i and μ_0 are the viscosity of the inner and outer phases. The shear modulus of the shell material $G = 10$ kPa was determined using a cantilevered-capillary force apparatus [153].

In the present analysis, the capillary geometry, Reynolds number and viscosity ratio were fixed at $\beta = 0.33$, $Re = 0.021$ and $\lambda = 4.81$, respectively. The dimensionless capsule diameter \bar{a} and the surface capillary number Ca_s were varied by changing the capsule diameter and shell thickness.

The surface capillary number represents the ratio of viscous to elastic forces. High surface capillary number indicates that viscous force, which deforms the capsule, is larger than the resisting membrane elastic force and leads to highly deformed capsules.

Figure 4.3 presents snapshots of the flow as a capsule passes through the constriction for System #3, with $D = 144.4 \mu\text{m}$ and $t = 15.2 \mu\text{m}$, which corresponds to $\bar{a} = 1.44$ and $Ca_s = 5.9 \times 10^{-4}$. As shown in the figure, the capsule does not burst under these conditions. It partially blocks the flow, causing an increase in the inlet pressure, as displayed in Fig. 4.4. When the capsule is far from the capillary throat, the inlet pressure is close to the one necessary to drive the continuous phase alone, e.g. approximately 5.4×10^{-3} MPa. The inlet pressure grows in order to force the microcapsule deformation, reaches a maximum value of approximately 35.8×10^{-3} MPa and then abruptly falls as the microcapsule flows away from the constriction. When the capsule is far downstream from the throat, the inlet pressure reaches the steady state associated with the flow of the continuous phase alone.

Experiments were repeated for at least 5 different capsules of each system. The behavior for each capsule of a same system was the same. For capsules of System #3, the standard deviation of the pressure peak as the capsule flows through the constriction was close to 11%.

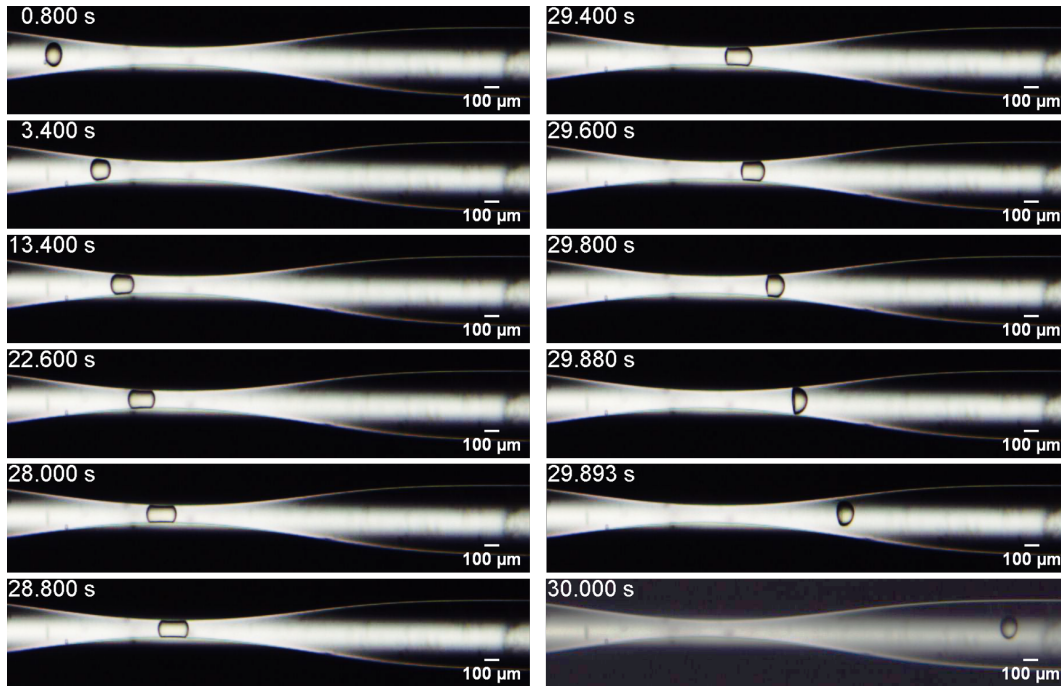


Figure 4.3: Evolution of the microcapsule position and configuration as it flows through the constriction. System #3, $D = 144.4 \mu\text{m}$ and $t = 15.2 \mu\text{m}$ ($\bar{a} = 1.44$ and $Ca_s = 5.9 \times 10^{-4}$).

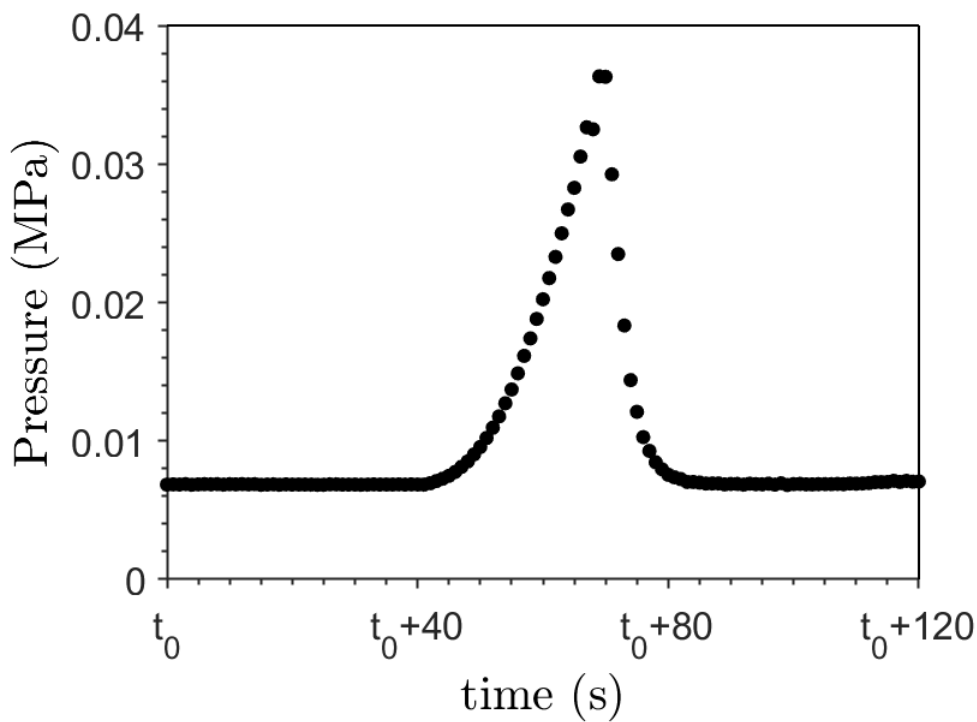


Figure 4.4: Evolution of the inlet pressure as the capsule flows through the constriction. System #3, $D = 144.4 \mu\text{m}$ and $t = 15.2 \mu\text{m}$ ($\bar{a} = 1.44$ and $Ca_s = 5.9 \times 10^{-4}$).

Figure 4.5 presents snapshots of the flow of a capsule from System #5, $D = 109.1 \mu\text{m}$ and $t = 5.3 \mu\text{m}$, which corresponds to $\bar{a} = 1.09$ and $Ca_s = 1.7 \times 10^{-3}$. At these conditions, the capsule also does not burst as it passes through the constriction. Microcapsules from this system are smaller than the ones from System #3 (example shown in Fig. 4.3) and thereby pass more easily and faster through the capillary throat. The extra pressure associated with the flow of the capsule through the constriction could not be measured because it was below the transducer resolution (2.07×10^{-3} MPa).

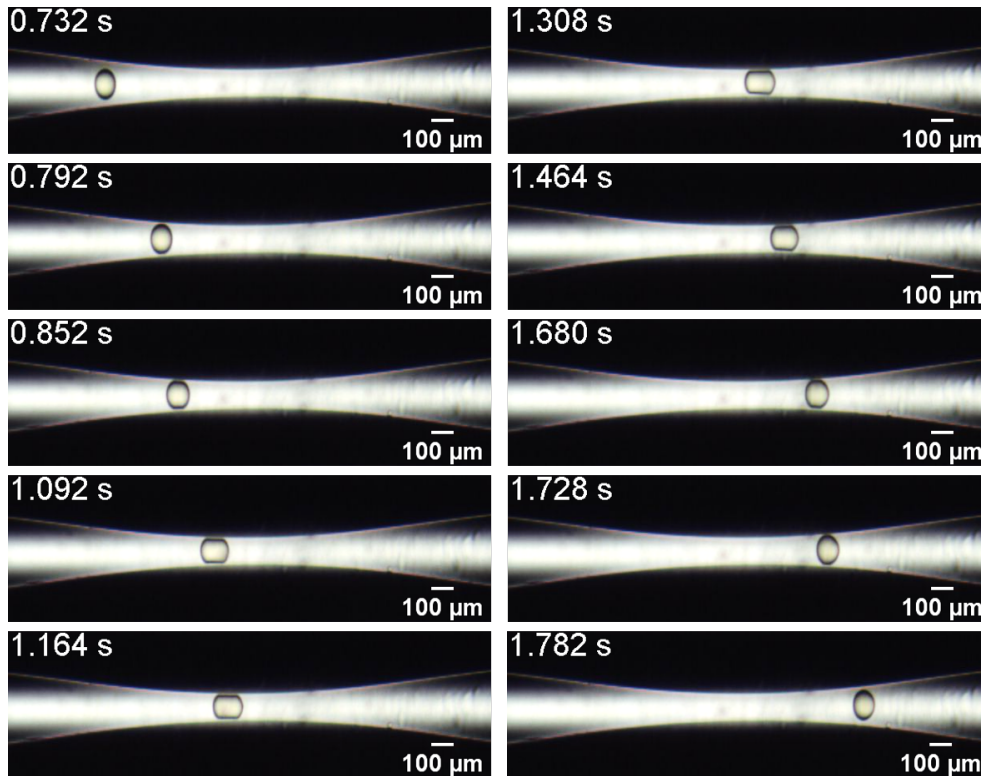


Figure 4.5: Evolution of the microcapsule position and configuration as it flows through the constriction. System #5, $D = 109.1 \mu\text{m}$ and $t = 5.3 \mu\text{m}$ ($\bar{a} = 1.09$ and $Ca_s = 1.7 \times 10^{-3}$).

The evolution of the capsule tip position in the flow direction x for capsules from System #3 and #5 is shown in Fig. 4.6. Far upstream of the minimum diameter position ($x = 0$), capsules from both systems present the same position evolution, since the imposed flow rate is fixed for all experiments. For capsules from System #3, which have larger diameter, the velocity is drastically reduced as it deforms to flow through the constriction. The capsule slows down approximately $500 \mu\text{m}$ upstream of the minimum diameter plane ($x = 0$). It stays near the constriction during approximately 26 s, with an average speed close to $14 \mu\text{m/s}$. During this period, the inlet pressure grows, as shown in Fig. 4.4. On the other hand, as the capsule from System #5 deforms and flows through the constriction, its velocity is

reduced. Then, the microcapsule is quickly expelled from the constriction and flows away from it.

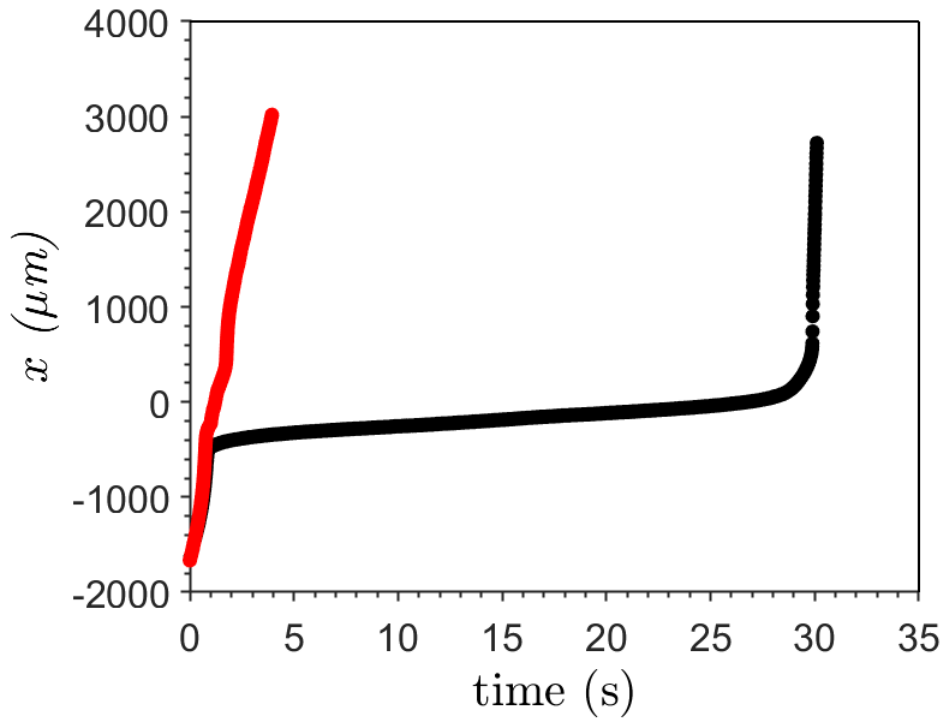


Figure 4.6: Microcapsule position in the flow direction as it flows through the constriction for capsules from (●) System #3 ($\bar{a} = 1.44$ and $Ca_s = 5.9 \times 10^{-4}$) and (●) System #5 ($\bar{a} = 1.09$ and $Ca_s = 1.7 \times 10^{-3}$).

As the capsules diameters are larger than the throat diameter, the capsules deform as they flow through the constriction. The length variation of the capsules in the flow direction L_x is presented in Fig. 4.7. At the straight portion upstream and downstream of the minimum diameter plane, L_x is more or less constant and equal to $L_x \approx 130 \mu\text{m}$ and $L_x \approx 105 \mu\text{m}$ for System #3 and System #5, respectively. These values are smaller than the capsules diameters because of the optical distortion associated with the curved surface of the capillary, since the refractive index of the suspended liquid (sucrose solution) does not match the refractive index of the curved capillary glass wall. As the capsules approach the throat, L_x rises to a maximum value. Because the capsule from System #5 is smaller than the one from System #3, it starts elongating at a position closer to the middle of the constriction and achieves a lower maximum length in the flow direction ($L_{x,0} \approx 155 \mu\text{m}$).

The deformation maybe quantified by the ratio of the length of the capsule at a given instant of time to the length of the undeformed capsule, away from the constriction, e.g. $\varepsilon_x = L_x/L_{x,0}$. Figure 4.8 presents the evolution of the deformation ε_x for capsules from System #3 and #5. Away from the constricted region of the

capillary, $\varepsilon_x \approx 1$, as expected. As the capsule approaches the throat, ε_x rises to a maximum value of approximately $\varepsilon_x \approx 1.71$ for System #3 and $\varepsilon_x \approx 1.42$ for System #5. Downstream of the throat, the larger capsules (from System #3) presented a backend with a concave configuration, leading to values of $\varepsilon_x < 1$, which has been observed in some numerical analyses [145, 146], before relaxing back to its nearly undeformed state.

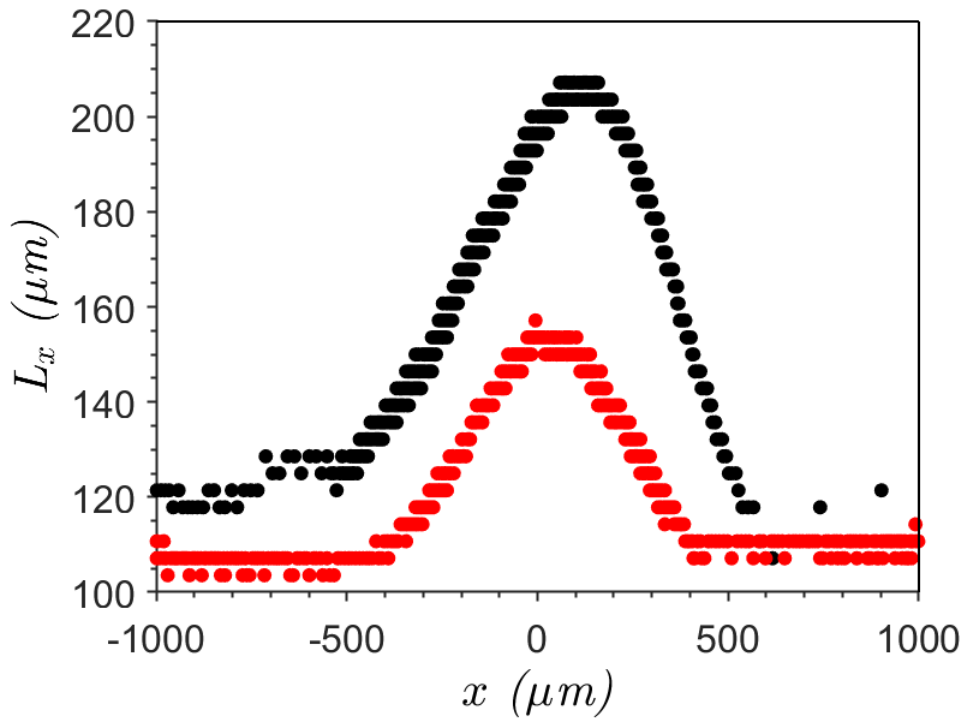


Figure 4.7: Length of the microcapsule in the flow direction as it flows through the constriction for capsules from (●) System #3 ($\bar{a} = 1.44$ and $Ca_s = 5.9 \times 10^{-4}$) and (●) System #5 ($\bar{a} = 1.09$ and $Ca_s = 1.7 \times 10^{-3}$).

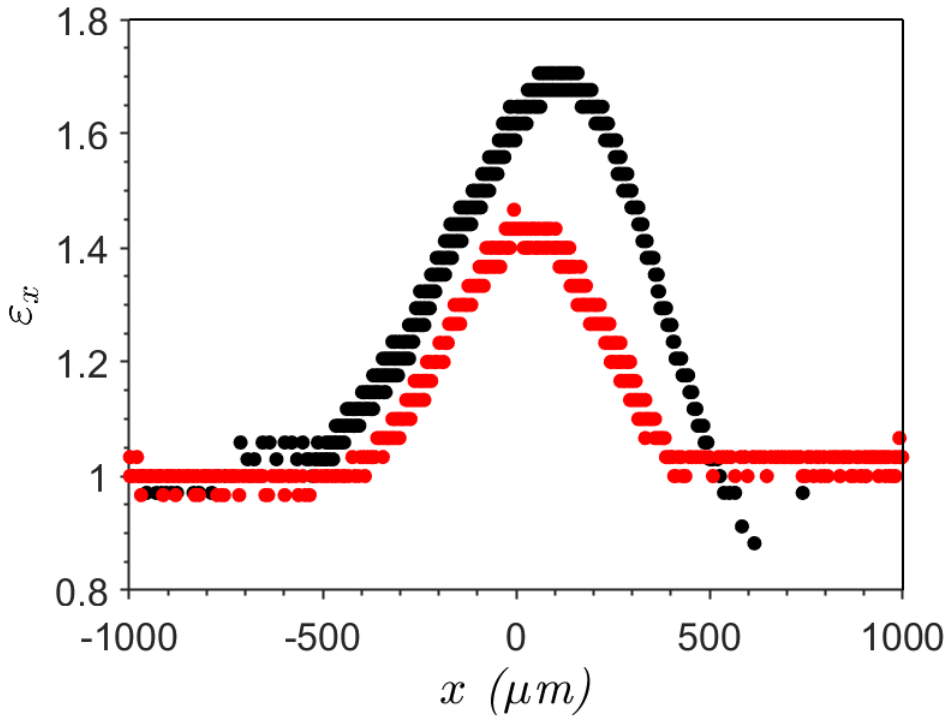


Figure 4.8: Microcapsule deformation $\varepsilon_x = L_x/L_{x,0}$ as it flows through the constriction for capsules from (●) System #3 ($\bar{a} = 1.44$ and $Ca_s = 5.9 \times 10^{-4}$) and (●) System #5 ($\bar{a} = 1.09$ and $Ca_s = 1.7 \times 10^{-3}$).

At some conditions, the stress / deformation is too high and the capsule bursts, releasing its inner content. Figure 4.9 presents snapshots of the flow of a capsule from System #1, $D = 174.6 \mu\text{m}$ and $t = 15.0 \mu\text{m}$ ($\bar{a} = 1.75$ and $Ca_s = 6.0 \times 10^{-4}$), which is one of the systems that releases its inner phase as it passes through the capillary throat. The stress acting on the capsule shell is maximum near the tip and backend of the capsule when it is close to the minimum diameter place [154]. If the shell cannot sustain the imposed stress, it ruptures and the inner phase flows out of the capsule. In the case shown in Fig. 4.9, the inner content is released from the tip of the capsule, as it is clear in frame 104.290 s. In the last frame shown, e.g. 104.430 s, the polymeric shell (almost fully emptied) and the dyed inner phase can be clearly observed. All capsules from System #1 presented the same behavior: they burst as the flowed through the constriction.

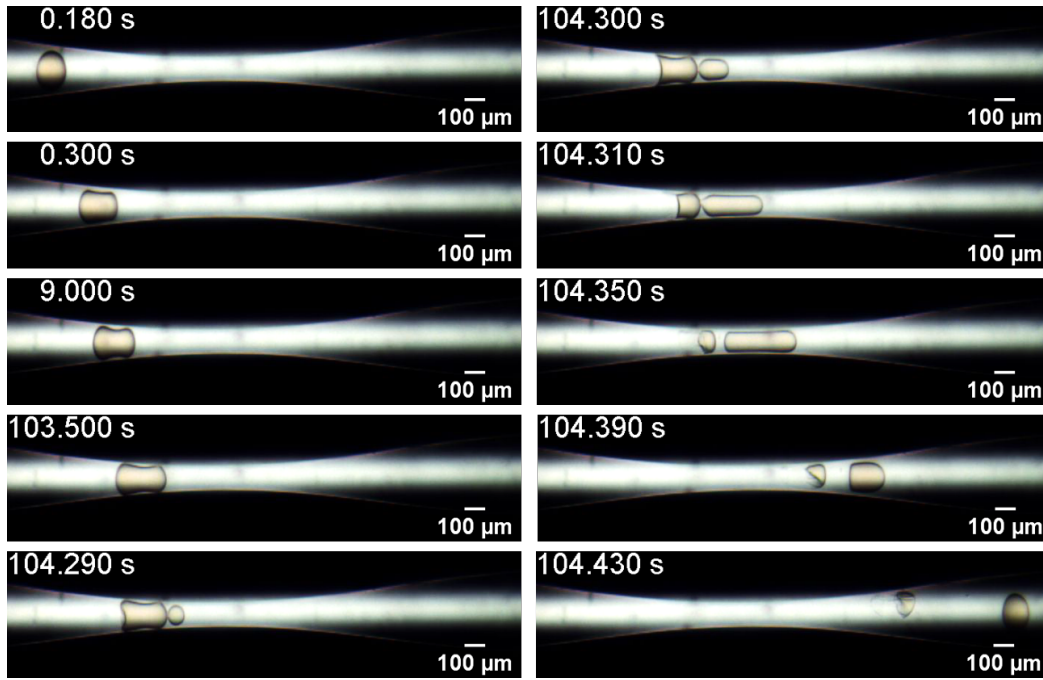


Figure 4.9: Evolution of the microcapsule position and configuration as it flows through the constriction. System #1, $D = 174.6 \mu\text{m}$ and $t = 15.0 \mu\text{m}$ ($\bar{a} = 1.75$ and $Ca_s = 6.0 \times 10^{-4}$).

Figure 4.10 presents the evolution of the inlet pressure for the flow shown in Fig. 4.9. The behavior is similar to the case at which the capsule did not rupture, presented in Fig. 4.4. The pressure rises as the capsule is deformed to flow through the capillary throat. Once the shell ruptures, flow resistance is decreased and the inlet pressure falls. It is important to note that the inlet pressure would be higher if the capsule shell have not ruptured.

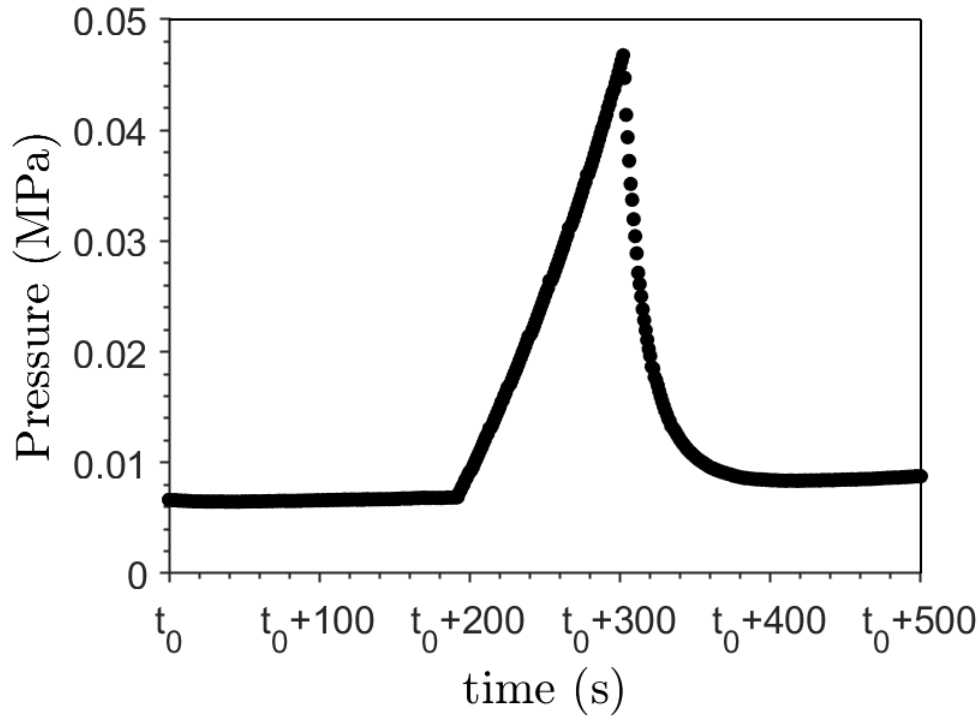
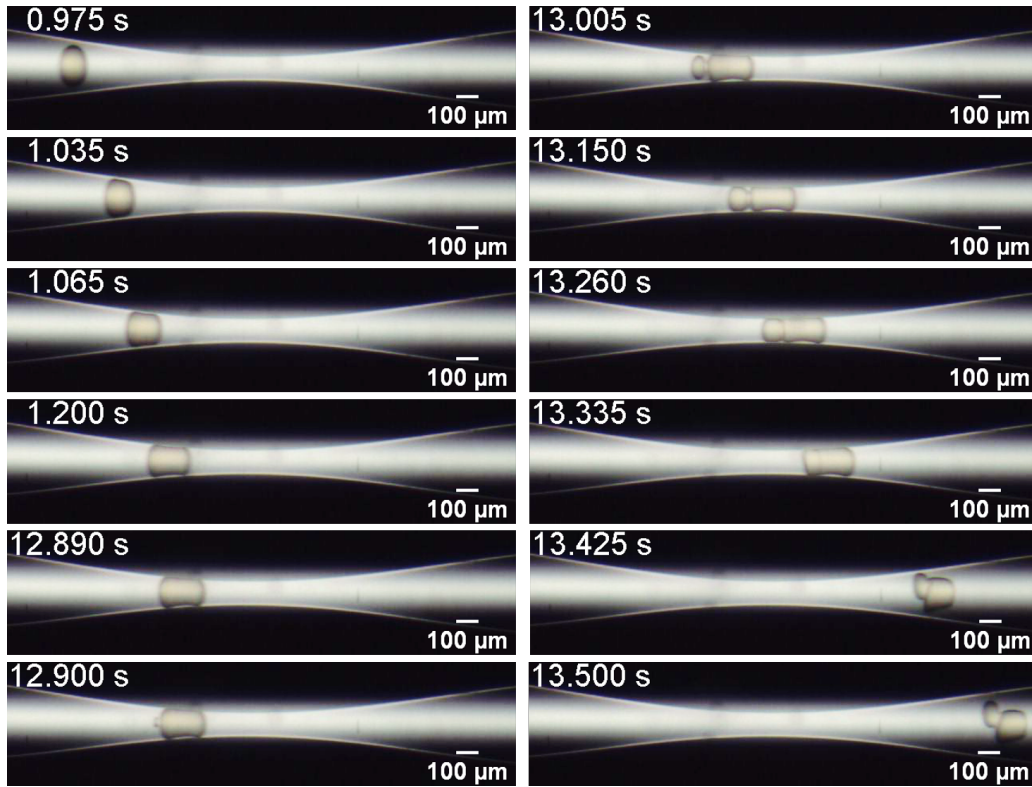


Figure 4.10: Evolution of the inlet pressure as the capsule flows through the constriction. System #1, $D = 174.6 \mu\text{m}$ and $t = 15.0 \mu\text{m}$ ($\bar{a} = 1.75$ and $Ca_s = 6.0 \times 10^{-4}$).

The capsule rupture and consequent inner phase release mechanism was similar for all the systems that were not strong enough to resist to the imposed stress as the capsule flows through the constriction. Figure 4.11 shows snapshots of the flow of a capsule from System #2, $D = 143.8 \mu\text{m}$ and $t = 6.3 \mu\text{m}$ ($\bar{a} = 1.44$ and $Ca_s = 1.4 \times 10^{-3}$) that releases its inner phase from its backend as it passes through the capillary throat, as can be seen in frame 12.900s. Figure 4.12, in turn, presents snapshots of the flow of a capsule from System #4, $D = 124.4 \mu\text{m}$ and $t = 5.6 \mu\text{m}$ ($\bar{a} = 1.24$ and $Ca_s = 1.6 \times 10^{-3}$), which is another system that releases its inner phase from the tip of the capsule as it passes through the capillary throat.



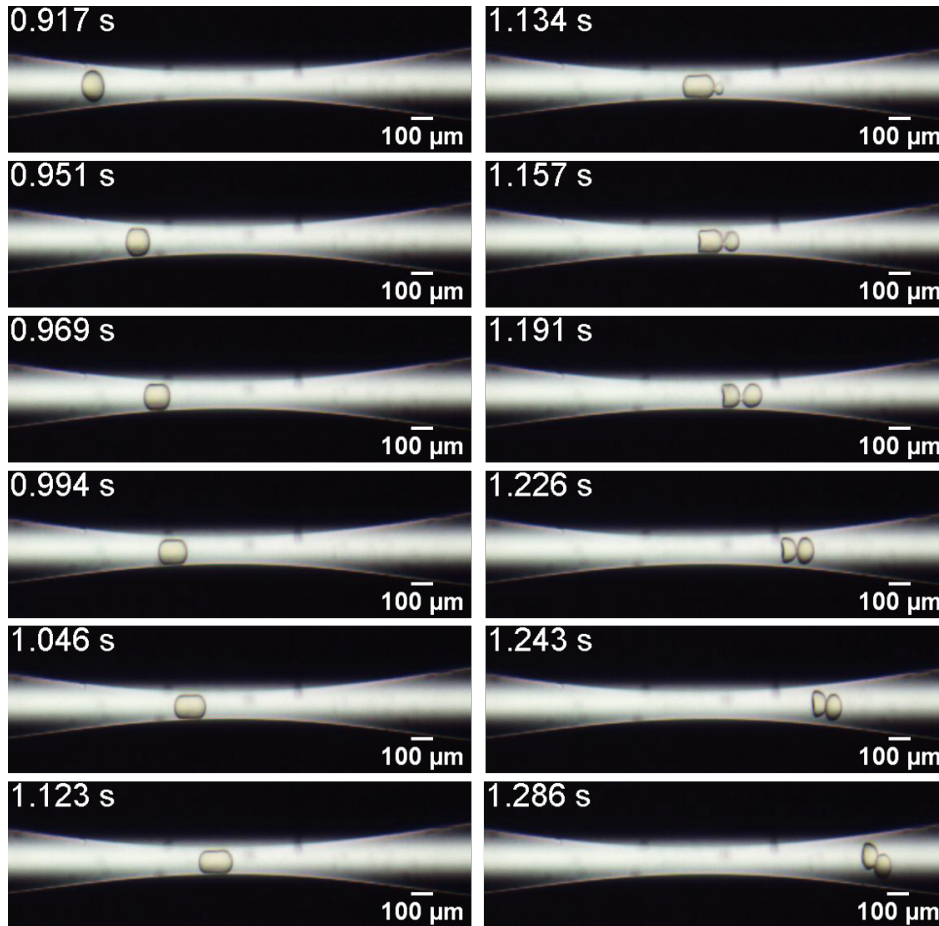


Figure 4.12: Evolution of the microcapsule position and configuration as it flows through the constriction. System #4, $D = 124.4 \mu\text{m}$ and $t = 5.6 \mu\text{m}$.

Table 4.2 summarizes the averaged maximum extra pressure-drop and deformation along the flow direction associated with the flow of the capsule through the constriction and the state of the capsule after flowing through the constricted capillary for the 5 systems tested. As mentioned before, experiments were repeated for at least 5 capsules of each system. The flow behavior was the same for all capsules of a same system. Table 4.2 also presents the standard deviation of the maximum pressure for each system. For systems #4 and #5, the maximum extra pressure drop was below the transducer resolution (2.07×10^{-3} MPa) and could not be measured.

| System ID | Ca_s | $\bar{a} = \frac{D}{D_c}$ | ΔP (MPa) | $\epsilon_{x,max} = \frac{L_{x,max}}{L_{x,0}}$ | ruptured |
|-----------|----------------------|---------------------------|-------------------------------|--|----------|
| #1 | 6.0×10^{-4} | 1.75 | $42.7 \pm 7.6 \times 10^{-3}$ | 1.81 | Yes |
| #2 | 1.4×10^{-3} | 1.44 | $4.97 \pm 1.1 \times 10^{-3}$ | 1.60 | Yes |
| #3 | 5.9×10^{-4} | 1.44 | $34.8 \pm 3.9 \times 10^{-3}$ | 1.71 | No |
| #4 | 1.6×10^{-3} | 1.24 | $<2.07 \times 10^{-3}$ | 1.36 | Yes |
| #5 | 1.7×10^{-3} | 1.09 | $<2.07 \times 10^{-3}$ | 1.47 | No |

Table 4.2: Maximum extra pressure-drop and deformation and state of the capsule after passing through the constriction for each system tested.

The effect of the capsule diameter, represented by \bar{a} , for a fixed shell thickness can be analyzed by comparing the flow behavior of capsules from systems #1 and #3 ($t \sim 15 \mu\text{m}$) at $Ca_s \approx 6 \times 10^{-4}$, and capsules from systems #2, #4 and #5 ($t \sim 5-6 \mu\text{m}$) at $Ca_s \approx 1.5 \times 10^{-3}$. As expected, the inlet pressure rises with capsule diameter, since larger capsules need to deform more to flow through the capillary throat. The increase in the deformation / stress with the capsule's diameter was enough to cause shell rupture.

Thicker shells lead to lower surface capillary number Ca_s , i.e. lower ratio between the viscous force, which drives deformation, and elastic force, which resists the deformation. Capsules that flow at lower surface capillary numbers are harder to deform and are also more resistant to rupture. This is clear by comparing the flow behavior of capsules from systems #2 and #3, which have the same diameter ($D \sim 144 \mu\text{m}$, $\bar{a} = 1.44$) and different shell thickness. Capsules from System #3, which have thicker shells and consequently lower surface capillary number, led to higher maximum inlet pressure and were able to flow through the constriction without releasing its inner phase.

Reversible deformation was only observed in microcapsules from systems #3 and #5, despite their differences in size and shell thickness. For a fixed capillary geometry and Reynolds number, the state of the capsule after flowing through the constriction, i.e. shell rupture or reversible deformation, is a function of the dimensionless capsule diameter \bar{a} and surface capillary number Ca_s . Figure 4.13 shows a map of the five systems tested in the parameter space \bar{a} vs. Ca_s . The capsules in the right-top portion of the plot, i.e. high capsule to throat diameter ratio and surface capillary number, rupture as they flow through the constriction. At a fixed capsule diameter, there is a critical surface capillary number above which the capsule bursts. This critical surface capillary number value decreases with capsule diameter. If the application requires capsules that release their content triggered by external stress caused by flow through constricted channels, the dimensionless parameters of the flow should be above the transition zone of Fig. 4.13; if the

capsule is designed to change the flow mobility in porous media or require to flow through constricted passages without releasing their inner phase content, the flow dimensionless parameter should be in the region below the transition zone. Experiments with different constriction geometries, flow rate and shell material may enable the development of a general phase diagram-like plot that could be used to design capsules accordingly to their applications.

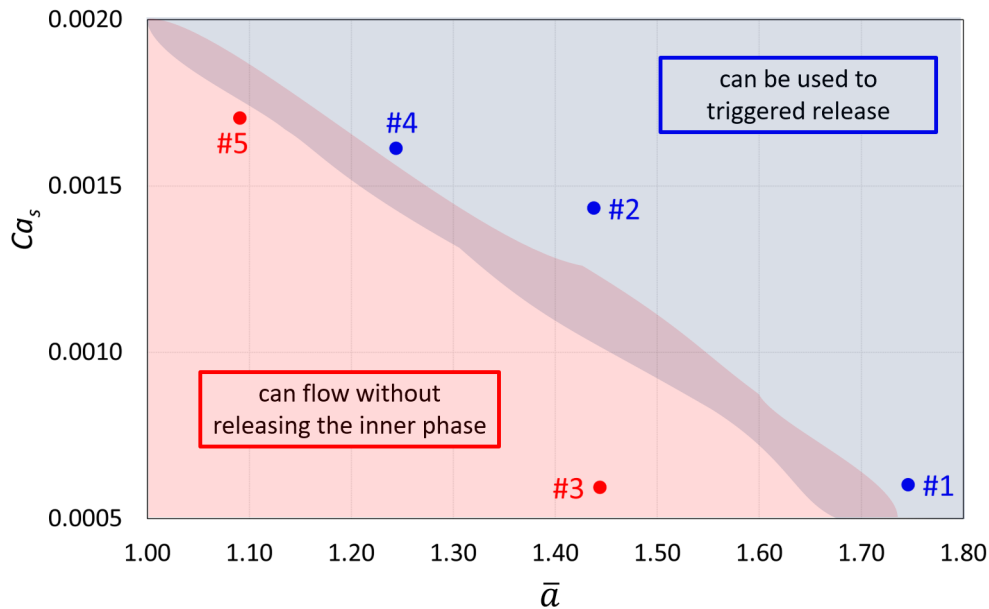


Figure 4.13: Map of state of capsule after flowing through the constriction as a function of dimensionless capsule diameter \bar{a} and surface capillary number Ca_s : (●) reversible deformation and (●) rupture.

4.4

Conclusions

The deformation dynamics of soft microcapsules as they flow through a constricted capillary strongly depends on the capillary geometry, capsule dimensions and properties and flow rate. If the stress imposed by the flow is higher than what the capsule shell can sustain, it will rupture and release its internal content. At a fixed capillary geometry and flow rate, the dynamics of the flow is a function of the ratio between the capsule diameter and capillary throat diameter, which defines the degree of deformation needed to flow the capsule through a constriction, and the surface capillary number, which represents the ratio of the viscous forces that deform the capsule and the elastic force that resists deformation.

Simultaneous flow visualization and pressure difference measurements presented in this Section enabled the detailed analysis of the flow and the effect of surface capillary number and dimensionless capsule diameter. Moreover, pressure

difference, capsule speed and deformation data reported can be used in the validation of different numerical models of the problem.

The results show that for the conditions explored, at each level of imposed deformation, which can be characterized by the capsule to constriction diameter ratio, there is a critical surface capillary number above which the membrane ruptures. The results should be used in the design of capsules for specific applications, i.e. if the release of its inner content should occur or not during the flow through constricted channels.

5 Gastroresistant microcapsules

5.1 Introduction

As discussed before, microcapsules have an important role in food and pharmaceutical industries due to their capacity to improve ingredient handling, to mask undesirable flavors, odors and colors and to protect different components from chemical or physical degradation during storage or after ingestion, controlling the release of the encapsulated ingredient [40, 155]. Microcapsules reduce the need for multiple dosing, since they guarantee a continuous therapeutic effect, which increases patient's convenience [47].

The rise on the market of healthy, vegetarian, vegan and sustainable supplies have expanded the interest on functional products which contain biologically active ingredients that can confer a health benefit on the host, such as antioxidants, probiotics or enzymes [156, 157, 158]. The incorporation of such ingredients in snacks, bars, beverages and shots is enabled by microencapsulation.

Oral route is the most preferred administration mode due to ease of ingestion, pain avoidance and public compliance [159]. However, it involves withstanding the harsh gastrointestinal tract as many active ingredients have to be delivered to the intestine or other organs, after passing through the stomach.

Considering the new vegan and vegetarian trends on consumers' needs and requirements, finding an appropriate shell material can be a major challenge, since the most used encapsulants are animal-based [156]. Most biodegradable polymers are biocompatible and thus very attractive as shell materials, especially when the application involves interaction with living organisms and natural degradation of microcapsules. Thus, gellan gum emerges as a promising encapsulant. It is a natural, non-toxic, biocompatible polymer approved by USFDA, EU and the World Health Organization (WHO). It is widely used in food products as texture agent since it is capable of forming transparent hydrogels that are stronger and less permeable than the largely used alginate-based ones. Gellan gum is secreted by the bacterium *Sphingomonas elodea* and animal products are not applied in its production process. In fact, it has already been used to replace gelatin in desserts and gummies, making them vegetarian.

As explained in Chapter 2, gellan gum gels are thermo [102] and pH-responsive [109]. Therefore, gellan microcapsules can be used for controlled or targeted release based on the surroundings temperature and pH, which can be set as process triggers.

In this chapter, the pH responsive property of gellan gum is explored, seeking the encapsulation of hydrophobic active compounds to be targeted delivery in the intestine after passing through the stomach. Thus, gellan gum microcapsules are submitted to a gastroresistance test. It is a static *in vitro* digestion simulation that follows a standardized protocol proposed by an international network of multidisciplinary experts from several countries in 2014 [6] and improved in 2019 [160]. In static digestion simulation, experimental conditions are constant during each phase.

Due to their high velocity and reproducibility, low cost and ease of handling, *in vitro* methods for simulating digestion processes are widely used to study the gastrointestinal behaviour of food or pharmaceuticals. Moreover, this kind of test does not present ethical restrictions and allows a simultaneous examination of a relatively large number of samples [6, 160]. However, it is important highlighting the need of dynamic models for a more accurate simulation of *in vivo* conditions since *in vitro* method is not suitable for simulating digestion kinetics, being indicated to assess digestion endpoints only.

5.2

Experimental set-up and methodology

The microcapsules used in these experiments have $160 \pm 3 \mu\text{m}$ of diameter and $6 \pm 2 \mu\text{m}$ of shell thickness. The inner phase, composed of a refined commercial sunflower oil (Liza, Cargill Agricola S.A., Brazil) and labeled with an orange food-grade dye and a fluorescent pigment called oil Glo 22 (Spectroline, Spectronics Corporation, USA), can be visualized in a fluorescent microscope. This is how the integrity of microcapsules is verified.

Digestion involves the exposure of food to three successive digestive phases: oral, gastric and intestinal. However, simulating the oral phase of digestion is not required mainly due to the very short residence times in the oral cavity [6]. Hence, the protocol only embraces gastric and intestinal phases.

In the gastric phase, the microcapsules are suspended in a solution of simulated gastric fluid (SGF) and pepsin (2000 U/mL) in a beaker and kept under agitation at pH 3.0 for 2 hours. After that, the entire content is diluted 1:1 (vol/vol) with simulated intestinal fluid (SIF), bile salts (10 mM) and pancreatic enzymes (pancreatin based on the activity of trypsin: 100 U/mL) and maintained at pH 7 for 2 more hours. After each phase, some microcapsules are collected and observed in an inverted microscope (model DMi8, Leica Microsystem, Germany) equipped with a fluorescent

module, which allows visualization of the inner phase of the microcapsules.

Simulated Gastric Fluid (SGF) and Simulated Intestinal Fluid (SIF) were prepared following Minekus et al. [6] guidelines. They consist of the corresponding electrolyte stock solution, water, enzymes and CaCl_2 . The last two components are added only during the assay. The recommended concentrations of electrolytes in each of the fluids is presented in Table 5.1. More details on how to prepare the simulated fluids can be found in the above-mentioned protocols [6, 160].

| Constituent | SGF | SIF |
|---------------------------------------|--------|--------|
| | mmol/L | mmol/L |
| K^+ | 7.8 | 7.6 |
| Na^+ | 72.2 | 123.4 |
| Cl^- | 70.2 | 55.5 |
| H_2PO_4^- | 0.9 | 0.8 |
| HCO_3^- , CO_3^{2-} | 25.5 | 85 |
| Mg^{2+} | 0.1 | 0.33 |
| NH_4^+ | 1.0 | - |
| Ca^{2+} | 0.15 | 0.6 |

Table 5.1: Recommended concentrations of electrolytes in Simulated Gastric Fluid (SGF) and Simulated Intestinal Fluid (SIF), based on human *in vivo* data. Reproduced from [6].

5.3

Results and discussion

Before submitting the microcapsules to digestion simulation, a baseline image of the intact microcapsules was taken showing the fluorescent dye integrity (Fig. 5.1).

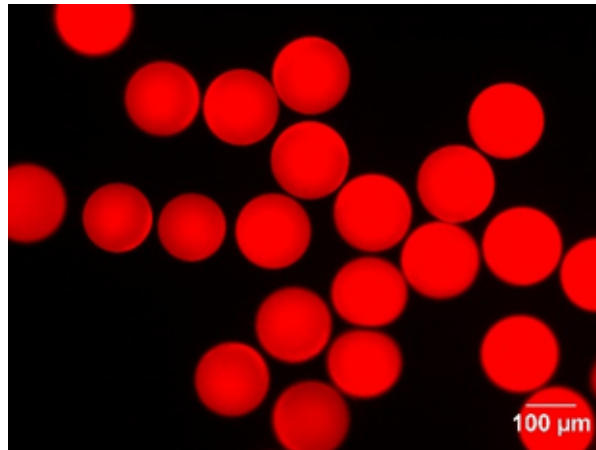


Figure 5.1: Confocal image of the inner phase of gellan microcapsules before static in vitro digestion simulation.

Fluorescent images of the microcapsules were also made during the gastric (after 1 hour) and at the end of it (after 2 hours) and are presented in Figures 5.2(a) and 5.2(b), respectively. These images show the inner content of each microcapsule, indicating their integrity during the entire gastric phase. Thereby, it is confirmed that the gellan gum microcapsules support the conditions of the stomach, being gastroresistant. In fact, as discussed in Chapter 2, when gellan gum is exposed to low pH values, the ionic strength increases, diminishing the repulsion between gellan double helixes which makes the polymer stronger [101]. Thus, the gellan gum shell of the microcapsules are actually reinforced in the stomach due to its acid pH (3.0), protecting their inner content and making them arrive intact to the intestine.

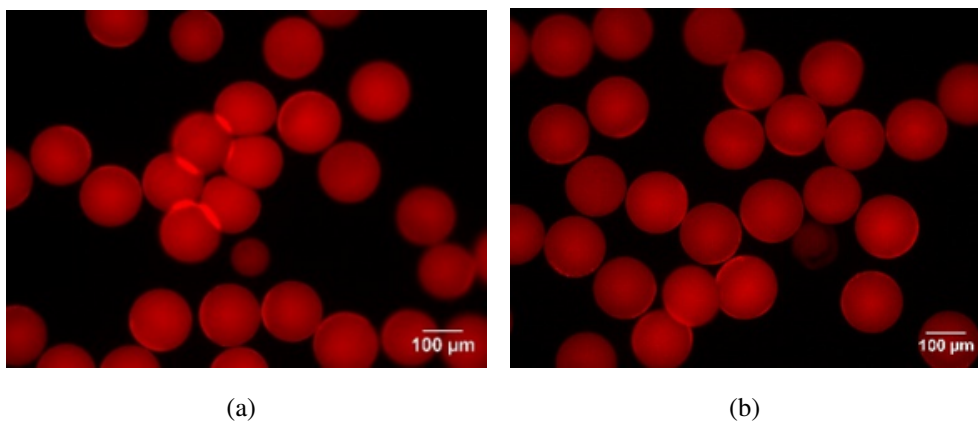


Figure 5.2: Fluorescent image of the inner phase of gellan microcapsules after (a) 1 hour and (b) 2 hours in gastric conditions.

After the gastric phase, the microcapsules were then exposed to intestinal conditions. From Figures 5.3(a) and 5.3(b), it is seen that after 1 hour, most of the microcapsules already had their shell ruptured and that, after 2 hours, all of

them were ruptured and the inner content was released. Contrarily to what happens in the stomach, there is an increase in pH which decreases the ionic strength and increases the repulsion between gellan double helices [101], weakening the protection rendered by the polymeric shell. Moreover, pancreatin has been reported as effective in breaking down gellan networks, even though it is not a specific enzyme for polysaccharide hydrolysis [158]. Thereby, the microcapsule's cargo is released in the intestine.

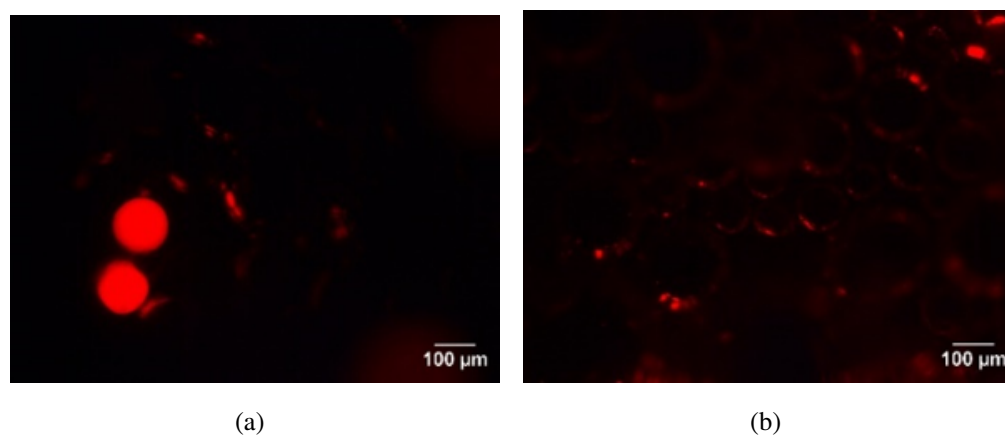


Figure 5.3: Fluorescent image of the inner phase of gellan microcapsules after (a) 1 hour and (b) 2 hours in intestinal conditions.

5.4 Conclusions

Gellan microcapsules have appropriate characteristics to food and pharmaceutical applications, filling the new consumers' requirements of being vegetarian and sustainable. The *in-vitro* digestion simulation experiment showed that the gellan microcapsules produced through microfluidics are gastro-resistant and able to release their inner content in the intestine due to the response of the gellan material to pH variations and pancreatin activity. Hence, this is a first evidence that they are suitable for encapsulating hydrophobic antioxidants, probiotics and enzymes, while being suspended in an aqueous or oily medium. Hydrophilic components can also be targeted delivery in the intestine if incorporated to the gellan shell. However, tests of encapsulation and culture of these compounds for quantification are still required.

6

Magnetic microcapsules

6.1

Introduction

A magnetic dipole can be defined as a pair of magnetic poles of opposite signs separated by a small distance. It generates a magnetic field and experiences torque in the presence of external magnetic fields, trying to align itself with them. The strength and orientation of the magnetic dipole is called magnetic dipole moment and indicates its ability to align to an external magnetic field.

Ferrofluids are liquids made of nanometer-sized magnetic particles (dipoles) suspended in a nonmagnetic carrier fluid. Usually, the volume fraction of magnetic particles ranges from 2 to 15 vol% [161]. Ferrofluids have special properties that make them useful in many technological, biological and medical applications. They react to an external magnetic field by moving towards regions with greater field magnitudes and possibly adjusting their physical properties but usually do not retain magnetization in the absence of the externally applied magnetic field for a long time (being classified as super-paramagnetic materials). Moreover, they heat up as absorbing electromagnetic energy [162]. Therefore, ferrofluids are commonly applied in loudspeakers, hard disks, damping, magnetic hyperthermia, magnetic resonance imaging (MRI) and in gene and drug delivery, for example [161, 162, 163].

Each application requires a specific concentration of magnetic material and carrier solvent and saturation magnetization (maximum value of the magnetic moment per unit volume when all the domains are aligned). For biomedical applications, biocompatibility and nontoxicity are also crucial. The most common nanoparticle used as magnetic phase is magnetite Fe_3O_4 due to its high Curie temperature, high saturation magnetization, reasonably magnetic stability and affinity to living cells [161, 163].

It is possible to incorporate ferrofluids to the core or polymeric shell of microcapsules, which then present similar superparamagnetic properties of the original magnetic fluid [54, 55, 164]. These microcapsules can be manipulated by external magnetic forces to aggregate, align and deform, being suitable to mimic artificial muscular contractions or to develop small reactors and nanomachines with tailor-

made properties [55], for example.

Microcapsules with magnetic properties can be employed as vehicles for triggered release of the encapsulated material enabling the remote control of their location by an external magnetic field. Their use is related to a fast and effective accumulation of drugs in a specific area, which is beneficial for patients because it avoids side effects, since only pathological cells are affected [165, 166, 167], and reduces dosing frequency [155]. *In-vitro* and *in-vivo* tests have shown that external remote triggers, such as light, pH and ultrasound, can be used to induce drug release after the capsules arrive to the right part of the body [165, 168].

Huang et al. [56] produced eccentric magnetic PDMS microcapsules with great potential for diagnostics and therapeutics. They are simultaneously suitable for MRI-guided local injection once the magnetic nanoparticles can be easily tracked by MRI scanners and pH-regulated drug release since the PDMS shell embedded with magnetic nanoparticles dissolves in acid environments. Voronin et al. [57] performed *in-vitro* and *in-vivo* experiments that show magnetic microcapsules being trapped in bloodstream by the local application of a permanent magnetic field. Although the capsules may have aggregated the flow remained intact. This is particularly interesting for cancer treatments which require guiding drug-filled capsules to the tumor area.

The effect of an external magnetic field on the deformation and breakup of elastic capsules that contain ferrofluids due to an external uniform magnetic field has also been studied [164]. Such capsules take an elongated shape as the magnetic field is applied until they burst at high field strengths. Similar behavior has been observed when an electric field was applied [169].

In this chapter, magnetite is incorporated to gellan-based microcapsules, providing them magnetic properties. The same procedure described in Chapter 3 is used to produce these microcapsules. The ferrofluid is added to the inner phase and Fe_3O_4 nanoparticles are considered to be biologically and chemically inert. As discussed before, gellan microcapsules are also biocompatible. Therefore, magnetic gellan microcapsules present all the requirements for the applications described above.

Additionally, ferromagnetic W/O/W microcapsules are produced with a different polymer: polydimethylsiloxane (PDMS). In this case, a ferrofluid is added to the inner phase as well as to the polymeric matrix. PDMS is a synthetic cross-linkable elastomer with valuable characteristics such as ease of fabrication, resistance to oxidation, thermo-tolerance, flexibility and tunable hardness. It has been explored as shell material for microcapsules enabling the adjustment of their stiffness by changing the ratio between the PDMS polymer and cross-linker [64].

Then, a magnetic experiment is carried out to establish how these capsules suspended in water respond to an external magnetic field and how the composition

of the capsule affects the magnetic response.

6.2

Experimental set-up and methodology

6.2.1

Ferrofluids

Two ferrofluids from Ferrotec Corporation were used in this part of the research, namely EMG 601P, which is aqueous, and EFH 1, which is oily. The first is composed of 1.2-7.9 vol% of magnetite particles, 6-22 vol% of water soluble dispersant (cationic) and 70.1-92.8 vol% of deionized water. The second is composed of 3-15 vol% of magnetite particles, 6-30 vol% of oil soluble dispersant and 55-91 vol% of distillates (petroleum) hydrotreated light.

The main properties of both ferrofluids are listed on tables 6.1 and 6.2.

| | |
|--------------------------|-------------------------------|
| Saturation magnetization | 44mT |
| Density | 1340 kg/m ³ @ 25°C |
| Viscosity | <4 mPa.s @ 27°C |
| pH | 8.5-9 |

Table 6.1: Main properties of the water-based ferrofluid EMG 601P from Ferrotec Corporation.

| | |
|---------------------------------|-------------------------------|
| Saturation magnetization | 44mT |
| Density | 1210 kg/m ³ @ 25°C |
| Viscosity | 6 mPa.s @ 27°C |
| Pour point | -94°C |
| Flash point | 92°C |
| Initial magnetic susceptibility | 2.64 |

Table 6.2: Main properties of the oil-based ferrofluid EFH1 from Ferrotec Corporation.

6.2.2

Production of magnetic microcapsules

Gellan gum shell: The set-up to produce magnetic gellan microcapsules was the same to produce the original gellan gum microcapsules detailed in Section 3.2. It includes (i) one three-dimensional coaxial microfluidic device; (ii) an inverted microscope (model DMi8, Leica Microsystem, Germany) equipped with a high speed camera (model Fastcam SA-3, Photron, USA); (iii) three syringe-pumps

(model Pump 11 from Harvard Apparatus, USA) to control the flow rates of the microcapsules phases; (iv) three BD plastic syringes; and (v) four flexible hoses with an outer diameter of 1.32 mm and an inner diameter of 0.864 mm.

Briefly, the microfluidic glass device was made of two cylindrical capillaries: one hydrophilic, for the injection of the inner phase, and the other hydrophobic, for the collection of the O/W/O templates. They were both nested into the opposite ends of a square capillary. In this case, the tips of the injection and collection capillaries were sanded to the final inner diameters of 80 μm and 350 μm , respectively. The distance between them was fixed at 120 μm . The middle and continuous phases were pumped in opposite directions through the interstices between the cylindrical and square capillaries.

Microcapsules were firstly collected in hexane and then dispersed in acetate buffer, after which hexane evaporated.

The original microcapsules were made of: a refined commercial sunflower oil (Liza, Cargill Agrícola S.A., Brazil) labeled with an orange food-grade dye as inner phase; a mixture of 0.5 wt% low-acyl gellan gum Kelcogel CG-LA (CP Kelco Brasil S/A, Brazil) and 2 wt% polyoxyethylene sorbitan monolaurate, Tween® 20 (Sigma-Aldrich, USA), in ultrapure water with resistivity 18.2 $\text{M}\Omega/\text{cm}$ (Direct-Q3 UV System, Millipore Co., USA) as middle phase; and a sunflower oil dispersion containing 1 wt% calcium acetate (Sigma-Aldrich, USA) and 5 wt% polyglycerol-polyricinoleate commercially named Grinstead PGPR super (Danisco Brasil, Brazil) as continuous phase. To magnetize them, two different percentages of the oil-based (EFH1, Ferrotec Corporation) were added to the inner phase, as following:

- Magnetic inner phase A: 75 wt% EFH1 ferrofluid + 25 wt% original inner phase
- Magnetic inner phase B: 100 wt% EFH1 ferrofluid

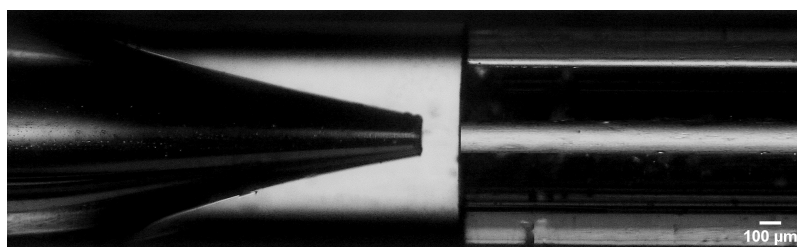
We also tried to disperse the aqueous ferrofluid, EMG 601P, in the gellan gum so that the capsules had a magnetic shell. However, the gelation of the polymer started immediately after both fluids got in contact, hindering the use of the mixture to form microcapsules. Probably, there is a component of the ferrofluid that acts on the gelation of gellan gum.

PDMS shell: For the production of PDMS-shelled microcapsules, a slightly different microfluidic device was used, as shown in Figure 6.1(a). It also has two cylindrical capillaries (OD 1.0 mm, ID 0.58 mm, manufactured by World Precision Instruments, Inc.) nested into a square capillary (OD 1.5 mm, ID 1.05 mm, manufactured by Atlantic International Technology, Inc.). The injection capillary is pulled with a micropipette puller (P-1000, Sutter Instrument) to a tapered opening

of 40 μm and subsequently sanded to a diameter of 150 μm (left capillary in Fig. 6.1(b)). This capillary is then treated with a commercial rain repellent Glass Shield (Inove Pack do Brasil, Brazil) to render a hydrophobic surface whereas the unmodified cylindrical collection capillary (right capillary in Fig. 6.1(b)) is treated with a polyelectrolytes solution composed of 1 wt% of poly(acrylamide-co-diallyldimethylammonium chloride) (Sigma-Aldrich, USA) and 2 mol/L NaCl to render a hydrophilic surface. Both cylindrical capillaries are coaxially aligned at a distance of 225 μm .



(a)



(b)

Figure 6.1: Device for PDMS microcapsules production: (a) photo of the coaxial glass-capillary device and (b) detail of the injection and collection capillaries.

Regular PDMS microcapsules can be produced with the inner phase being Milli-Q water (Direct-Q3 UV System, Millipore Co., USA); the middle fluid being the PDMS (Sylgard 184® from Dow Corning base and curing agent) and the outer phase being a 10% polyvinyl alcohol (PVA) solution [64]. The PVA increases the water viscosity and acts as a surfactant. The W/O/W templates formed in the microfluidic device should be collected in Milli-Q water and rotate for 1 week. This ensures that the inner and outer droplets are concentric upon curing at room temperature.

In this research, all PDMS microcapsules were made at a 10:1 ratio with the curing agent.

Similarly to what was made to the gellan microcapsules, to magnetize PDMS microcapsules, different percentages of the water-based (EMG 601P) ferrofluid of magnetite were added to their inner phase, as following:

- Magnetic inner phase A: 25 wt% EMG 601P ferrofluid + 75 wt% original inner phase
- Magnetic inner phase B: 75 wt% EMG 601P ferrofluid + 25 wt% original inner phase
- Magnetic inner phase C: 100 wt% EMG 601P ferrofluid

Moreover, PDMS capsules with ferrofluid in the shell were also produced by mixing 25 wt% of the oil-based (EFH1) ferrofluid with 75 wt% of the original middle phase (10:1 PDMS).

6.2.3

Magnetic response test

To assess the response of the magnetic microcapsules to an applied magnetic field, two bar magnets were used. Each one was composed of six 5.0 mm cubic magnets. Table 6.3 presents the value of the magnetic field measured at three different distances from magnets from ImaShop which are similar to the ones used in the experiments.

| Distance (mm) | Magnetic Field (G) |
|---------------|--------------------|
| 0 | 5274 |
| 2 | 2089 |
| 5 | 549 |

Table 6.3: Magnetic field measured at 3 distances from the magnet. Data available in the magnets technical file from ImaShop.

The magnets were aligned at a distance of 5.58 mm and a plastic tube with outer diameter of 1320.8 μm and inner diameter of 863.6 μm was used to flow the microcapsules suspended in milli-Q water between them. Both magnets had their south pole closer to the plastic tube so they repel each other, as shown in Fig. 6.2.

The field lines proximity (or spatial density) indicates the magnitude of the magnetic field in each position. The more tightly-packed the lines are, the stronger the magnetic field is. The magnetic force that attracts objects to a magnet is always tangent to the magnetic field lines, and it also depends on the object's magnetic dipole moment.

Due to their paramagnetism, microcapsules with ferrofluids, when submitted to an external magnetic field, also become magnetic dipoles aligned with the applied field direction, and consequently they are weakly attracted by magnets as they draw near to them. Therefore, if a capsule is close enough (positions B and D in Fig. 6.2), its north pole points to the south pole of the magnets as each magnet exerts an

attraction force on it that is tangent to the magnetic field line (red arrows). In this case, the net magnetic force (orange arrow) is not zero and it is always in the x (flow) direction, acting to bring the capsule closer to the magnets. Thus, when the capsule is in position B, the net force is positive and acts in the same orientation of the drag force (blue arrow). On the other hand, when the capsule is in position D, the net magnetic force is negatively oriented and competes with the drag force.

Between the two south poles in Fig. 6.2 (position C), the magnetic field is very weak because the density of magnetic lines is almost zero and the magnetic forces exerted by the magnets (red arrows) cancel each other since they have the same modulus but act in opposite orientations.

A capsule that is far away from the magnets does not feel any magnetic field (position A in Fig. 8); the only force driving it is the drag force (blue arrow) generated by the flow.

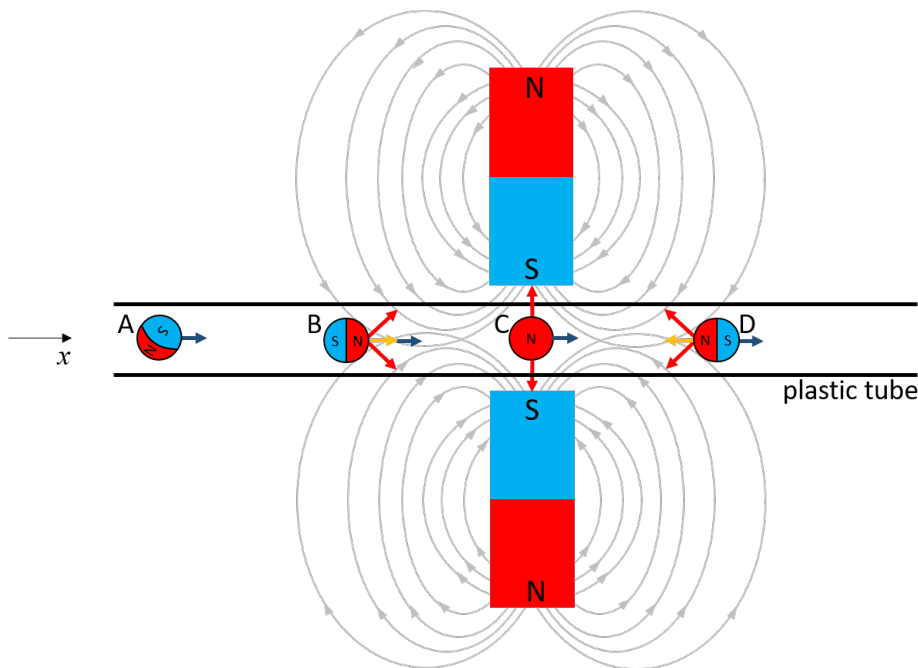


Figure 6.2: Schematic of a magnetic capsule flowing between magnets. Black arrows represent magnetic field lines.

The magnets and the plastic tube were assembled on a device made of PLA and Clear resin pieces printed by two 3D printers, Ultimaker 3 Extended and Forms 2, especially for this purpose (Fig. 6.3). A syringe-pump (model Pump 11 from Harvard Apparatus) and a 10 mL BD plastic syringe were used to control the flow rate and a Nikon stereomicroscope (model SMZ-745T) equipped with a high speed camera (model IL5 from Fastec Imaging) was used to monitor and record the experiments. The entire experimental set-up is shown in Fig. 6.4 and a simplified scheme is presented in Fig. 6.5.

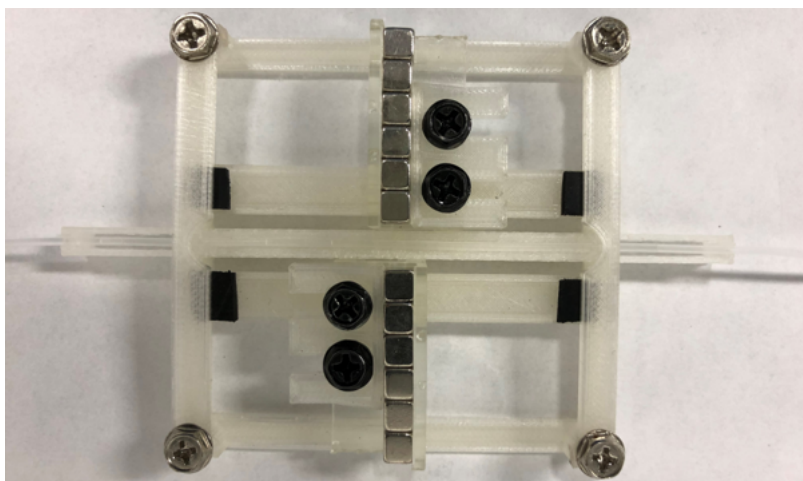


Figure 6.3: 3D printed device with magnets and hose used to flow microcapsules between magnets.

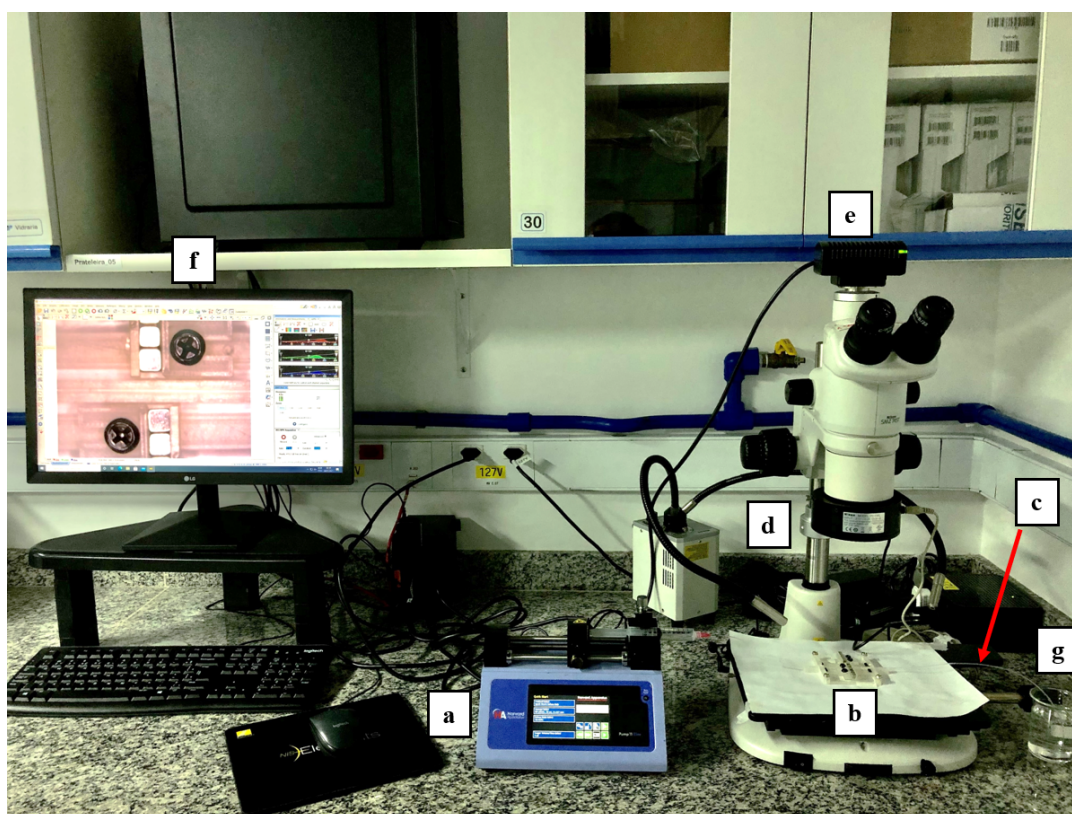


Figure 6.4: Experimental set-up for flowing microcapsules between magnets: (a) a syringe pump; (b) the 3D printed device; (c) a plastic tube; (d) an stereomicroscope; (e) a high speed camera; (f) a computer for real time visualization and (g) a dispensing beaker.

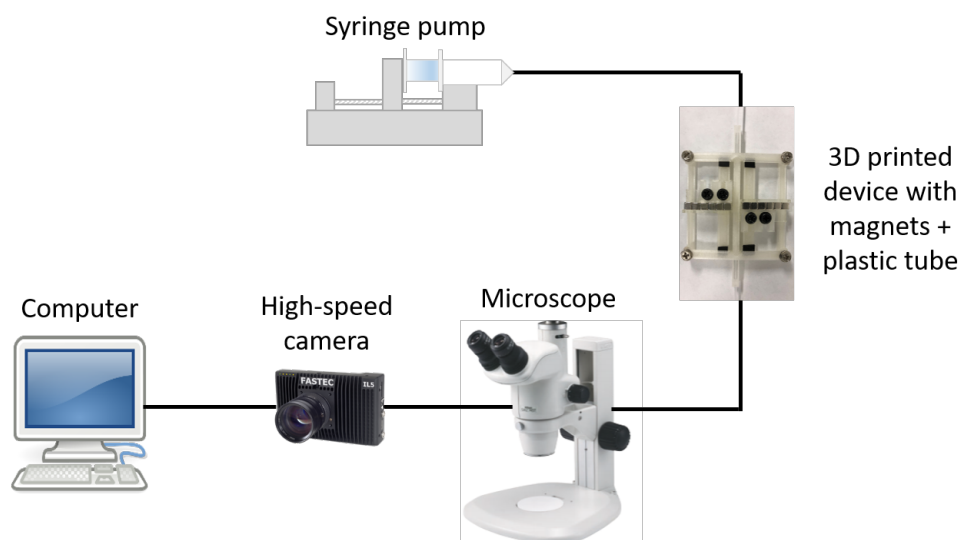


Figure 6.5: Scheme of the experimental set-up for flowing microcapsules between magnets.

Results were all obtained at constant flow rates. The range of flow rates explored varied according to the microcapsule being tested. Depending on the composition and size of the capsules, the minimum flow rate required to make it pass through the magnets varied. This value can be related to the capsule's response to the external magnetic field.

Experiments were repeated for at least 3 different capsules of each system.

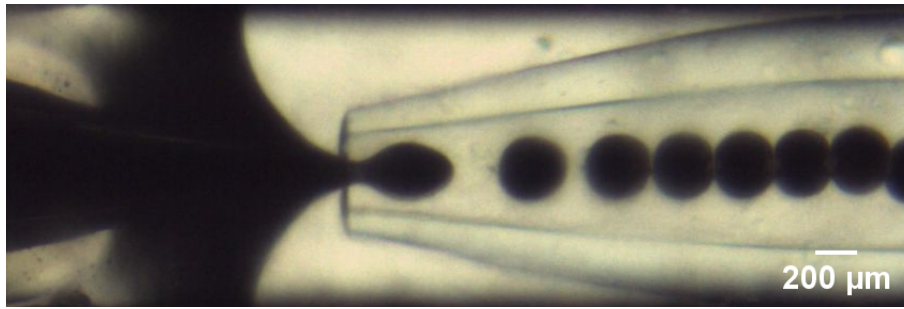
After performing the experiments, all images were extracted from the videos and processed with a Matlab code based on frame difference to detect the moving capsules. The images were converted into grayscale and, after denoising, into binary images. After that, morphological operations were performed and small unwanted objects were removed from the background.

The length scale was determined from the known tube outer diameter. The position of the microcapsules centroid (x_c) was measured in each frame.

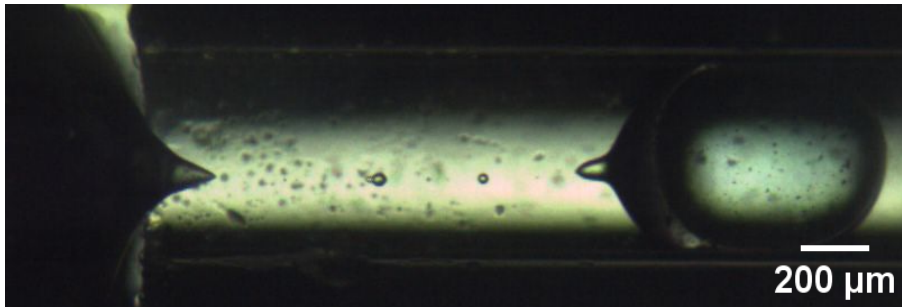
6.2.4

Results and discussion

The dripping flow regime (Fig. 6.6), in which the interfaces between the inner and middle phases and between the middle and continuous phases break simultaneously at the same spatial location and frequency, was achieved in all cases. So, monodispersed magnetic microcapsules made of gellan gum and PDMS were produced with different diameters and shell thicknesses.



(a)



(b)

Figure 6.6: Production of monodispersed (a) gellan magnetic microcapsules with ferrofluid as inner phase and (b) PDMS magnetic microcapsules with ferrofluid in the shell.

Some batches were used in the magnetic response test. The ones with magnetic cores are listed in Table 6.4 while the ones with magnetic shells are listed in Table 6.5. The diameter and shell thickness presented are the mean value of 10 measurements made for each batch with their standard deviation, except for the shell thickness of the PDMS microcapsules with ferrofluid in the shell. Due to the ferrofluid dark color, it was not possible to visually distinguish the shell internal limits to measure its thickness. Therefore, a relation between the shell thickness t , the capsule diameter D , and the middle and inner phase flow rates Q_m and Q_i presented by do Nascimento et al. [64] was used to estimate it (Eq. 6-1). The flow rates to produce the capsules from each system are listed in Table 6.6.

Because the dimensions of the microfluidic device used to form PDMS templates are bigger than the dimensions of the device used to form gellan templates, the PDMS microcapsules are bigger than the gellan gum ones. Nevertheless, all capsules were smaller than the tube diameter (863.6 μm).

$$\frac{t}{D} = 1 - \left(1 - \frac{Q_m}{Q_i}\right)^{1/3} \quad (6-1)$$

| System ID | Shell material | Ferrofluid wt% | D (μm) | t (μm) |
|-----------------|----------------|----------------|-----------------------|-----------------------|
| Gellan-core-75 | Gellan gum | 75 | 221.0 ± 3.6 | 15.7 ± 1.9 |
| Gellan-core-100 | Gellan gum | 100 | 244.1 ± 3.4 | 22.0 ± 7.2 |
| PDMS-core-25 | PDMS | 25 | 622.3 ± 4.6 | 61.0 ± 6.8 |
| PDMS-core-75 | PDMS | 75 | 635.1 ± 6.2 | 71.6 ± 7.3 |
| PDMS-core-100 | PDMS | 100 | 655.3 ± 3.7 | 54.9 ± 4.7 |

Table 6.4: Main properties of microcapsules with magnetic cores used in the magnet experiments.

| System ID | Shell material | Ferrofluid wt% | D (μm) | t (μm) |
|-----------------|----------------|----------------|-----------------------|-----------------------|
| PDMS-shell-25-1 | PDMS | 25 | 613.0 ± 4.6 | 56.0 |
| PDMS-shell-25-2 | PDMS | 25 | 590.1 ± 3.9 | 122.0 |
| PDMS-shell-25-3 | PDMS | 25 | 601.0 ± 4.4 | 222.0 |

Table 6.5: Main properties of PDMS microcapsules with magnetic shells used in the magnet experiments. Shell thicknesses were calculated by Eq. 6-1.

| System ID | Q_i ($\mu\text{L/h}$) | Q_m ($\mu\text{L/h}$) | Q_o ($\mu\text{L/h}$) |
|-----------------|---------------------------|---------------------------|---------------------------|
| Gellan-core-75 | 100 | 100 | 1000 |
| Gellan-core-100 | 100 | 150 | 1500 |
| PDMS-core-25 | 500 | 500 | 6000 |
| PDMS-core-75 | 500 | 750 | 6000 |
| PDMS-core-100 | 1000 | 750 | 6000 |
| PDMS-shell-25-1 | 1000 | 250 | 6000 |
| PDMS-shell-25-2 | 1000 | 500 | 6000 |
| PDMS-shell-25-3 | 1000 | 750 | 6000 |

Table 6.6: Flow rates applied to form magnetic microcapsules.

Figure 6.8 shows the time evolution of the centroid position of a microcapsule from System Gellan-core-75 for different flow rates. It is possible to see that the capsule velocity is reduced as it flows between the magnets but, for most of the flow rates tested, it ended up passing by the magnets. Only the lower flow rates, i.e. 170 mL/h, 180 mL/h and 190 mL/h, resulted in magnetic forces strong enough to hold the capsule near the magnets. The centroid position (x_c) stops varying in these cases slightly after the magnetic lines stagnation point between the magnets ($x_c = 0$). In these equilibrium conditions, the net force acting on the capsules is zero and the magnetic force is equal to the drag force caused by the flow.

The drag force (F_D) on a stationary sphere in Poiseuille flow can be calculated by Eq. 6-2, where ρ is the fluid's density, \bar{V} is the average flow velocity, D is the

capsule diameter and C_D is the drag coefficient, which Song and Gupta [5] concluded to be a function of the Reynolds number (Re) and the sphere-to-tube diameter ratio (λ). Thus, this coefficient can be estimated through plots numerically obtained by the authors.

$$F_D = C_D \frac{1}{2} \rho \bar{V}^2 \left(\frac{\pi D^2}{4} \right) \quad (6-2)$$

In our experiments, the Reynolds number varied between 1.40 and 35.7 and the sphere-to-tube diameter ratio between 0.26 and 0.76, so we extrapolated data from Fig. 6.7 to obtain the drag coefficient in each case.

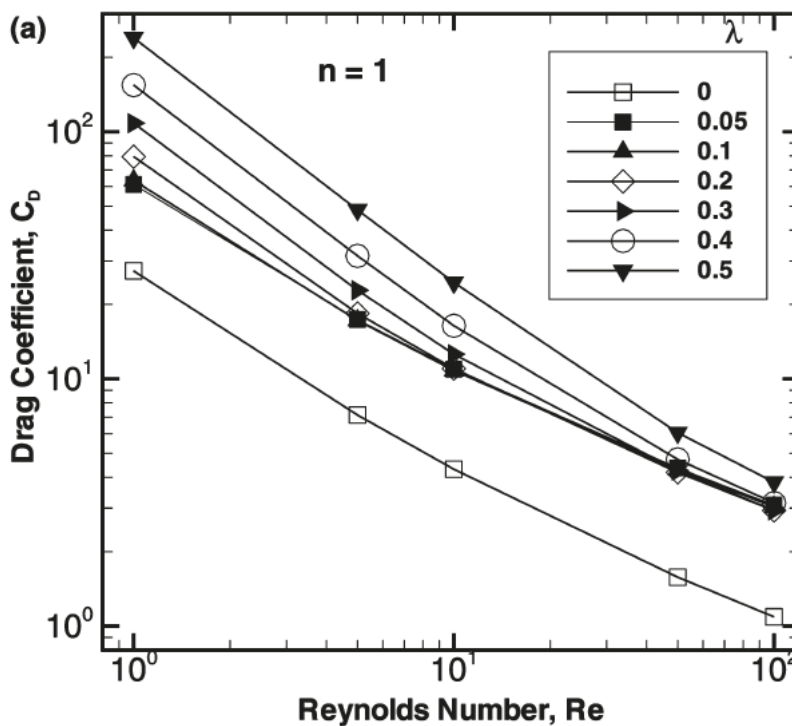


Figure 6.7: Dependence of drag coefficient on Reynolds number and sphere-to-tube diameter ratio for a Newtonian fluid. Reproduced from [5].

As the drag force that pushes the capsule in opposition to the magnetic force is proportional to the flow rate, the microcapsule stops closer to the magnets (lower magnetic force) when the flow rate is lower. At high flow rates, the net drag force was higher than the magnetic force and the capsules were able to flow through the tube. A drag force higher than $F_D \approx 1.2 \times 10^{-6}$ N was needed to overcome the magnetic force in this case. We consider this value to be the maximum magnetic force action on the capsule during the flow.

A similar behavior is seen in Fig. 6.9 for a gellan microcapsule with 100% of ferrofluid in its core (System Gellan-core-100). However, in this case, because the

amount of ferrofluid in microcapsule's inner phase is higher than for System Gellan-core-75, the maximum flow rate that makes the capsule stop is higher: 260 mL/h, which corresponds to $F_D \approx 2.1 \times 10^{-6}$ N. This clearly shows the effect of the capsule composition in its magnetic response.

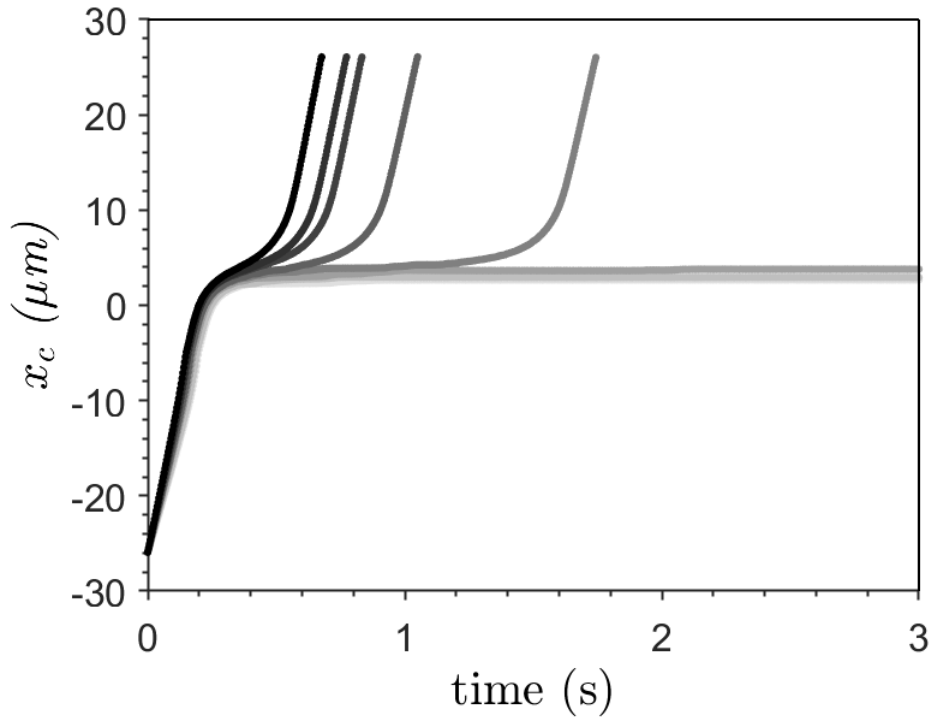


Figure 6.8: System Gellan-core-75 microcapsule centroid position (x_c) as it flows between the magnets for different flow rates: $Q =$ (●) 170 mL/h, (●) 180 mL/h, (●) 190 mL/h, (●) 200 mL/h, (●) 210 mL/h, (●) 220 mL/h, (●) 230 mL/h and (●) 240 mL/h. $x_c = 0$ corresponds to magnets center plane.

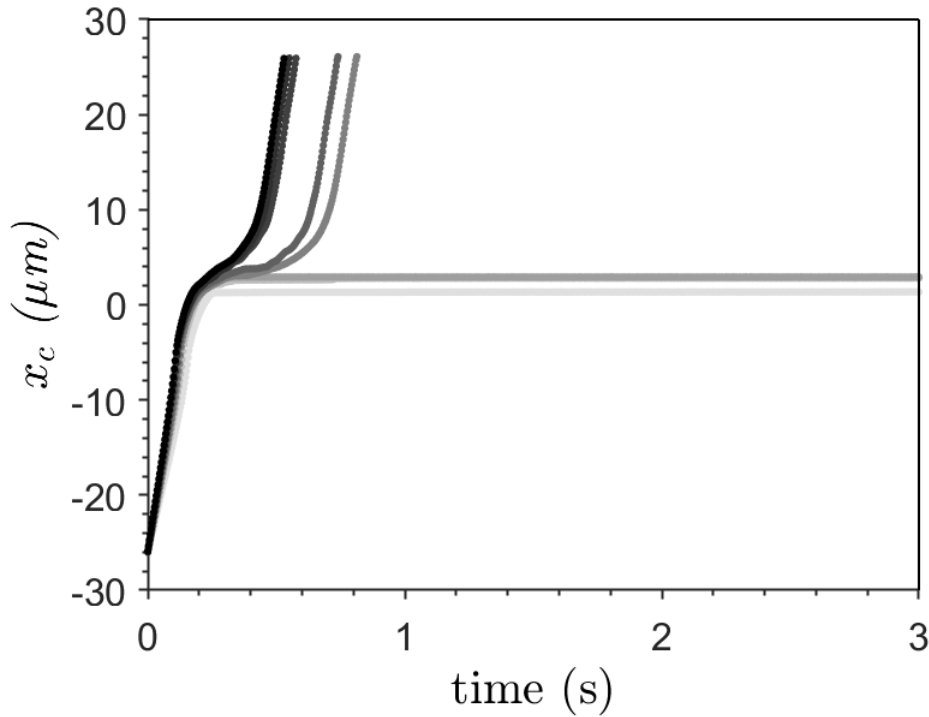


Figure 6.9: System Gellan-core-100 microcapsule centroid position (x_c) as it flows between the magnets for different flow rates: $Q =$ (●) 200 mL/h, (●) 250 mL/h, (●) 260 mL/h, (●) 270 mL/h, (●) 280 mL/h, (●) 290 mL/h, (●) 300 mL/h and (●) 310 mL/h. $x_c = 0$ corresponds to magnets center plane.

The PDMS microcapsules with magnetic nanoparticles suspended in the core presented the same trend, as can be seen in Figures 6.10, 6.11 and 6.12. As the amount of ferrofluid in the capsule's core is increased because of its larger diameter, the minimum flow rate necessary to make it flow between the magnets and pass through the magnetic field also increases. For System PDMS-core-25, with 25% of ferrofluid, it is 60 mL/h, while for System PDMS-core-75, with 75% of ferrofluid, it is 70 mL/h and for System PDMS-core-100, with 100% of ferrofluid, it is 100 mL/h. In these cases, the drag force has to be higher than $F_D \approx 4.2 \times 10^{-6}$ N, $F_D \approx 5.0 \times 10^{-6}$ N and $F_D \approx 9.2 \times 10^{-6}$ N, respectively, to overcome the magnetic force. The higher maximum magnetic force experienced by the PDMS capsules can be explained by their larger diameters.

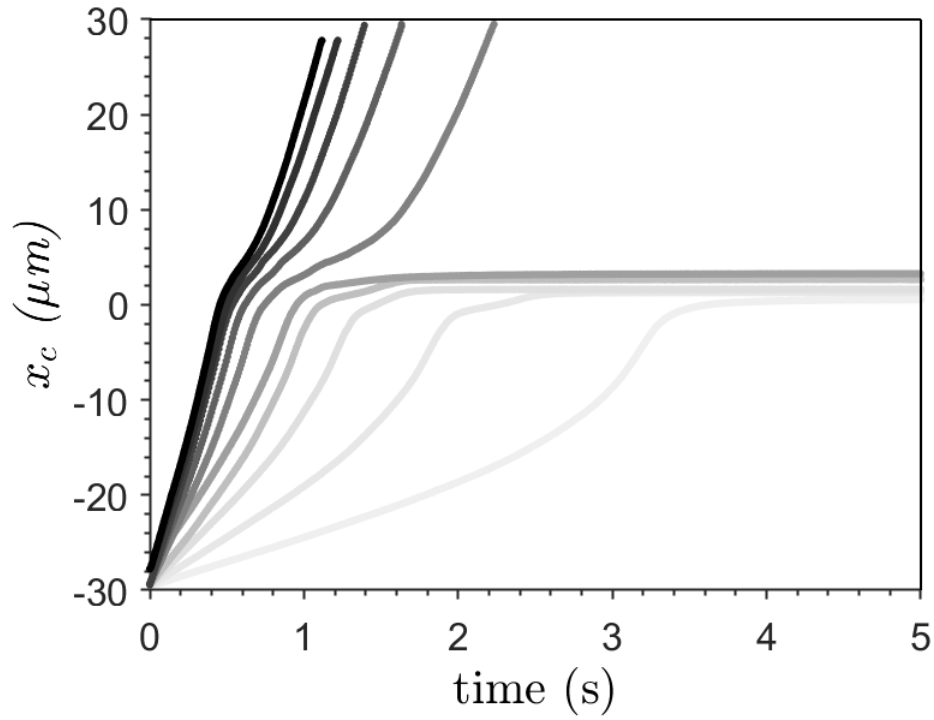


Figure 6.10: System PDMS-core-25 microcapsule centroid position (x_c) as it flows between the magnets for different flow rates: $Q =$ (●) 10 mL/h (●) 20 mL/h (●) 30 mL/h, (●) 40 mL/h, (●) 50 mL/h, (●) 60 mL/h, (●) 70 mL/h, (●) 80 mL/h, (●) 90 mL/h and (●) 100 mL/h. $x_c = 0$ corresponds to magnets center plane.

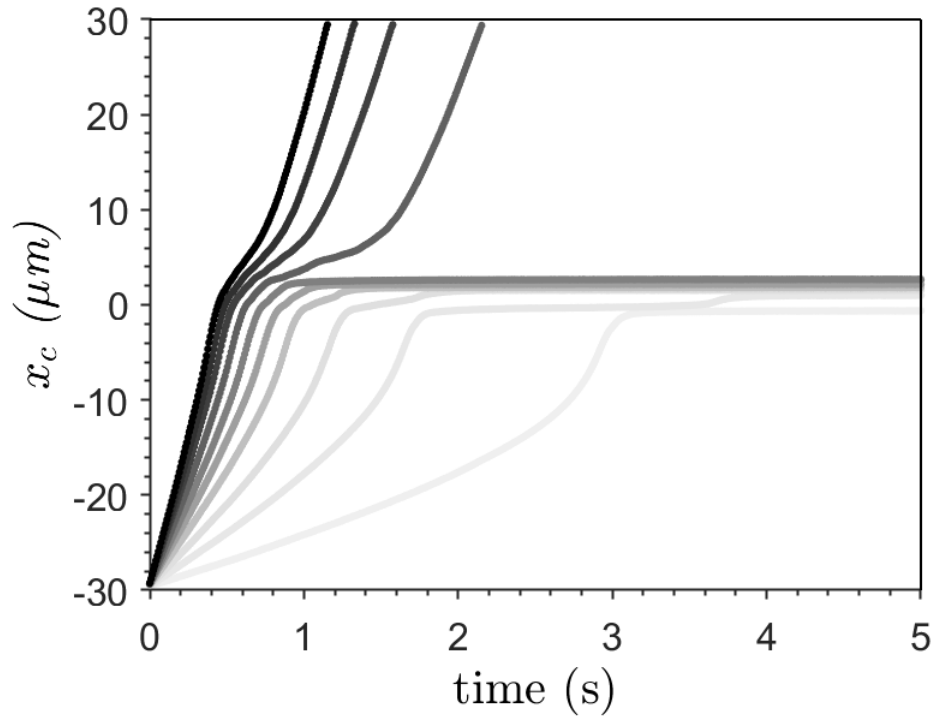


Figure 6.11: System PDMS-core-75 microcapsule centroid position (x_c) as it flows between the magnets for different flow rates: $Q =$ (●) 10 mL/h (●) 20 mL/h (●) 30 mL/h, (●) 40 mL/h, (●) 50 mL/h, (●) 60 mL/h, (●) 70 mL/h, (●) 80 mL/h, (●) 90 mL/h and (●) 100 mL/h. $x_c = 0$ corresponds to magnets center plane.

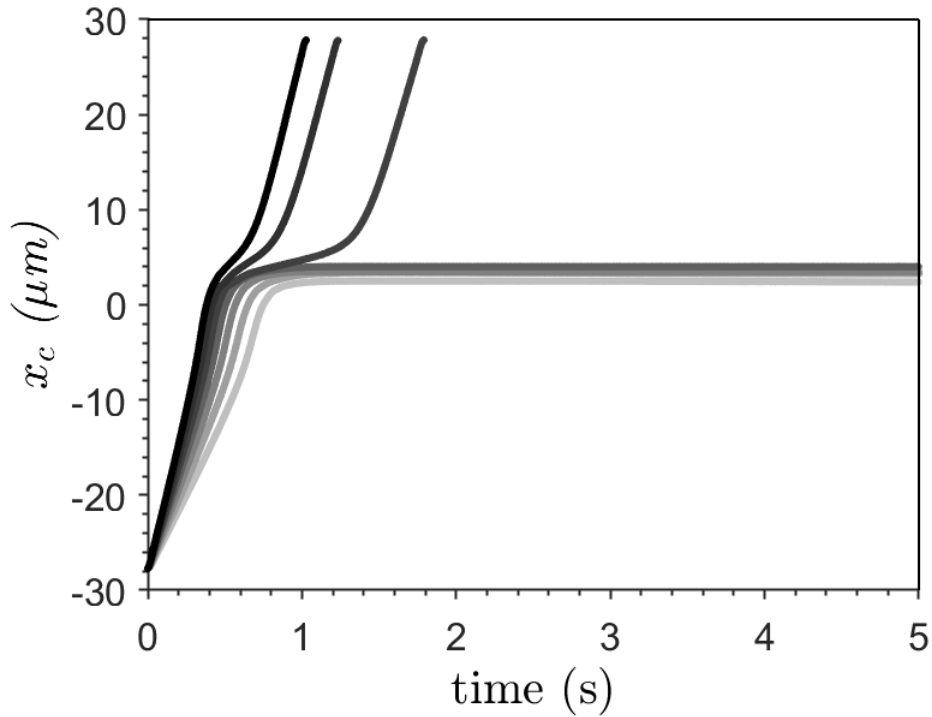


Figure 6.12: System PDMS-core-100 microcapsule centroid position (x_c) as it flows between the magnets for different flow rates: $Q =$ (●) 60 mL/h, (●) 70 mL/h, (●) 80 mL/h, (●) 90 mL/h, (●) 100 mL/h, (●) 110 mL/h and (●) 120 mL/h. $x_c = 0$ corresponds to magnets center plane.

Below a critical flow rate value, the drag force is not strong enough to overcome the maximum magnetic force acting in the capsule, and it is not able to flow through the magnetic field. The microcapsule stops at different positions depending on the flow rate (drag force) value. The position corresponds to the place at which the magnetic field value leads to a magnetic force that equilibrates the drag force. Figure 6.13 shows the final centroid position for each case. The average value and the standard deviation (error bars in the plots) of at least 3 measurements are reported.

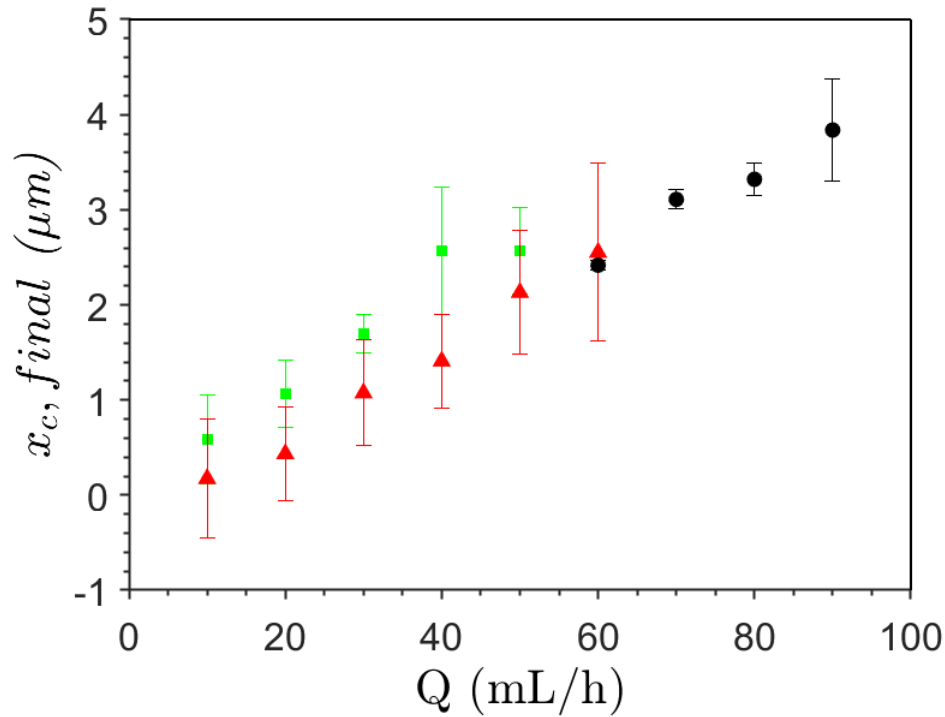


Figure 6.13: Microcapsule final centroid position ($x_{c, final}$) as a function of the flow rate: (■) System PDMS-core-25, (▲) System PDMS-core-75, (●) System PDMS-core-100.

It is possible to see that, for the same flow rate and capsule diameter, and consequently the same drag force, microcapsules with more ferrofluid in their composition tend to stop closer to the magnets. This occurs due to two factors: (i) for those capsules, the needed magnetic field to induce a magnetic force that equals the drag force is weaker and; (ii) the net magnetic field generated by the magnet set-up increases with the distance from the stagnation point until its maximum magnitude ($|B_{x, max}|$), and decays after it, as shown in Fig. 6.14.

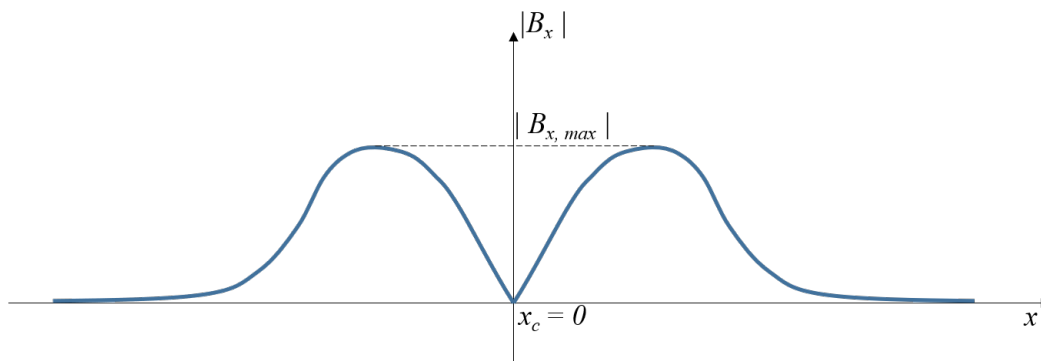
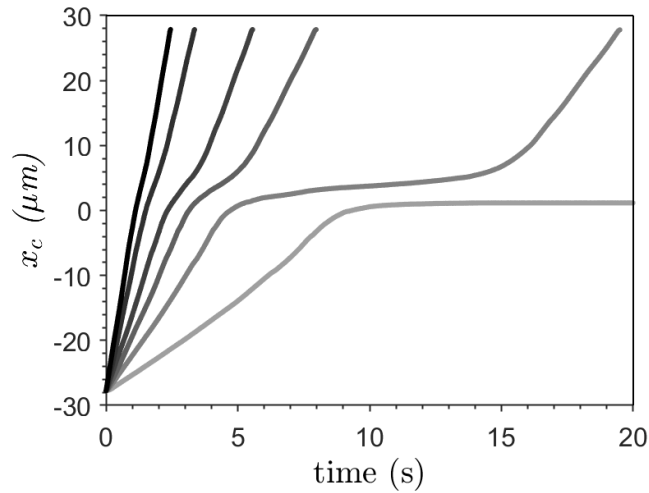


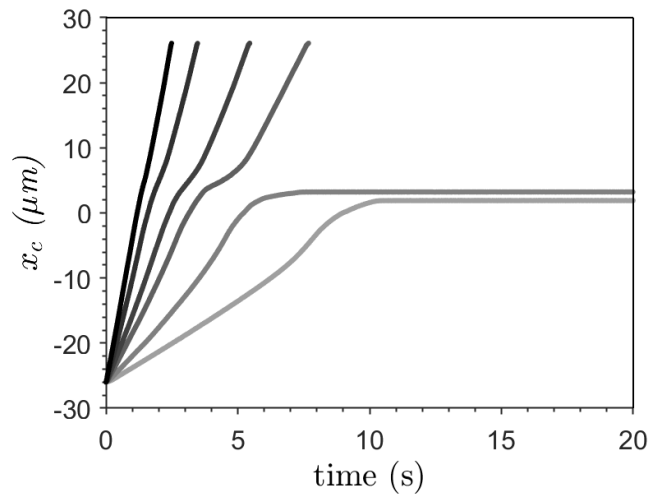
Figure 6.14: Qualitative representation of the magnetic field variation with distance in the flow direction.

The motion of PDMS capsules with magnetic nanoparticles in the shell is presented in Fig. 6.15. For these microcapsules, much lower flow rates (10 mL/h or 15 mL/h) and consequently drag forces were able to move them through the magnets. In the example presented in Fig. 6.15(a), for a capsule from System PDMS-shell-25-1, it is possible to see that, at a flow rate of 10 mL/h, the capsule has its velocity drastically decreased by the magnets as its position almost does not change. However, after some time (≈ 10 s), the capsule flows away from the magnets, at a higher velocity. This was the minimum flow rate tested that did not stop the capsules from this system. For the other two systems presented in Fig. 6.15, with thicker shells, this minimum flow rate was 15 mL/h. For these systems, at which the magnetic nanoparticles are suspended in a solid phase, the magnetic nanoparticles are not free to move and align themselves with the magnetic field, resulting in a lower magnetic force.

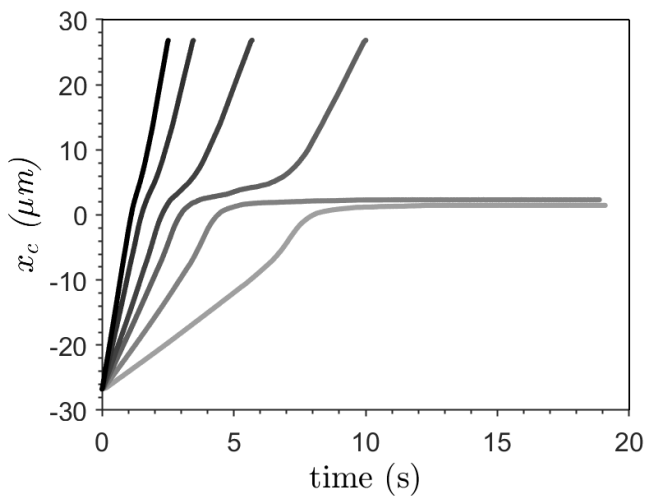
As in the systems with nanoparticles suspended in the liquid core, the maximum magnetic force acting in each capsule is a function of the number of particles suspended. As the shell thickness is increased, and therefore the number of magnetic particles rises, the critical flow rate and drag force also increase. For System PDMS-S-25-1, with $t = 56.0 \mu\text{m}$, the drag force had to be higher than $F_D \approx 3.3 \times 10^{-7}$ N to overcome the magnetic force; for System PDMS-S-25-2, with $t = 122.0 \mu\text{m}$, it had to be higher than $F_D \approx 5.8 \times 10^{-7}$ N and for System PDMS-S-25-3, with $t = 222.0 \mu\text{m}$, higher than $F_D \approx 6.4 \times 10^{-7}$.



(a)



(b)



(c)

Figure 6.15: Microcapsule centroid position (x_c) as it flows between the magnets for different flow rates: $Q =$ (●) 5 mL/h, (●) 10 mL/h, (●) 15 mL/h, (●) 20 mL/h, (●) 30 mL/h and (●) 40 mL/h. $x_c = 0$ corresponds to magnets center plane. (a) System PDMS-shell-25-1, (b) System PDMS-shell-25-2 and (c) System PDMS-shell-25-3.

As discussed before, when the magnetic force is equal to the drag force caused by the flow, the net force acting on the capsules is zero and they stop flowing. Table 6.7 summarizes the maximum magnetic force ($F_{M,max}$) acting in the capsules from the different systems tested. The values cover a range larger than one order of magnitude, showing that very different magnetic response can be obtained by changing the capsules' configuration. Figure 6.16 presents the maximum magnetic force as a function of the volume of suspended magnetic particles for all the systems tested. Clearly, the intensity of the magnetic response is a function of the configuration of the microcapsules, with magnetic nanoparticles suspended either in the liquid core or in the solid polymeric shell. In the capsules with the ferrofluid in the liquid inner core, the magnetic particles are free to align with the magnetic field, leading to higher magnetic forces. In the capsules with the magnetic particles suspended in the solid polymeric shell, the particles cannot align with the magnetic field, leading to significantly lower magnetic force. For both configurations, the magnetic force increases with the volume of nanoparticles used.

| System ID | D (μm) | t (μm) | $F_{M,max}$ (N) |
|-----------------|-----------------------|-----------------------|------------------------------|
| Gellan-core-75 | 221.0 ± 3.6 | 15.7 ± 1.9 | $\approx 1.2 \times 10^{-6}$ |
| Gellan-core-100 | 244.1 ± 3.4 | 22.0 ± 7.2 | $\approx 2.1 \times 10^{-6}$ |
| PDMS-core-25 | 622.3 ± 4.6 | 61.0 ± 6.8 | $\approx 4.2 \times 10^{-6}$ |
| PDMS-core-75 | 635.1 ± 6.2 | 71.6 ± 7.3 | $\approx 5.0 \times 10^{-6}$ |
| PDMS-core-100 | 655.3 ± 3.7 | 54.9 ± 4.7 | $\approx 9.2 \times 10^{-6}$ |
| PDMS-shell-25-1 | 613.0 ± 4.6 | 56.0 | $\approx 3.3 \times 10^{-7}$ |
| PDMS-shell-25-2 | 590.1 ± 3.9 | 122.0 | $\approx 5.8 \times 10^{-7}$ |
| PDMS-shell-25-3 | 601.0 ± 4.4 | 222.0 | $\approx 6.4 \times 10^{-7}$ |

Table 6.7: Maximum magnetic force to stop the flow of capsules from each system.

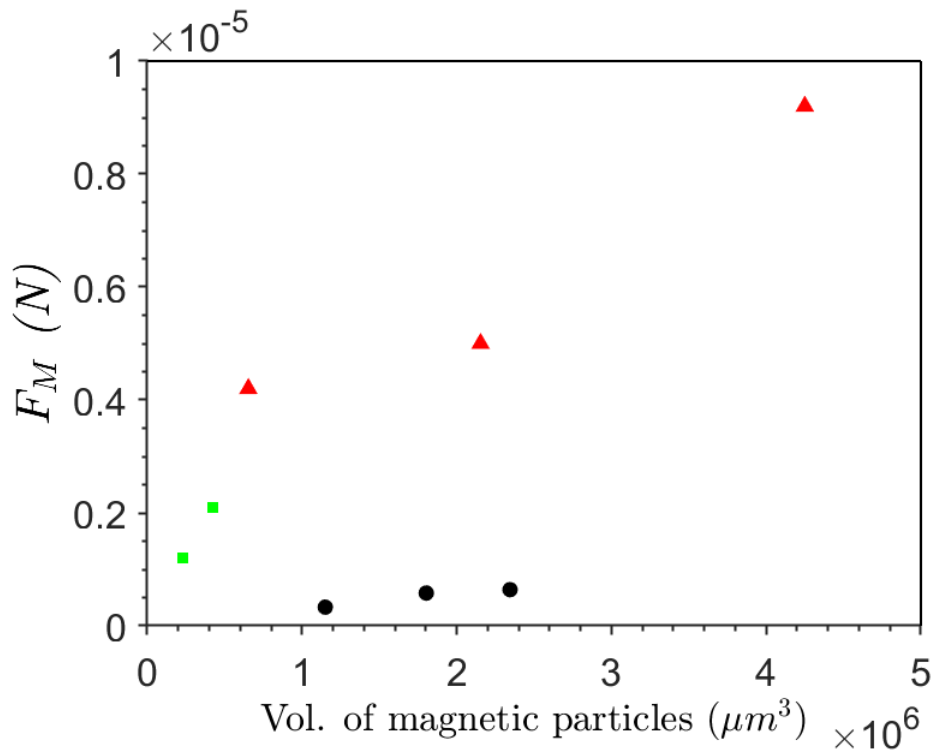


Figure 6.16: Maximum magnetic force as a function of the volume of suspended magnetic nanoparticles for capsules with particles suspended in the liquid core and in the solid shell: (■) Gellan-core, (▲) PDMS-core, (●) PDMS-shell.

6.2.5 Conclusions

Microcapsules with ferrofluid in their composition have paramagnetic properties and are attracted by magnets. The magnetic response of these microcapsules depends on their dimensions and on ferrofluid properties.

The results presented in this chapter show the production of magnetic microcapsules using both water-based and oil-based ferrofluids, with magnetic nanoparticles embedded in the core or in the capsule shell. The magnetic response was characterized by flowing the capsules suspended in a liquid through a tube exposed to a magnetic field. The magnetic response, characterized by the magnetic force acting on the capsule as it flows through a magnetic field, can be controlled by suspending the nanoparticles either in the core or shell, changing the ferrofluid concentration, capsule diameter and shell thickness.

These microcapsules with controlled magnetic response can be used in several applications as drug carriers and contrast agents in MRI, for example.

7

Final remarks and suggestions for future works

We successfully demonstrated the formation of O/W/O double emulsion templates aiming biopolymer-based microcapsules production through a glass-capillary microfluidic device using entirely FDA-approved materials. The O/W/O templates were transformed into solid microcapsules through an external ionotropic gelation of the middle phase induced by the calcium acetate. After gelation, the capsules could be dispersed in an aqueous phase, enabling the encapsulation of hydrophobic actives in a water-based dispersion.

In Chapter 3, the operability window of the process was determined as a function of the flow rate of each phase. We observed that fixing the flow rate of the inner phase and varying the flow of the middle phase is the best choice to create microcapsules with an accurate control of the shell thickness, while a systematic variation in the capsules diameter can be achieved by changing the flow rate of the continuous phase. The range of the microcapsule diameter scaled with the diameter of the collection capillary. Therefore, smaller capsules can be obtained using devices with smaller tip diameters of the injection and collection capillaries.

The proposed methodology can be used in a broad range of applications for encapsulating, delivering, and controllably releasing hydrophobic active compounds in a water based medium. In fact, it was demonstrated that, depending on their physical characteristics, gellan microcapsules can release their content triggered by external stress on the flow through small constrictions or act as blocking agents to change liquid mobility. The data provided can be used to validate different numerical models regarding microcapsule flowing through a constriction. Experiments similar to the one presented in Chapter 4 can be made using different geometries and flow rates, depending on the application. The imposed stress is a function of the flow rate and constriction geometry and more abrupt constrictions will lead to larger stresses.

As shown in Chapter 5, due to the pH sensitivity of gellan gum, the capsules made of this material are also suitable for targeted delivery in the intestine. Thus, being valuable for food and pharmaceutical industries. In this regard, the next step should be to carry out encapsulation and cultivate of interesting active compounds for quantification as well as *in vivo* experiments.

By adding a ferrofluid to their core or shell, it is possible not only to magnetize gellan microcapsules but also control their response to external magnetic fields

(see Chapter 6). This enlarges the possibilities of using these microcapsules in applications that require non-intrusively manipulation by external magnetic fields or detection by magnetic sensors. Further studies applying different magnetic fields and sensors can be of interest.

Bibliography

- [1] BAKRY, A. M.; ABBAS, S.; ALI, B.; MAJEED, H.; ABOUELWAFI, M. Y.; MOUSA, A. ; LIANG, L.. **Microencapsulation of oils: A comprehensive review of benefits, techniques, and applications.** *Comprehensive Reviews in Food Science and Food Safety*, 15(1):143–182, Nov. 2015.
- [2] UTADA, A. S.. **Monodisperse double emulsions generated from a micro-capillary device.** *Science*, 308(5721):537–541, Apr. 2005.
- [3] BACELAR, A. H.; SILVA-CORREIA, J.; OLIVEIRA, J. M. ; REIS, R. L.. **Recent progress in gellan gum hydrogels provided by functionalization strategies.** *Journal of Materials Chemistry B*, 4(37):6164–6174, 2016.
- [4] OSMAŁEK, T.; FROELICH, A. ; TASAREK, S.. **Application of gellan gum in pharmacy and medicine.** *International Journal of Pharmaceutics*, 466(1-2):328–340, May 2014.
- [5] SONG, D.; GUPTA, R. K.. **Drag on a sphere in poiseuille flow of shear-thinning power-law fluids.** *Industrial & Engineering Chemistry Research*, 50(23):13105–13115, Dec. 2011.
- [6] MINEKUS, M.; ALMINGER, M.; ALVITO, P.; BALLANCE, S.; BOHN, T.; BOURLIEU, C.; CARRIÈRE, F.; BOUTROU, R.; CORREDIG, M.; DUPONT, D.; DUFOUR, C.; EGGER, L.; GOLDING, M.; KARAKAYA, S.; KIRKHUS, B.; FEUNTEUN, S. L.; LESMES, U.; MACIERZANKA, A.; MACKIE, A.; MARZE, S.; MCCLEMENTS, D. J.; MÉNARD, O.; RECIO, I.; SANTOS, C. N.; SINGH, R. P.; VEGARUD, G. E.; WICKHAM, M. S. J.; WEITSCHIES, W. ; BRODKORB, A.. **A standardised staticin vitrodigestion method suitable for food – an international consensus.** *Food Funct.*, 5(6):1113–1124, 2014.
- [7] DATTA, S. S.; ABBASPOURRAD, A.; AMSTAD, E.; FAN, J.; KIM, S.-H.; ROMANOWSKY, M.; SHUM, H. C.; SUN, B.; UTADA, A. S.; WINDBERGS, M.; ZHOU, S. ; WEITZ, D. A.. **25th anniversary article: Double emulsion templated solid microcapsules: Mechanics and controlled release.** *Advanced Materials*, 26(14):2205–2218, Feb. 2014.

- [8] AMSTAD, E.. **Capsules: Their past and opportunities for their future.** ACS Macro Letters, 6(8):841–847, July 2017.
- [9] XU, S.; TABAKOVIĆ, A.; LIU, X. ; SCHLANGEN, E.. **Calcium alginate capsules encapsulating rejuvenator as healing system for asphalt mastic.** Construction and Building Materials, 169:379–387, Apr. 2018.
- [10] ABBASPOURRAD, A.; CARROLL, N. J.; KIM, S.-H. ; WEITZ, D. A.. **Polymer microcapsules with programmable active release.** Journal of the American Chemical Society, 135(20):7744–7750, May 2013.
- [11] DUBEY, R.; SHAMI, T. ; RAO, K.. **Microencapsulation technology and applications.** Defence Science Journal, 59:82–95, 01 2009.
- [12] WINDBERGS, M.; ZHAO, Y.; HEYMAN, J. ; WEITZ, D. A.. **Biodegradable core–shell carriers for simultaneous encapsulation of synergistic actives.** Journal of the American Chemical Society, 135(21):7933–7937, May 2013.
- [13] SUN, B. J.; SHUM, H. C.; HOLTZE, C. ; WEITZ, D. A.. **Microfluidic melt emulsification for encapsulation and release of actives.** ACS Applied Materials & Interfaces, 2(12):3411–3416, Nov. 2010.
- [14] ABBASPOURRAD, A.; DATTA, S. S. ; WEITZ, D. A.. **Controlling release from pH-responsive microcapsules.** Langmuir, 29(41):12697–12702, Oct. 2013.
- [15] ZHANG, W.; ABBASPOURRAD, A.; CHEN, D.; CAMPBELL, E.; ZHAO, H.; LI, Y.; LI, Q. ; WEITZ, D. A.. **Osmotic pressure triggered rapid release of encapsulated enzymes with enhanced activity.** Advanced Functional Materials, 27(29):1700975, May 2017.
- [16] ZHANG, W.; QU, L.; PEI, H.; QIN, Z.; DIDIER, J.; WU, Z.; BOBE, F.; INGBER, D. E. ; WEITZ, D. A.. **Controllable fabrication of inhomogeneous microcapsules for triggered release by osmotic pressure.** Small, 15(42):1903087, Aug. 2019.
- [17] LIU, L.; WU, F.; JU, X.-J.; XIE, R.; WANG, W.; NIU, C. H. ; CHU, L.-Y.. **Preparation of monodisperse calcium alginate microcapsules via internal gelation in microfluidic-generated double emulsions.** Journal of Colloid and Interface Science, 404:85–90, Aug. 2013.
- [18] LISERRE, A. M.; RÉ, M. I. ; FRANCO, B. D.. **Microencapsulation of *Bifidobacterium animalis* subsp. *lactis* in modified alginate-chitosan beads**

- and evaluation of survival in simulated gastrointestinal conditions.** Food Biotechnology, 21(1):1–16, Mar. 2007.
- [19] MARTINS, E.; PONCELET, D. ; RENARD, D.. **A novel method of oil encapsulation in core-shell alginate microcapsules by dispersion-inverse gelation technique.** Reactive and Functional Polymers, 114:49–57, May 2017.
- [20] ROSAS-FLORES, W.; RAMOS-RAMÍREZ, E. G. ; SALAZAR-MONTOYA, J. A.. **Microencapsulation of lactobacillus helveticus and lactobacillus delbrueckii using alginate and gellan gum.** Carbohydrate Polymers, 98(1):1011–1017, Oct. 2013.
- [21] NABAVI, S. A.; VLADISAVLJEVIĆ, G. T.; BANDULASENA, M. V.; ARJMANDI-TASH, O. ; MANOVIĆ, V.. **Prediction and control of drop formation modes in microfluidic generation of double emulsions by single-step emulsification.** Journal of Colloid and Interface Science, 505:315–324, Nov. 2017.
- [22] TABELING, P.. **Introduction to Microfluidics.** Oxford U. Press, 2005.
- [23] ZHAO, Y.; SHUM, H. C.; ADAMS, L. L. A.; SUN, B.; HOLTZE, C.; GU, Z. ; WEITZ, D. A.. **Enhanced encapsulation of actives in self-sealing microcapsules by precipitation in capsule shells.** Langmuir, 27(23):13988–13991, Dec. 2011.
- [24] CHEN, P. W.; ERB, R. M. ; STUDART, A. R.. **Designer polymer-based microcapsules made using microfluidics.** Langmuir, 28(1):144–152, Dec. 2011.
- [25] LOPETINSKY, R. J.; MASLIYAH, J. H. ; XU, Z.. **Solids-stabilized emulsions: A review.** In: Binks, B. P.; Horozov, T. S., editors, COLLOIDAL PARTICLES AT LIQUID INTERFACES, p. 186–224. Cambridge University Press.
- [26] KABALNOV, A.. **Thermodynamic and theoretical aspects of emulsions and their stability.** Current Opinion in Colloid & Interface Science, 3(3):270–275, June 1998.
- [27] SCHRAMM, L.. **Emulsions, foams, and suspensions : fundamentals and applications.** Wiley-VCH, Weinheim Great Britain, 2005.
- [28] Tadros, T. F., editor. **Emulsion science and technology.** Wiley-VCH, Weinheim, 2009. OCLC: ocn298775843.

- [29] YANG, Y.; FANG, Z.; CHEN, X.; ZHANG, W.; XIE, Y.; CHEN, Y.; LIU, Z. ; YUAN, W.. **An overview of pickering emulsions: Solid-particle materials, classification, morphology, and applications.** *Frontiers in Pharmacology*, 8, May 2017.
- [30] LINKE, C.; DRUSCH, S.. **Pickering emulsions in foods - opportunities and limitations.** *Critical Reviews in Food Science and Nutrition*, 58(12):1971–1985, Oct. 2017.
- [31] IZMAILOVA, V.; YAMPOLSKAYA, G.. **Concentrated emulsions stabilized by macromolecules and the contributions of hans sonntag to this scientific field.** *Colloids and Surfaces A: Physicochemical and Engineering Aspects*, 142(2-3):125–134, Dec. 1998.
- [32] BANCROFT, W. D.. **The theory of emulsification, v.** *The Journal of Physical Chemistry*, 17(6):501–519, June 1913.
- [33] BANCROFT, W. D.. **The theory of emulsification, VI.** *The Journal of Physical Chemistry*, 19(4):275–309, Apr. 1915.
- [34] CLOWES, G. H. A.. **Protoplasmic equilibrium.** *The Journal of Physical Chemistry*, 20(5):407–451, May 1916.
- [35] MCCLEMENTS, D.; DECKER, E. ; WEISS, J.. **Emulsion-based delivery systems for lipophilic bioactive components.** *Journal of Food Science*, 72(8):R109–R124, Oct. 2007.
- [36] MCCLEMENTS, D.. **Nanoparticle- and microparticle-based delivery systems : encapsulation, protection and release of active compounds.** CRC Press, Boca Raton, Florida, 2015.
- [37] FANG, Z.; BHANDARI, B.. **Encapsulation of polyphenols – a review.** *Trends in Food Science & Technology*, 21(10):510–523, Oct. 2010.
- [38] RAYBAUDI-MASSILIA, R. M.; MOSQUEDA-MELGAR, J.. **Polysaccharides as carriers and protectors of additives and bioactive compounds in foods.** In: THE COMPLEX WORLD OF POLYSACCHARIDES. InTech, Oct. 2012.
- [39] WAZARKAR, K.; PATIL, D.; RANE, A.; BALGUDE, D.; KATHALEWAR, M. ; SABNIS, A.. **Microencapsulation: an emerging technique in the modern coating industry.** *RSC Advances*, 6(108):106964–106979, 2016.
- [40] GOUIN, S.. **Microencapsulation.** *Trends in Food Science & Technology*, 15(7-8):330–347, July 2004.

- [41] PAULO, F.; SANTOS, L.. **Design of experiments for microencapsulation applications: A review**. *Materials Science and Engineering: C*, 77:1327–1340, Aug. 2017.
- [42] CALVO, P.; CASTAÑO, Á. L.; HERNÁNDEZ, M. T. ; GONZÁLEZ-GÓMEZ, D.. **Effects of microcapsule constitution on the quality of microencapsulated walnut oil**. *European Journal of Lipid Science and Technology*, 113(10):1273–1280, June 2011.
- [43] GOODWIN, J. T.; SOMERVILLE, G. R.. **Physical methods for preparing microcapsules**. In: *MICROENCAPSULATION*, p. 155–163. Springer US, 1974.
- [44] RÉ, M. I.. **Microencapsulation by spray drying**. *Drying Technology*, 16(6):1195–1236, Jan. 1998.
- [45] GREEN, B.; SCHLEICHER, L.. **Pressure responsive record materials**.
- [46] PEANPARKDEE, M.; IWAMOTO, S. ; YAMAUCHI, R.. **Microencapsulation: A Review Of Applications in the Food and Pharmaceutical Industries**. *Reviews in Agricultural Science*, 4(0):56–65, 2016.
- [47] M.N. SINGH, K.S.Y. HEMANT, M. R.; SHIVAKUMAR, H.. **Microencapsulation: A promising technique for controlled drug delivery**. *Research in Pharmaceutical Sciences*, 5(2):65–77, July 2010.
- [48] LAM, P.; GAMBARI, R.. **Advanced progress of microencapsulation technologies: In vivo and in vitro models for studying oral and transdermal drug deliveries**. *Journal of Controlled Release*, 178:25–45, Mar. 2014.
- [49] CHANG, T. M. S.. **Therapeutic applications of polymeric artificial cells**. *Nature Reviews Drug Discovery*, 4(3):221–235, Mar. 2005.
- [50] HUNT, N. C.; GROVER, L. M.. **Cell encapsulation using biopolymer gels for regenerative medicine**. *Biotechnology Letters*, 32(6):733–742, Feb. 2010.
- [51] ULUDAG, H.; VOS, P. D. ; TRESKO, P. A.. **Technology of mammalian cell encapsulation**. *Advanced Drug Delivery Reviews*, 42(1-2):29–64, Aug. 2000.
- [52] JOKI, T.; MACHLUF, M.; ATALA, A.; ZHU, J.; SEYFRIED, N. T.; DUNN, I. F.; ABE, T.; CARROLL, R. S. ; BLACK, P. M.. **Continuous release of endostatin from microencapsulated engineered cells for tumor therapy**. *Nature Biotechnology*, 19(1):35–39, Jan. 2001.

- [53] ORIVE, G.; HERNÁNDEZ, R. M.; GASCÓN, A. R.; CALAFIORE, R.; CHANG, T. M.; VOS, P. D.; HORTELANO, G.; HUNKELER, D.; LACÍK, I.; SHAPIRO, A. J. ; PEDRAZ, J. L.. **Cell encapsulation: Promise and progress**. *Nature Medicine*, 9(1):104–107, Jan. 2003.
- [54] NEVEU-PRIN, S.; CABUIL, V.; MASSART, R.; ESCAFFRE, P. ; DUSSAUD, J.. **Encapsulation of magnetic fluids**. *Journal of Magnetism and Magnetic Materials*, 122(1-3):42–45, Apr. 1993.
- [55] DEGEN, P.; PESCHEL, S. ; REHAGE, H.. **Stimulated aggregation, rotation, and deformation of magnetite-filled microcapsules in external magnetic fields**. *Colloid and Polymer Science*, 286(8-9):865–871, Feb. 2008.
- [56] HUANG, J.; HUANG, W.; CHEN, Y.; ZHANG, Y. S.; ZHONG, J.; LI, Y. ; ZHOU, J.. **Eccentric magnetic microcapsules for MRI-guided local administration and pH-regulated drug release**. *RSC Advances*, 8(73):41956–41965, 2018.
- [57] VORONIN, D. V.; SINDEEVA, O. A.; KUROCHKIN, M. A.; MAYOROVA, O.; FEDOSOV, I. V.; SEMYACHKINA-GLUSHKOVSKAYA, O.; GORIN, D. A.; TUCHIN, V. V. ; SUKHORUKOV, G. B.. **In vitro and in vivo visualization and trapping of fluorescent magnetic microcapsules in a bloodstream**. *ACS Applied Materials & Interfaces*, 9(8):6885–6893, Feb. 2017.
- [58] SCHROOYEN, P. M. M.; VAN DER MEER, R. ; KRUIF, C. G. D.. **Microencapsulation: its application in nutrition**. *Proceedings of the Nutrition Society*, 60(4):475–479, Nov. 2001.
- [59] MADENE, A.; JACQUOT, M.; SCHER, J. ; DESOBRY, S.. **Flavour encapsulation and controlled release - a review**. *International Journal of Food Science and Technology*, 41(1):1–21, Jan. 2006.
- [60] CARVALHO, I. T.; ESTEVINHO, B. N. ; SANTOS, L.. **Application of microencapsulated essential oils in cosmetic and personal healthcare products - a review**. *International Journal of Cosmetic Science*, 38(2):109–119, May 2015.
- [61] MARTINS, I. M.; BARREIRO, M. F.; COELHO, M. ; RODRIGUES, A. E.. **Microencapsulation of essential oils with biodegradable polymeric carriers for cosmetic applications**. *Chemical Engineering Journal*, 245:191–200, June 2014.

- [62] CHENG, S.; YUEN, C.; KAN, C. ; CHEUK, K.. **Development of cosmetic textiles using microencapsulation technology**. Research Journal of Textile and Apparel, 12(4):41–51, Nov. 2008.
- [63] LI, J.; YANG, S.; MUHAMMAD, Y.; SAHIBZADA, M.; ZHU, Z.; LIU, T. ; LIAO, S.. **Fabrication and application of polyurea formaldehyde-bioasphalt microcapsules as a secondary modifier for the preparation of high self-healing rate SBS modified asphalt**. Construction and Building Materials, 246:118452, June 2020.
- [64] DO NASCIMENTO, D. F.; AVENDAÑO, J. A.; MEHL, A.; MOURA, M. J. B.; CARVALHO, M. S. ; DUNCANSON, W. J.. **Flow of tunable elastic microcapsules through constrictions**. Scientific Reports, 7(1), Sept. 2017.
- [65] ZHANG, L.; ABBASPOURRAD, A.; PARSAR, S.; TANG, J.; CASSIOLA, F.; ZHANG, M.; TIAN, S.; DAI, C.; XIAO, L. ; WEITZ, D. A.. **Core–shell nanohydrogels with programmable swelling for conformance control in porous media**. ACS Applied Materials & Interfaces, 12(30):34217–34225, July 2020.
- [66] KIM, S.-H.; KIM, J. W.; CHO, J.-C. ; WEITZ, D. A.. **Double-emulsion drops with ultra-thin shells for capsule templates**. Lab Chip, 11(18):3162–3166, 2011.
- [67] DESAI, K. G. H.; PARK, H. J.. **Recent developments in microencapsulation of food ingredients**. Drying Technology, 23(7):1361–1394, July 2005.
- [68] GHARSALLAOUI, A.; ROUDAUT, G.; CHAMBIN, O.; VOILLEY, A. ; SAUREL, R.. **Applications of spray-drying in microencapsulation of food ingredients: An overview**. Food Research International, 40(9):1107–1121, Nov. 2007.
- [69] JAFARI, S. M.; ASSADPOOR, E.; HE, Y. ; BHANDARI, B.. **Encapsulation efficiency of food flavours and oils during spray drying**. Drying Technology, 26(7):816–835, July 2008.
- [70] PETROVIC, L. B.; SOVILJ, V. J.; KATONA, J. M. ; MILANOVIC, J. L.. **Influence of polymer–surfactant interactions on o/w emulsion properties and microcapsule formation**. Journal of Colloid and Interface Science, 342(2):333–339, Feb. 2010.
- [71] THIEL, W. J.; NGUYEN, L. T.. **Fluidized bed film coating of an ordered powder mixture to produce microencapsulated ordered units**. Journal of Pharmacy and Pharmacology, 36(3):145–152, Mar. 1984.

- [72] WESDYK, R.; JOSHI, Y.; VINCENTIS, J. D.; NEWMAN, A. ; JAIN, N.. **Factors affecting differences in film thickness of beads coated in fluidized bed units.** International Journal of Pharmaceutics, 93(1-3):101–109, May 1993.
- [73] HWANG, J. R.; SEFTON, M. V.. **Effect of capsule diameter on the permeability to horseradish peroxidase of individual HEMA-MMA microcapsules.** Journal of Controlled Release, 49(2-3):217–227, Dec. 1997.
- [74] WEN-TAO, Q.; WEI-TING, Y.; YU-BING, X. ; XIAOJUN, M.. **Optimization of saccharomyces cerevisiae culture in alginate–chitosan–alginate microcapsule.** Biochemical Engineering Journal, 25(2):151–157, Sept. 2005.
- [75] IJICHI, K.; YOSHIZAWA, H.; UEMURA, Y.; HATATE, Y. ; KAWANO, Y.. **Multi-layered gelatin/acacia microcapsules by complex coacervation method.** Journal of Chemical Engineering of Japan, 30(5):793–798, 1997.
- [76] SING, C. E.; PERRY, S. L.. **Recent progress in the science of complex coacervation.** Soft Matter, 16(12):2885–2914, 2020.
- [77] NAKASHIMA, T.; SHIMIZU, M. ; KUKIZAKI, M.. **Particle control of emulsion by membrane emulsification and its applications.** Advanced Drug Delivery Reviews, 45(1):47–56, Dec. 2000.
- [78] AKAMATSU, K.; CHEN, W.; SUZUKI, Y.; ITO, T.; NAKAO, A.; SUGAWARA, T.; KIKUCHI, R. ; ICHI NAKAO, S.. **Preparation of monodisperse chitosan microcapsules with hollow structures using the SPG membrane emulsification technique.** Langmuir, 26(18):14854–14860, Sept. 2010.
- [79] ANNA, S. L.. **Droplets and bubbles in microfluidic devices.** Annual Review of Fluid Mechanics, 48(1):285–309, Jan. 2016.
- [80] MARTINO, C.; BERGER, S.; WOOTTON, R. C. R. ; DEMELLO, A. J.. **A 3d-printed microcapillary assembly for facile double emulsion generation.** Lab Chip, 14(21):4178–4182, 2014.
- [81] OKUSHIMA, S.; NISISAKO, T.; TORII, T. ; HIGUCHI, T.. **Controlled production of monodisperse double emulsions by two-step droplet breakup in microfluidic devices.** Langmuir, 20(23):9905–9908, Nov. 2004.
- [82] HUANG, S.-H.; TAN, W.-H.; TSENG, F.-G. ; TAKEUCHI, S.. **A monolithically three-dimensional flow-focusing device for formation of single/double emulsions in closed/open microfluidic systems.** Journal of Micromechanics and Microengineering, 16(11):2336–2344, Sept. 2006.

- [83] BARBIER, V.; TATOULIAN, M.; LI, H.; AREFI-KHONSARI, F.; AJDARI, A. ; TABELING, P.. **Stable modification of PDMS surface properties by plasma polymerization: application to the formation of double emulsions in microfluidic systems**. *Langmuir*, 22(12):5230–5232, June 2006.
- [84] THIELE, J.; ABATE, A. R.; SHUM, H. C.; BACHTLER, S.; FÖRSTER, S. ; WEITZ, D. A.. **Fabrication of polymersomes using double-emulsion templates in glass-coated stamped microfluidic devices**. *Small*, 6(16):1723–1727, July 2010.
- [85] GÓMEZ-MASCARAQUE, L. G.; SIPOLI, C. C.; DE LA TORRE, L. G. ; LÓPEZ-RUBIO, A.. **A step forward towards the design of a continuous process to produce hybrid liposome/protein microcapsules**. *Journal of Food Engineering*, 214:175–181, Dec. 2017.
- [86] NISISAKO, T.; OKUSHIMA, S. ; TORII, T.. **Controlled formulation of monodisperse double emulsions in a multiple-phase microfluidic system**. *Soft Matter*, 1(1):23, 2005.
- [87] NURUMBETOV, G.; BALLARD, N. ; BON, S. A. F.. **A simple microfluidic device for fabrication of double emulsion droplets and polymer microcapsules**. *Polymer Chemistry*, 3(4):1043, 2012.
- [88] CHANG, Z.; SERRA, C. A.; BOUQUEY, M.; PRAT, L. ; HADZIIOANNOU, G.. **Co-axial capillaries microfluidic device for synthesizing size- and morphology-controlled polymer core-polymer shell particles**. *Lab on a Chip*, 9(20):3007, 2009.
- [89] ABATE, A. R.; THIELE, J. ; WEITZ, D. A.. **One-step formation of multiple emulsions in microfluidics**. *Lab Chip*, 11(2):253–258, 2011.
- [90] VLADISAVLJEVIĆ, G.; NUUMANI, R. A. ; NABAVI, S.. **Microfluidic production of multiple emulsions**. *Micromachines*, 8(3):75, Mar. 2017.
- [91] NABAVI, S. A.; VLADISAVLJEVIĆ, G. T. ; MANOVIĆ, V.. **Mechanisms and control of single-step microfluidic generation of multi-core double emulsion droplets**. *Chemical Engineering Journal*, 322:140–148, Aug. 2017.
- [92] KIM, S.-H.; JEON, S.-J. ; YANG, S.-M.. **Optofluidic encapsulation of crystalline colloidal arrays into spherical membrane**. *Journal of the American Chemical Society*, 130(18):6040–6046, May 2008.
- [93] MAZUREK, P.; DAUGAARD, A. E.; SKOLIMOWSKI, M.; HVILSTED, S. ; SKOV, A. L.. **Preparing mono-dispersed liquid core PDMS microcapsules**

- from thiol–ene–epoxy-tailored flow-focusing microfluidic devices.** RSC Advances, 5(20):15379–15386, 2015.
- [94] HAYWARD, R. C.; UTADA, A. S.; DAN, N. ; WEITZ, D. A.. **Dewetting instability during the formation of polymersomes from block-copolymer-stabilized double emulsions.** Langmuir, 22(10):4457–4461, May 2006.
- [95] OFNER, A.; MOORE, D. G.; RÜHS, P. A.; SCHWENDIMANN, P.; EGGERSDORFER, M.; AMSTAD, E.; WEITZ, D. A. ; STUDART, A. R.. **High-throughput step emulsification for the production of functional materials using a glass microfluidic device.** Macromolecular Chemistry and Physics, 218(2):1600472, Dec. 2016.
- [96] KIM, S.-H.; KIM, J. W.; KIM, D.-H.; HAN, S.-H. ; WEITZ, D. A.. **Enhanced-throughput production of polymersomes using a parallelized capillary microfluidic device.** Microfluidics and Nanofluidics, 14(3-4):509–514, Oct. 2012.
- [97] ROMANOWSKY, M. B.; ABATE, A. R.; ROTEM, A.; HOLTZE, C. ; WEITZ, D. A.. **High throughput production of single core double emulsions in a parallelized microfluidic device.** Lab on a Chip, 12(4):802, 2012.
- [98] TAYLOR, M.; TOMLINS, P. ; SAHOTA, T.. **Thermoresponsive gels.** Gels, 3(1):4, Jan. 2017.
- [99] ZIA, K. M.; TABASUM, S.; KHAN, M. F.; AKRAM, N.; AKHTER, N.; NOREEN, A. ; ZUBER, M.. **Recent trends on gellan gum blends with natural and synthetic polymers: A review.** International Journal of Biological Macromolecules, 109:1068–1087, Apr. 2018.
- [100] MORRIS, E. R.; NISHINARI, K. ; RINAUDO, M.. **Gelation of gellan – a review.** Food Hydrocolloids, 28(2):373–411, Aug. 2012.
- [101] GRASDALEN, H.; SMIDSRØD, O.. **Gelation of gellan gum.** Carbohydrate Polymers, 7(5):371–393, Jan. 1987.
- [102] GRAHAM, S.; MARINA, P. F. ; BLENCOWE, A.. **Thermoresponsive polysaccharides and their thermoreversible physical hydrogel networks.** Carbohydrate Polymers, 207:143–159, Mar. 2019.
- [103] STEVENS, L. R.; GILMORE, K. J.; WALLACE, G. G. ; IN HET PANHUIS, M.. **Tissue engineering with gellan gum.** Biomaterials Science, 4(9):1276–1290, 2016.

- [104] QUINN, F. X.; HATAKEYAMA, T.; YOSHIDA, H.; TAKAHASHI, M. ; HATAKEYAMA, H.. **The conformational properties of gellan gum hydrogels**. *Polymer Gels and Networks*, 1(2):93–114, Jan. 1993.
- [105] OLIVEIRA, J. T.; MARTINS, L.; PICCIOCHI, R.; MALAFAYA, P. B.; SOUSA, R. A.; NEVES, N. M.; MANO, J. F. ; REIS, R. L.. **Gellan gum: A new biomaterial for cartilage tissue engineering applications**. *Journal of Biomedical Materials Research Part A*, 2009.
- [106] GONG, Y.; WANG, C.; LAI, R. C.; SU, K.; ZHANG, F. ; AN WANG, D.. **An improved injectable polysaccharide hydrogel: modified gellan gum for long-term cartilage regeneration in vitro**. *Journal of Materials Chemistry*, 19(14):1968, 2009.
- [107] KIRCHMAJER, D. M.; STEINHOFF, B.; WARREN, H.; CLARK, R. ; IN HET PANHUIS, M.. **Enhanced gelation properties of purified gellan gum**. *Carbohydrate Research*, 388:125–129, Mar. 2014.
- [108] OGAWA, E.; MATSUZAWA, H. ; IWAHASHI, M.. **Conformational transition of gellan gum of sodium, lithium, and potassium types in aqueous solutions**. *Food Hydrocolloids*, 16(1):1–9, Jan. 2002.
- [109] NAYAK, A. K.; PAL, D. ; SANTRA, K.. **Tamarind seed polysaccharide–gellan mucoadhesive beads for controlled release of metformin HCl**. *Carbohydrate Polymers*, 103:154–163, Mar. 2014.
- [110] MATRICARDI, P.; CENCETTI, C.; RIA, R.; ALHAIQUE, F. ; COVIELLO, T.. **Preparation and characterization of novel gellan gum hydrogels suitable for modified drug release**. *Molecules*, 14(9):3376–3391, Sept. 2009.
- [111] LAU, M.; TANG, J. ; PAULSON, A.. **Texture profile and turbidity of gellan/gelatin mixed gels**. *Food Research International*, 33(8):665–671, Oct. 2000.
- [112] SMITH, A. M.; SHELTON, R. M.; PERRIE, Y. ; HARRIS, J. J.. **An initial evaluation of gellan gum as a material for tissue engineering applications**. *Journal of Biomaterials Applications*, 22(3):241–254, Jan. 2007.
- [113] VIEIRA, S.; DA SILVA MORAIS, A.; GARET, E.; SILVA-CORREIA, J.; REIS, R. L.; GONZÁLEZ-FERNÁNDEZ, Á. ; OLIVEIRA, J. M.. **Self-mineralizing ca-enriched methacrylated gellan gum beads for bone tissue engineering**. *Acta Biomaterialia*, 93:74–85, July 2019.

- [114] OLIVEIRA, J. T.; SANTOS, T. C.; MARTINS, L.; SILVA, M. A.; MARQUES, A. P.; CASTRO, A. G.; NEVES, N. M. ; REIS, R. L.. **Performance of new gellan gum hydrogels combined with human articular chondrocytes for cartilage regeneration when subcutaneously implanted in nude mice.** *Journal of Tissue Engineering and Regenerative Medicine*, 3(7):493–500, Oct. 2009.
- [115] OLIVEIRA, J. T.; GARDEL, L. S.; RADA, T.; MARTINS, L.; GOMES, M. E. ; REIS, R. L.. **Injectable gellan gum hydrogels with autologous cells for the treatment of rabbit articular cartilage defects.** *Journal of Orthopaedic Research*, 28(9):1193–1199, Feb. 2010.
- [116] SILVA-CORREIA, J.; OLIVEIRA, J. M.; CARIDADE, S. G.; OLIVEIRA, J. T.; SOUSA, R. A.; MANO, J. F. ; REIS, R. L.. **Gellan gum-based hydrogels for intervertebral disc tissue-engineering applications.** *Journal of Tissue Engineering and Regenerative Medicine*, 5(6):e97–e107, Dec. 2010.
- [117] MIYAZAKI, S.; AOYAMA, H.; KAWASAKI, N.; KUBO, W. ; ATTWOOD, D.. **In situ-gelling gellan formulations as vehicles for oral drug delivery.** *Journal of Controlled Release*, 60(2-3):287–295, Aug. 1999.
- [118] KUBO, W.. **Oral sustained delivery of paracetamol from in situ-gelling gellan and sodium alginate formulations.** *International Journal of Pharmaceutics*, 258(1-2):55–64, June 2003.
- [119] ALHAIQUE, F.; SANTUCCI, E.; CARAFA, M.; COVIELLO, T.; MURTAS, E. ; RICCIERI, F.. **Gellan in sustained release formulations: preparation of gel capsules and release studies.** *Biomaterials*, 17(20):1981–1986, Oct. 1996.
- [120] MICHELON, M.; LEOPÉRCIO, B. C. ; CARVALHO, M. S.. **Microfluidic production of aqueous suspensions of gellan-based microcapsules containing hydrophobic compounds.** *Chemical Engineering Science*, 211:115314, Jan. 2020.
- [121] COSTA, A. L. R.; GOMES, A.; USHIKUBO, F. Y. ; CUNHA, R. L.. **Gellan microgels produced in planar microfluidic devices.** *Journal of Food Engineering*, 209:18–25, Sept. 2017.
- [122] VLADISAVLJEVIĆ, G. T.; SHUM, H. C. ; WEITZ, D. A.. **Control over the shell thickness of core/shell drops in three-phase glass capillary devices.** In: *UK COLLOIDS 2011*, p. 115–118. Springer Berlin Heidelberg, 2012.

- [123] VILANOVA, N.; RODRÍGUEZ-ABREU, C.; FERNÁNDEZ-NIEVES, A. ; SOLANS, C.. **Fabrication of novel silicone capsules with tunable mechanical properties by microfluidic techniques.** ACS Applied Materials & Interfaces, 5(11):5247–5252, May 2013.
- [124] LEE, D.; WEITZ, D. A.. **Double emulsion-templated nanoparticle colloidosomes with selective permeability.** Advanced Materials, 20(18):3498–3503, Aug. 2008.
- [125] KONG, F.; ZHANG, X. ; HAI, M.. **Microfluidics fabrication of monodisperse biocompatible phospholipid vesicles for encapsulation and delivery of hydrophilic drug or active compound.** Langmuir, 30(13):3905–3912, Mar. 2014.
- [126] NABAVI, S. A.; VLADISAVLJEVIĆ, G. T.; GU, S. ; EKANEM, E. E.. **Double emulsion production in glass capillary microfluidic device: Parametric investigation of droplet generation behaviour.** Chemical Engineering Science, 130:183–196, July 2015.
- [127] HENNEQUIN, Y.; PANNACCI, N.; DE TORRES, C. P.; TETRADIS-MERIS, G.; CHAPULIOT, S.; BOUCHAUD, E. ; TABELING, P.. **Synthesizing microcapsules with controlled geometrical and mechanical properties with microfluidic double emulsion technology.** Langmuir, 25(14):7857–7861, July 2009.
- [128] PICONE, C. S. F.; DA CUNHA, R. L.. **Interactions between milk proteins and gellan gum in acidified gels.** Food Hydrocolloids, 24(5):502–511, July 2010.
- [129] SANTOS, T. P.; CUNHA, R. L.. **Role of process variables on the formation and in vitro digestion of gellan gels.** Carbohydrate Polymers, 192:111–117, July 2018.
- [130] YAMAMOTO, F.; CUNHA, R.. **Acid gelation of gellan: Effect of final pH and heat treatment conditions.** Carbohydrate Polymers, 68(3):517–527, Apr. 2007.
- [131] VILELA, J. A. P.; CAVALLIERI, Â. L. F. ; DA CUNHA, R. L.. **The influence of gelation rate on the physical properties/structure of salt-induced gels of soy protein isolate–gellan gum.** Food Hydrocolloids, 25(7):1710–1718, Oct. 2011.

- [132] LEE, D.; WEITZ, D. A.. **Nonspherical colloidosomes with multiple compartments from double emulsions.** *Small*, 5(17):1932–1935, Sept. 2009.
- [133] BURGAIN, J.; GAIANI, C.; LINDER, M. ; SCHER, J.. **Encapsulation of probiotic living cells: From laboratory scale to industrial applications.** *Journal of Food Engineering*, 104(4):467–483, June 2011.
- [134] PEÑA, B.; PANISELLO, C.; ARESTÉ, G.; GARCIA-VALLS, R. ; GUMÍ, T.. **Preparation and characterization of polysulfone microcapsules for perfume release.** *Chemical Engineering Journal*, 179:394–403, Jan. 2012.
- [135] DE COCK, L. J.; DE KOKER, S.; DE GEEST, B. G.; GROOTEN, J.; VERVAET, C.; REMON, J. P.; SUKHORUKOV, G. B. ; ANTIPINA, M. N.. **Polymeric multilayer capsules in drug delivery.** *Angewandte Chemie International Edition*, 49(39):6954–6973, July 2010.
- [136] HUANG, L.; ZHOU, J.; CHEN, Y.; LI, W.; HAN, X. ; WANG, L.. **Engineering microcapsules for simultaneous delivery of combinational therapeutics.** *Advanced Materials Technologies*, 5(11):2000623, Sept. 2020.
- [137] GUN, W. J.; ROUTH, A. F.. **Microcapsule flow behaviour in porous media.** *Chemical Engineering Science*, 102:309–314, Oct. 2013.
- [138] ABBASPOURRAD, A.; DUNCANSON, W. J.; LEBEDEVA, N.; KIM, S.-H.; ZHUSHMA, A. P.; DATTA, S. S.; DAYTON, P. A.; SHEIKO, S. S.; RUBINSTEIN, M. ; WEITZ, D. A.. **Microfluidic fabrication of stable gas-filled microcapsules for acoustic contrast enhancement.** *Langmuir*, 29(40):12352–12357, Sept. 2013.
- [139] RIBEIRO, R. C. O. S.. **3d visualization of oil displacement in porous media by the injection of microcapsule suspension using confocal microscopy.** In: SPE ANNUAL TECHNICAL CONFERENCE AND EXHIBITION. Society of Petroleum Engineers, 2020.
- [140] FREUND, J. B.. **Numerical simulation of flowing blood cells.** *Annual Review of Fluid Mechanics*, 46(1):67–95, Jan. 2014.
- [141] MAO, X.; HUANG, T. J.. **Exploiting mechanical biomarkers in microfluidics.** *Lab on a Chip*, 12(20):4006, 2012.
- [142] SURESH, S.. **Biomechanics and biophysics of cancer cells.** *Acta Biomaterialia*, 3(4):413–438, July 2007.

- [143] HOU, H. W.; LI, Q. S.; LEE, G. Y. H.; KUMAR, A. P.; ONG, C. N. ; LIM, C. T.. **Deformability study of breast cancer cells using microfluidics.** *Biomedical Microdevices*, 11(3):557–564, Dec. 2008.
- [144] BARTHÈS-BIESEL, D.. **Motion and deformation of elastic capsules and vesicles in flow.** *Annual Review of Fluid Mechanics*, 48(1):25–52, Jan. 2016.
- [145] LEYRAT-MAURIN, A.; BARTHES-BIESEL, D.. **Motion of a deformable capsule through a hyperbolic constriction.** *Journal of Fluid Mechanics*, 279:135–163, Nov. 1994.
- [146] RORAI, C.; TOUCHARD, A.; ZHU, L. ; BRANDT, L.. **Motion of an elastic capsule in a constricted microchannel.** *The European Physical Journal E*, 38(5), May 2015.
- [147] DIMITRAKOPOULOS, P.; KURIAKOSE, S.. **Determining a membrane's shear modulus, independent of its area-dilatation modulus, via capsule flow in a converging micro-capillary.** *Soft Matter*, 11(14):2782–2793, 2015.
- [148] RISSO, F.; COLLÉ-PAILOT, F. ; ZAGZOULE, M.. **Experimental investigation of a bioartificial capsule flowing in a narrow tube.** *Journal of Fluid Mechanics*, 547(-1):149, Jan. 2006.
- [149] LEFEBVRE, Y.; BARTHÈS-BIESEL, D.. **Motion of a capsule in a cylindrical tube: effect of membrane pre-stress.** *Journal of Fluid Mechanics*, 589:157–181, Oct. 2007.
- [150] LECLERC, E.; KINOSHITA, H.; FUJII, T. ; BARTHÈS-BIESEL, D.. **Transient flow of microcapsules through convergent–divergent microchannels.** *Microfluidics and Nanofluidics*, 12(5):761–770, Dec. 2011.
- [151] LEONG, F. Y.; LI, Q.; LIM, C. T. ; CHIAM, K.-H.. **Modeling cell entry into a micro-channel.** *Biomechanics and Modeling in Mechanobiology*, 10(5):755–766, Nov. 2010.
- [152] COBOS, S.; CARVALHO, M. ; ALVARADO, V.. **Flow of oil–water emulsions through a constricted capillary.** *International Journal of Multiphase Flow*, 35(6):507–515, June 2009.
- [153] HUANG, Y.; SALMON, F.; KAMBLE, A.; XU, A.; MICHELON, M.; LEOPÉRCIO, B. C.; CARVALHO, M. S. ; FROSTAD, J.. **Methods and models for the mechanical characterization of edible microcapsules.** *Food Hydrocolloids* (submitted), 2021.

- [154] ROCA, J. F.; MENEZES, I. F. ; CARVALHO, M. S.. **Mobility reduction in the flow of an elastic microcapsule through a constricted channel.** Industrial & Engineering Chemistry Research, Jan. 2021.
- [155] LENGYEL, M.; KÁLLAI-SZABÓ, N.; ANTAL, V.; LAKI, A. J. ; ANTAL, I.. **Microparticles, microspheres, and microcapsules for advanced drug delivery.** Scientia Pharmaceutica, 87(3):20, Aug. 2019.
- [156] ARENAS-JAL, M.; SUÑÉ-NEGRE, J. M. ; GARCÍA-MONTOYA, E.. **An overview of microencapsulation in the food industry: opportunities, challenges, and innovations.** European Food Research and Technology, 246(7):1371–1382, Apr. 2020.
- [157] HILL, C.; GUARNER, F.; REID, G.; GIBSON, G. R.; MERENSTEIN, D. J.; POT, B.; MORELLI, L.; CANANI, R. B.; FLINT, H. J.; SALMINEN, S.; CALDER, P. C. ; SANDERS, M. E.. **The international scientific association for probiotics and prebiotics consensus statement on the scope and appropriate use of the term probiotic.** Nature Reviews Gastroenterology & Hepatology, 11(8):506–514, June 2014.
- [158] PICONE, C. S. F.; BUENO, A. C.; MICHELON, M. ; CUNHA, R. L.. **Development of a probiotic delivery system based on gelation of water-in-oil emulsions.** LWT, 86:62–68, Dec. 2017.
- [159] SASTRY, S. V.; NYSHADHAM, J. R. ; FIX, J. A.. **Recent technological advances in oral drug delivery – a review.** Pharmaceutical Science & Technology Today, 3(4):138–145, Apr. 2000.
- [160] BRODKORB, A.; EGGER, L.; ALMINGER, M.; ALVITO, P.; ASSUNÇÃO, R.; BALLANCE, S.; BOHN, T.; BOURLIEU-LACANAL, C.; BOUTROU, R.; CARRIÈRE, F.; CLEMENTE, A.; CORREDIG, M.; DUPONT, D.; DUFOUR, C.; EDWARDS, C.; GOLDING, M.; KARAKAYA, S.; KIRKHUS, B.; FEUNTEUN, S. L.; LESMES, U.; MACIERZANKA, A.; MACKIE, A. R.; MARTINS, C.; MARZE, S.; MCCLEMENTS, D. J.; MÉNARD, O.; MINEKUS, M.; PORTMANN, R.; SANTOS, C. N.; SOUCHON, I.; SINGH, R. P.; VEGARUD, G. E.; WICKHAM, M. S. J.; WEITSCHIES, W. ; RECIO, I.. **INFOGEST static in vitro simulation of gastrointestinal food digestion.** Nature Protocols, Mar. 2019.
- [161] RIVAS, J.; KOLEN'KO, Y. ; BAÑOBRE-LÓPEZ, M.. **Magnetic nanocolloids.** In: NANOCOLLOIDS, p. 75–129. Elsevier, 2016.

- [162] SCHERER, C.; NETO, A. M. F.. **Ferrofluids: properties and applications**. Brazilian Journal of Physics, 35(3a):718–727, Sept. 2005.
- [163] MCBAIN, S.; YIU, H. ; DOBSON, J.. **Magnetic nanoparticles for gene and drug delivery**. International Journal of Nanomedicine, p. 169, June 2008.
- [164] WISCHNEWSKI, C.; KIERFELD, J.. **Spheroidal and conical shapes of ferrofluid-filled capsules in magnetic fields**. Physical Review Fluids, 3(4), Apr. 2018.
- [165] ANTIPINA, M. N.; SUKHORUKOV, G. B.. **Remote control over guidance and release properties of composite polyelectrolyte based capsules**. Advanced Drug Delivery Reviews, 63(9):716–729, Aug. 2011.
- [166] HUANG, J.; LUO, C.; LI, W.; LI, Y.; ZHANG, Y. S.; ZHOU, J. ; JIANG, Q.. **Eccentric magnetic microcapsules for orientation-specific and dual stimuli-responsive drug release**. Journal of Materials Chemistry B, 3(22):4530–4538, 2015.
- [167] CHAKKARAPANI, P.; SUBBIAH, L.; PALANISAMY, S.; BIBIANA, A.; AHRENTORP, F.; JONASSON, C. ; JOHANSSON, C.. **Encapsulation of methotrexate loaded magnetic microcapsules for magnetic drug targeting and controlled drug release**. Journal of Magnetism and Magnetic Materials, 380:285–294, Apr. 2015.
- [168] CHEN, H.; SULEJMANOVIC, D.; MOORE, T.; COLVIN, D. C.; QI, B.; MEFFORD, O. T.; GORE, J. C.; ALEXIS, F.; HWU, S.-J. ; ANKER, J. N.. **Iron-loaded magnetic nanocapsules for pH-triggered drug release and MRI imaging**. Chemistry of Materials, 26(6):2105–2112, Mar. 2014.
- [169] KARYAPPA, R. B.; DESHMUKH, S. D. ; THAOKAR, R. M.. **Deformation of an elastic capsule in a uniform electric field**. Physics of Fluids, 26(12):122108, Dec. 2014.